UNIVERSITÄT HAMBURG
DEPARTMENT PHYSIK

Measurement of Z Boson production using $Z \rightarrow ee$ decays with one of the electrons detected in the forward calorimeters of the ATLAS detector using 4.6 fb^{-1} of data collected at $\sqrt{s} = 7$ TeV.

Dissertation
zur Erlangung des Doktorgrades
des Department Physik
der Universität Hamburg

vorgelegt von
George Sedov
aus Leningrad

Hamburg
2016

Gutachter der Dissertation:	Dr. Habil. Alexandre Glazov
	Prof. Dr. Johannes Haller
Gutachter der Disputation:	Prof. Dr. Caren Hagner
	Dr. Andreas Ringwald
	Prof. Dr. Erika Garutti
Datum der Disputation:	1 Dezember 2016
Vorsitzender des Prüfungsausschusses:	Prof. Dr. Caren Hagner
Vorsitzender des Promotionsausschusses:	Prof. Dr. Jan Louis
Leiter des Departments Physik:	Prof. Dr. Michael Potthoff
Dekan der MIN-Fakultät:	Prof. Dr. Heinrich Graener

Abstract

The double differential cross-section for Z bosons decaying in the electron channel was measured as a function of the di-electron invariant mass and rapidity. For this measurement, the data collected at the ATLAS detector at the LHC during 2011 at a center-of-mass energy of $\sqrt{s} = 7$ TeV was used.

The analysis is focused on the central-forward Z bosons, i.e. the bosons that decay into two electrons, one of which is reconstructed in the central region of the detector ($|\eta| < 2.5$) and the other in the forward region of the detector ($|\eta| > 2.5$). Several sources of the systematic uncertainties were taken into account, including the electron reconstruction and identification efficiencies, pileup effects, PDF sets for the initial protons, and differences between various Monte Carlo simulations. The main sources of uncertainties were found to be the efficiency scales of the forward electron identification and the forward electron energy resolution. The results of the analysis are in agreement with measurements in other decay channels of the Z boson and with theoretical predictions.

The fast simulation method called Frozen Showers was developed to speed up the simulation of Monte Carlo data samples. This method increases the simulation speed by $\sim$25% while introducing additional errors of less than 1% in the energy scale and resolution of the reconstructed particles. The method was used to speed up the production of all Monte Carlo samples used in this analysis.

Zusammenfassung

Die vorliegende Arbeit stellt eine Messung des doppel-differenziellen Wirkungsquerschnitts des Z-Bosons im Elektronen Kanal dar. Die zugrundeliegenden Daten wurden bei einer Schwerpunktsenergie von $\sqrt{s} = 7\,\mathrm{TeV}$ im Jahr 2011 mit dem ATLAS-Detektor am LHC aufgezeichnet.

Die Analyse betrachtet Z-Bosonen im Zentral-Vorwärts Bereich, d.h., Bosonen, die in zwei Elektronen zerfallen, von denen je eines im Zentral-Bereich des Detektors ($|\eta| < 2.5$) und das andere im Vowärts-Bereich ($|\eta| > 2.5$) rekonstruiert wird. Systematische Unsicherheiten z.B. durch Pileup-Effekte, Effizienzunsicherheiten und Unterschiede zwischen den verwendeten Parton-Verteilungsfunktionen der Monte-Carlo-Generatoren wurden berücksichtigt. Den grösten Beitrag hierbei stellen die Unsicherheiten auf die Korrekturfaktoren der Elektronrekonstruktion im Vorwärtsbereich und deren Energiekalibration dar. Die Ergebnisse dieser Arbeit sind mit den Resultaten aus Analysen anderer Zerfalls-Kanäle sowie theoretischen Vorhersagen in Übereinstimmung.

In Zuge dieser Arbeit wurde die sogennante Frozen Showers Simulationsmethode entwickelt, um die Generierung von Monte-Carlo Daten zu beschleunigen. Mithilfe dieser Methode konnte die Simulationsgeschwindigkeit um circa 25% verbessert werden, während hingegen eine zusätzliche Unsicherheit von weniger als 1% auf die Energieskala und Auflösung der rekonstruierten Teilchen einführt wird. Die Methode wurde zur Generierung aller in dieser Arbeit verwendeten Monte Carlo Datensätze verwendet.

Contents

CHAPTER 1

Thesis overview

This thesis describes the measurement of the neutral current Drell-Yan cross-section in the electron channel measured in the forward region of the ATLAS detector. The data samples are collected in the year 2011 during the *pp* collisions at $\sqrt{s} = 7$ TeV at LHC. For the unfolding of the detector-level results, the Monte Carlo (MC) simulation based on the collisions conditions during 2011 is used. The theoretical predictions use various parton distribution functions (PDFs) derived from previous experimental data samples.

All the details of the cross-section measurements are described in the corresponding chapters. The highlights of the analysis include the details of the Monte Carlo generation, the technicalities of the event reconstruction and selection, and the distinct features of the ZeeD analysis software, which allowed to speed-up the analysis process by a significant factor.

The focus of this work is the central-forward (CF) variant of the $Z \to ee$ decay, where "central-forward" means that one of the two final-state electrons is detected in the forward calorimeter, while the other in the central. While the CF analysis share a lot with the central-central (CC) one, which is the other possible variant of the $Z \to ee$ decay (both electrons go to the central parts of the detector), there are still some differences in both the analysis chain and in the results. The combination of the two variants of the analysis is possible, and is done in a paper [1] that is yet to be published. The work in this thesis contributes to that paper.

1.1 Thesis organization

The thesis is organized as follows:

Chapter 2. Introduction to the Standard Model, to *pp*-collision physics, and to the Z boson production is given. This chapter also provides a motivation for the $Z \to ee$ cross-section measurements.

Chapter 3. The CERN accelerator complex with LHC is shortly described.

Chapter 4. Description of the ATLAS detector and its relevant sub-components is presented. The physics program of the ATLAS experiment is outlined. The ATLAS data acquisition system and computing strategy are discussed as well.

Chapter 5. The ATLAS data with its luminosity which was collected in 2011 and used for this thesis is described.

Chapter 6. The MC samples generated with different MC algorithms are discussed. The full chain of MC production in the ATLAS experiment is shown. The fast simulation system which is called “Frozen Showers” is described. The system was developed within the scope of this thesis.

Chapter 7. The method of the off-line calibration of the electromagnetic (EM) calorimeter is explained. The systematic uncertainties in the calibration are discussed as well. Resolution of the EM calorimeters is estimated. Impact from the Fast Simulation techniques is discussed.

Chapter 8. The ATLAS event reconstruction of the EM objects, including trigger performance, electron reconstruction and identification, is described.

Chapter 9. The analysis framework developed for this analysis (ZeeD) is described. The method to compress data and speed-up the calculations is shown.

Chapter 10. The event selection for $Z \to e^+e^-$ analysis is discussed. The Central-Forward (CF) selection is introduced.

Chapter 11. The method of the cross-section extraction and the binning definition are presented. The extrapolation techniques are discussed.

Chapter 12. The electron trigger, identification, reconstruction and isolation efficiencies are described. The details of the forward electron efficiencies are discussed.

Chapter 13. Studies of the different backgrounds are presented. Several methods for the background estimation are discussed.

Chapter 14. Inclusive, single and double differential cross-section measurements in bins of the di-electron rapidity and mass are presented. The background estimation, efficiency determination, acceptance calculation and systematic uncertainties are discussed.

Chapter 15. A summary of the main results is given.

CHAPTER 2

Theoretical introduction

In this section the theoretical basis for the measurements are explained. First of all, the overview of the Standard Model, then the theoretical aspects of the pp collisions, and in the end the specifies of the Z boson production are discussed.

2.1 The Standard Model

The Standard Model of particle physics is a theoretical foundation of the modern particle physics. It described all currently-known particles and three out of four currently-known types of interactions (weak, strong, and electromagnetic, excluding gravity). It was developed during the last fifty years and made several predictions on the nature of particles and interactions, all of which were confirmed experimentally by the present time. Among its predictions are quarks and gluons (confirmed by multiple indirect observations during the 1970s), vector bosons (confirmed in 1983 [2]), top-quark (confirmed in 1995 [3]), and τ-neutrino (confirmed in 2000 [4]). The last to-date update to the Standard Model was made in 2002 with the theoretical explanation of neutrino oscillations [5], which was confirmed to be true with the T2K experiment in july 2013 [6]. The most recently confirmed major prediction of the Standard Model was the existence of the Higgs boson, which was confirmed in january 2013.

The main ingredients of the Standard Model are:

- There are 61 fundamental particles divided into several groups (can be seen on Figure 2.1):
    - The quarks, that are carrying electromagnetic weak and color charge, and thus participating in all three interactions. There are two types of quarks defined by their electric charges, three generations, and 3 possible color charges. Together with the anti-particle partner for every particle this makes 36 particles in total.
    - The leptons, which do not carry color charge, and thus do not participate in strong interactions. Again, there are two types of leptons, one having both electric and weak charges and one having only the weak charge, three generations and an anti-particle partner for every particle, which makes the total of 12.

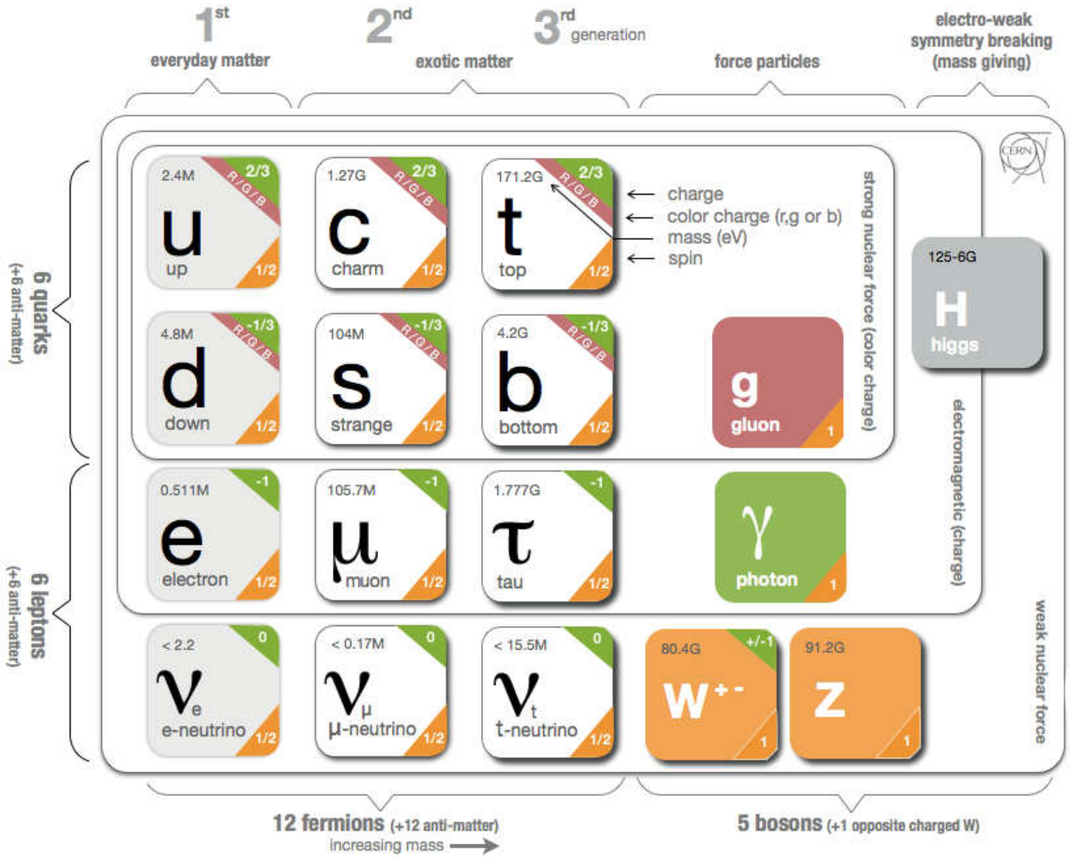

Figure 2.1: The particles of the Standard Model. The image was made during 2012 CERN Summer Student Webfest. [7]

  - The gauge bosons, the force carriers for all three fundamental interactions, which are divided into three symmetry groups: the gluons, the carriers of the strong interaction with 8 possible color charges, constituting the $SU(3)$ group; the $W^{\pm}$ and Z bosons, the carriers of the weak interaction, constituting the $SU(2)$ group; the photons, the carriers of the electromagnetic interaction, constituting the $U(1)$ group. The total number of gauge bosons is thus 12.
  - The Higgs boson, by interacting with which all other particles gain their masses.

- The quarks and leptons, together known as fermions, are participating in the interactions. The strong and electromagnetic interactions only occur between the fermions in the same generation, while the weak interaction can mix the generations, which enables fermions to weakly decay into lighter particles.

- The Standard Model has many parameters which can not be theoretically predicted: the masses of all massive particles, the gauge couplings, the CKM mixing angles and the Weinberg angle (Tab. 2.1).

Parameter	Description	Value
m_u	Up quark mass	2.3 MeV
m_d	Down quark mass	4.8 MeV
m_s	Strange quark mass	95 MeV
m_c	Charm quark mass	1.275 GeV
m_b	Bottom quark mass	4.18 GeV
m_t	Top quark mass	173.5 GeV
m_e	Electron mass	511 keV
m_μ	Muon mass	105.7 MeV
m_τ	Tau mass	1.78 GeV
m_Z	Z boson mass	91.18 GeV
m_W	W boson mass	80.38 GeV
m_H	Higgs boson mass	126 GeV
α	Fine-structure constant	$7.297 \cdot 10^{-3}$
$\alpha_s(m_Z)$	Strong coupling constant	0.1184
$G_F/(\hbar c)^3$	Weak coupling constant	$1.166 \cdot 10^{-5}$
$sin^2\Theta_W$	Weinberg angle	0.231

$$V_{CKM} = \begin{pmatrix} 0.9742 & 0.2253 & 0.0035 \\ 0.2252 & 0.9734 & 0.0412 \\ 0.0086 & 0.0404 & 0.9991 \end{pmatrix}$$

Table 2.1: The list of the parameters of the Standard Model, assuming the masses of neutrinos to be zeros (this is a valid approximation since the mass of neutrinos is very small, $m_\nu < 2$ eV). [8]

The Standard Model is not a single theory which describes everything, it is a system of several interconnected theories which were developed in different times, sometimes replacing one another as new experimental data were obtained. At the start of the 20th century the dominant idea in physics was that of the luminiferous ether [9–11]. The ether was believed to be the source of all matter, as well as both the EM and gravitational forces. When the electron was discovered in 1897 [12] it was regarded as tool for the further development of the ether theory as the "theory of everything", because the observable properties of the electron suggested that it had no "not-electromagnetic" features (i.e. no mass). The high peak of the ether theory was in 1904 when Walter Kaufmann discovered the velocity dependence of the e/m ratio in cathode rays [13, 14], which fell in line with the concept of the electromagnetic impulse previously suggested by Henri Poincare and Max Abraham. At the same time, the new concept of the relativity was developed by Hendrik Lorentz and Albert Einstein [15]. The theory also marked the beginning of the completely new approach (which can be called a "relativistic program" as opposed to the previously established "etherial field program") to the theoretical physics which was one of the reasons why physicist were so reluctant to accept it. It was only in 1911, after the works of Hermann Minkowski [16, 17], when the concept of the relativity became widely accepted.

But even after the acceptance of the idea of relativity, there were some efforts to keep the ether model as the basis for all matter. The most notable theories were made by Gustav Mie [18–20]. His mathematical models that were published in three parts during 1912-1913 attempted to describe both particles (e.g. electrons) and EM interaction (which was believed to be universal and include gravity as well), and they should also be able to mathematically predict fundamental constants, such as electron charge and $\hbar$, also known as Planck's constant, and is a fundamental constant that links the energy of the quantum with its frequency. Mie believed that the quantum effects could be described electromagnetically, because the Planck's constant $\hbar$ was found to be the same order of magnitude as e^2/c (which was previously noted by Einstein, who also tried to construct the similar mathematical model 1908 with no results [21]). But this theory was never finished, the lagrangian for it was never found, even though several physicists tried to find it even in 1930-1940s [22], long after the establishment of the quantum theories. These works also inspired several other attempts to build a unified field theory, such as Jun Ishiwara and Gunnar Nordström in 1914 [23, 24], David Hilbert in 1915 [25, 26], Hermann Weyl in 1919 [27], and finally, the Kaluza-Klein theory in 1921 [28] which was the first theory to introduce the extra dimension, and will later become a foundation for the string theory.

But in the 1920s, all the approaches to construct a field theory that would describe the EM interaction and also have a non-singular, spherically-symmetrical, static solutions that can be interpreted as electrons failed. In the fifth edition of his book, Hermann Weyl, whose theory was considered the last bastion of the geometric field approach, wrote that his theory is no more able to explain the newly discovered physical effects, and that the new theory must be searched for using the quantum approach. And it was during that time when quantum physics made the biggest progress. The theory was quickly established by predicting different spectroscopy results. The biggest milestones were the hypothesis of Louis de Broglie, who postulated the wave-particle duality in 1924 [29]; the development of the matrix mechanics by Werner Heisenberg, Max Born, and Pascual Jordan in 1925 [30–32]; and finally the establishment of the equivalence of wave and matrix approaches in 1926 [33]. The non-deterministic nature of the quantum mechanics was formulated by Heisenberg in 1927 [34]. On the fifth Solvay Conference[1] in 1927, the quantum physics was fully established as the new program of the theoretical physics. All this culminated in the Dirac's equation which was introduced in 1928 [35], and unified the quantum physics with the theory of relativity.

$$(i\hbar c\gamma^{\mu}\partial_{\mu} - mc^2)\Psi = 0\,. \tag{2.1}$$

It allowed to theoretically calculate the energy levels of the hydrogen atom including the fine structure, and explain Zeeman's effect. Based on this equation the formulaes for the Compton scattering were derived as well as one for the bremsstrahlung, which was later observed experimentally. It also predicted the existence of the anti-matter, as a physical interpretation of the solutions with the negative energy (the positrons were discovered in 1932 [36]). The

---

[1] A Solvay Conference is a conference established by International Solvay Institutes for Physics and Chemistry in 1911, and is widely regarded a turning point of the modern physics.

Dirac's equation describes all the half-integer spined non-interacting particles. The following efforts to include the EM interaction in it resulted in the quantum electrodynamics theory.

2.1.1 Quantum Electrodynamics (QED)

The main effort in fundamental physics since the discovery of the particles was the unification of the particles and interactions in a single theory. The class of theories that was searched for was the geometrical field theories, and the most notable figures in that search were Einstein and Weyl. The geometrical field approach never resulted in any successful theory, but it laid the foundation for the pivotal point of the modern Standard Model: the gauge field theory.

It was Weyl's theory developed in 1919 that put basis of the first gauge theory, developed by him together with Vladimir Fock and Fritz London in 1929 [37–39]. Fock was the one to introduce the first version of the local gauge transformation:

$$\begin{aligned} \psi^{'} &= e^{-i\frac{ef(x)}{hc}}\psi\,, \\ \varphi_i^{'} &= \varphi_i + \frac{\partial f(x)}{\partial x_i}\,. \end{aligned} \tag{2.2}$$

The gauge theory is a type of a field theory with the so-called gauge invariance or gauge symmetry. This property allows the freedom to select the configuration of the non-observable parameters of the field, as long as it doesn't change the observable quantities. The example of a simple transformation satisfying this criteria can be constructed using the local $U(1)$ symmetry group:

$$\Psi(x) \rightarrow e^{i\alpha(x)}\Psi(x)\,. \tag{2.3}$$

The term $e^{i\alpha(x)}$ is complex and thus can't be observed, but we also need the equation that describes the field to be invariant under this transformation. With this restriction the equation describing the interacting particles can be derived:

$$\begin{gathered} L = \bar{\Psi}(i\gamma_\mu\partial^\mu - m)\Psi + e\bar{\Psi}\gamma_\mu A^\mu\Psi - \frac{1}{4}F_{\mu\nu}F^{\mu\nu} \\ F_{\mu\nu} = \partial_\mu A_\nu - \partial_\nu A_\mu\,. \end{gathered} \tag{2.4}$$

The vector field A_μ, introduced in this equation, is the electromagnetic field and it allows us to achieve the desired invariance. The term $e\bar{\Psi}\gamma_\mu A_\mu\Psi$ describes the interaction between this field and the particle, and the term $F_{\mu\nu}F^{\mu\nu}$ represents the kinetic energy of the field itself in accordance with the Maxwell's equations for the electromagnetic interactions.

The development of the gauge theory continued with the works of Fermi, Dirac, Fock and Heisenberg. It was finally formulated in 1954 in the work of Chen Ning Yang and Robert Lauren Mills [40]. At first, the Yang-Mills theory did not find any application in quantum field theories, and it had some internal problems, like the unability of quantization for non-abelian groups (e.g. $SU(2)$, which by that time was already proposed for the weak interaction). The quantization of the Yang-Mills fields for non-abelian groups was done later with the help of the previous works of Ludvig Faddeev and Victor Popov who introduced the so-called Faddeev-Popov ghostss [41].

The first inclusion of the weak interaction was attempted by Enrico Fermi in 1933s [42]. His theory didn't include any interaction carriers but had particles interacting directly in one vertex. And while it described the results of the β-decay remarkably well, the need for a more elaborate description of different occurrences of the new type of interaction became gradually stronger as new experimental data was collected. The most notable was the "Wu experiment" conducted in 1956 by Chien-Shiung Wu which established the violation of the P-symmetry[1] [43]. The next attempt to develop a theory was made a year later by Robert Marshak and his student George Sudarshan. They never published it though, so the authorship is widely attributed to Richard Feynman and Murray Gell-Mann who published it in 1958 [44]. They developed a theory that was called a $V - A$ theory (as "vector minus axial vector") after the main term of the Lagrangian that described the interaction.

In 1964 the CP violation[2] was observed in the kaon experiment by James Cronin and Val Fitch [45]. The $V - A$ theory couldn't explain it, so there was a need to either update the $V - A$ theory or to introduce the new theory of some "superweak interaction". And at first, such superweak theories were developed, so when the new theory (that later became the QED theory) was developed by Sheldon Glashow, Steven Weinberg, and Abdus Salam in 1968 [46], that was based on the gauge Yang-Mills theory, it wasn't accepted (the paper, that would later become the most cited physical paper in history, saw only a couple of citations in the first three years). By that time the theory had several internal problems, but most importantly, it also wasn't able to describe the CP-violation. The first important advantage of the new theory was gained in 1972, when Gerard 't Hooft and Martinus Veltman proved that the Yang-Mills fields were renormalizable[3] [47]. They shared a Nobel prize for that work in 1999. And it was finally accepted in 1973, when the Gargamelle bubble chamber at CERN presented the direct evidence of the existence of neutral currents, that were predicted by their theory [48]. The new gauge bosons, W and Z, were directly observed only in 1983 [2]. In the same 1973 the first works that proved that the gauge theory can explain the CP-violation if the third generation of quarks were to be added appeared. This discovery would be further discussed in the following section.

---

[1] The "P-symmetry", or "parity symmetry" is the idea that the quantum processes would remain the same if we swap "left" and "right". The processes that make difference between "left" and "right" are said to "violate the P-symmetry".

[2] Much like the P-symmetry, the CP-symmetry is the idea that the processes would remain the same if we change both the parity and the charges, i.e. change the matter into antimatter and vise versa. The CP-symmetry was introduced after the confirmation of the P-symmetry violation as the new fundamental symmetry of the quantum processes.

[3] The renormalization of the theory is important for the use of the perturbation theory to predict the outcomes of the interactions. If the theory is not remormalizable, the integrals produced by the perturbation theory will divergent.

2.1.2 Quantum Chromodynamics (QCD)

The firsts works on the theory of the strong interactions started even before this interaction was first observed, as a theoretical explorations of the possibilities of the $SU(3)$ groups in particle physics. The need for the new theory first arose in 1947 after the discovery of the K-mesons in cosmic rays [49]. The first attempts to include the new experimental data in the existing theories were made by suggesting that the new interaction is the same as the EM interaction in nature, but with massive carriers. Considering that

$$\Delta E \cdot \Delta t = (m_q c^2) \cdot \Delta t \approx \hbar \,, \tag{2.5}$$

where m_q is the mass of the field quantum and Δt is its lifetime, and considering that $r = c \cdot \Delta t$ where the radius of the strong interaction was predicted to be $r = 10^{-15}$ m we will get the predicted value for the carrier mass as

$$m_q c^2 \approx \frac{\hbar c}{r} \approx 200\,\mathrm{MeV} \,. \tag{2.6}$$

The theoretical works predicting the massive carrier for the strong nuclear force were done by Hideki Yukawa in 1935 [50]. In 1947 π^+-meson was observed with the mass of 140 MeV [51], which initially was thought to be the carrier of the strong interaction. Although technically it wasn't true, the discovery of π-mesons played a big role in the foundation of the QCD, and Yukawa got a Nobel prize in 1949 for his work. Later, in 1950 the Λ^0-baryons were observed in experiments conducted by Victor David Hopper and Sukumar Biswas. These particles had a much longer lifetime than the theories predicted, and it was proposed that they have some new, unknown charge which was called "strange". The number of new particles observed experimentally grew steadily, and there were no successful attempts to fit them into the $SU(2)$ groups.

In 1961 Yuval Ne'eman [52] and later in 1962 independetly Murray Gell-Mann [53] proposed a new hadron classification model, the so-called "eightfold way". It was based on the $SU(3)$ group, and among other things, predicted the Ω-baryon as part of the baryon decuplet. This baryon was found in 1964 with the mass and properties predicted by the model [54]. Yet, the fundamental elements of the $SU(3)$ group were still not described be the theory. This problem was solved with the introduction of the quark model independently by Murray Gell-Mann [55] and George Zweig [56] in 1964. The quark model still had several flaws though. First of all, the quarks were never observed experimentally. Second, only the $q\bar{q}$ and qqq states were observed, no qq or $qqqq$. There were no rules that forbade such states. And the main issue was the flaws within the theory itself. For example, according to the theory, the Δ^{++}-baryon consisted of three quarks (uuu) with the spin 1/2, which violated the Pauli principle. To solve this problem, there was introduced another charge, called "color". It was first proposed by Oscar W. Greenberg in 1964 as an independent $SU(3)$ group of color charges [57]. This idea was developed for several years and eventually laid the foundation for the modern QCD theory. Murray Gell-Mann got the Nobel prize in 1969 for his works in this field.

In the same year 1964, several works predicted the existence of the fourth quark as part of the quark-lepton symmetry. The prediction is usually credited to Sheldon Glashow, John Iliopoulos and Luciano Maiani for their work on flavor-changing neutral currents that was published in 1970 [58]. The proposed mechanism (the GIM mechanism, for the first letters in the authors names) required the forth quark to exist.

Also in 1964 the works started on the CP-violation in K-meson decays. The important work was done by James Watson Cronin and Val Logsdon Fitch who received the Nobel prize for it in 1980. The works on CP-violation were continued by Makoto Kobayashi and Toshihide Maskawa who based it on the work of Nicola Cabibbo on weak interactions, and added a third generation of quarks. They published their work in 1973 [59].

In the same year David Gross and Frank Anthony Wilczek [60] and independently Hugh David Politzer [61] published their works on asymptotic freedom in strong interaction, which solved the so-called “Landau-pole” problem, which suggested that the interactions should become infinitely strong at certain scale. These works allowed to predict the results of the deep inelastic scattering by the means of perturbative theory. They shared a Nobel prize in 2004 for that work.

In 1974 the J/ψ meson was first observed independently in SLAC [62] and BNL [63]. This particle had a width of a mass peak much smaller that the theory predicted for a particle of this mass. The only explanation for this was an assumption, that the particle was a bound state of an unknown heavy quark that was called “charm” (or c-quark).

The bound state of the second heavy quark - the Υ-meson, was discovered in 1977 in Fermilab [64]. The last predicted quark was searched for for the next twenty years because of its very high mass. Only in 1995 it was jointly confirmed by two detectors (DZero and CDF) on Tevatron collider at Fermilab [3].

Makoto Kobayashi and Toshihide Maskawa got a Nobel prize in 2008 for their work.

2.2 Parton Distribution Function (PDF)

The processes observed in the high-energy collisions suggest that the hadrons are complex particles that consist of several partons. The term “parton” was first proposed by Richard Feynman in 1969 as a generic term for every particle that constitutes hadrons, they are called quarks and gluons now. At first, the hadrons were believed to consist of duplets ($q\bar{q}$) and triplets (qqq) of quarks. But, through the interaction processes, these quarks (also called the valence quarks) can also produce an arbitrary number of the lower-energy virtual partons, also called “sea” quarks and gluons. The sea partons were first observed by James Bjorken and Emmanuel Paschos in 1969 [65].

Every parton within the hadron carries some amount of its energy. So in order to predict the results of the deep inelastic scattering involving a hadron we need to calculate which parton will be participating in the scattering and what fraction of the hadron’s energy it carries. These parameters can’t be derived from the theory in any way, they can only be produced based on the experimental data, which leaded to the creation of the parton distribution functions.

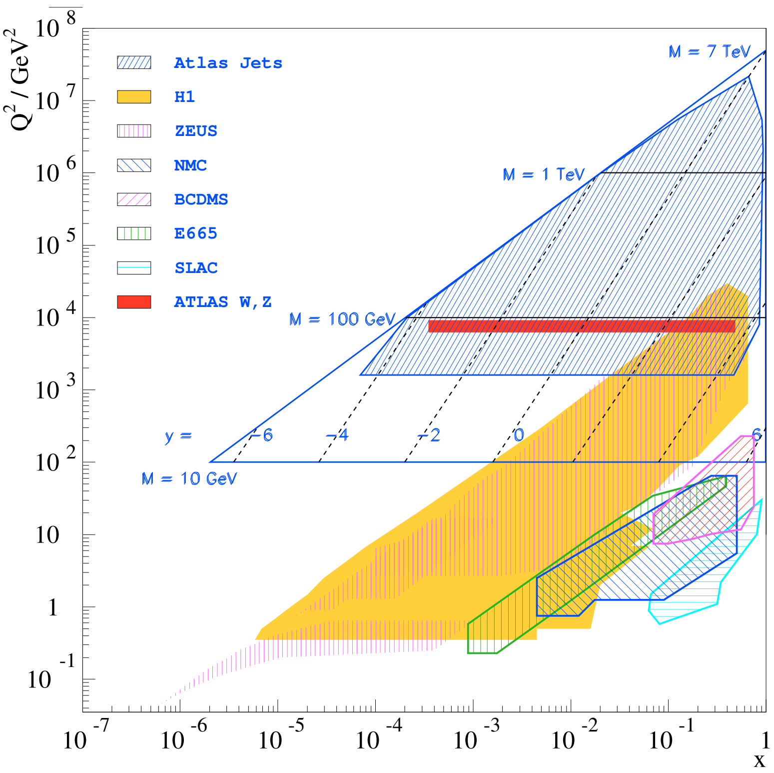

Figure 2.2: The kinematic plane of various collider experiments in Q^2 and x. In red the range for Z and W production in ATLAS is shown.

The PDF is a function which allows to find the probability density of finding the given parton in the given hadron with a given momentum. In the collision experiments the most interest represent the proton PDFs which are constructed based on the experimental data from the ep, pp and $p\bar{p}$ scattering. The proton PDFs depend on two parameters: "Q^2" and "Bjorken x" (or just "x"). The Q^2 corresponds to the energy scale of the collision process, and x represents the momentum fraction of the proton that the interacting parton holds. The constructed PDFs are only applicable for the certain range of Q^2 and x, which depends on the range coverage of the data they were based on. The coverage of the kinematic plane in Q^2 and x of various experiments is shown in Figure 2.6. The red stripe in the middle is the W and Z boson production in ATLAS. It can be seen that the Q^2 is very narrow, because these analyses only cover a mass window of $46 < M < 150$ GeV (and even less so in case of central-forward analysis), while the x coverage is quite large. As it can be seen on the plot, the x parameters is tied to the boson rapidity, which in turn translates to the pseudorapidity of the decay products (which are electrons, in case of $Z \to ee$). The rapidity y and pseudorapidity η are defined as:

$$\begin{aligned} y &= \frac{1}{2}\log\left(\frac{E+p_z}{E-p_z}\right) , \\ \eta &= -\log(\tan(\frac{\theta}{2})) . \end{aligned} \tag{2.7}$$

The y coverage of the $Z \to ee$ central-central analysis (as well as $Z \to \mu\mu$ and $W \to e\nu$) is

$|y| < 2.4$, while the coverage of $2.4 < |y|$ is achieved solely by $Z \to ee$ central-forward, so the central-forward analysis is very important in achievement of the large x coverage.

The coverage of the PDFs can be increased by the use of the evolution equations, such as DGLAP. To accurately predict the results of hadron scattering the set of 13 different PDFs is required, one for each of the 12 quarks ($\bar{t}$, $\bar{b}$, $\bar{c}$, $\bar{s}$, $\bar{u}$, $\bar{d}$, d, u, s, c, b, t) and one for the gluons. The color of the partons can't be determined, so the PDFs are integrated over this degree of freedom. The PDFs for t and $\bar{t}$ are set to zero because of the high mass of the top quark. The PDFs for b, $\bar{b}$, c and $\bar{c}$ are only non-zero for $Q^2 \gg (m_b)^2$.

Sets of PDFs are released by several groups, who utilize similar fitting techniques and are based on the experimental data. Among recent releases can be noted these of the CTEQ collaboration [66], the MSTW group [67, 68] (who also released the MMHT PDF set [69]), the ABM group [70]. They provide the sets for different levels of radiative corrections and also $\alpha_S(M_Z)$ determinations. The HERAPDF group not only released the sets, but also opened their fitting framework for other experiments in order to produce a global fits [71]. The NNPDF group used a neural network approach to determine the PDFs with unbiased parameterization [72–74]. The sets are distributed with the LHAPDF software [75], which represents the full compendium of PDF sets calculated and validated by this time. Most significant contributions to the PDF collection were done by the Tevatron and HERA experiments.

2.3 *pp* collisions and Z boson production

The proton-proton collisions are the ones that take place at the LHC. At low energies, the *pp* collision looks like elastic scattering of two charged particles. But on the energies achievable in the LHC, the predominant processes are deep inelastic, which means that the internal structure of the proton starts to play a key role.

The process of the *pp* collision is schematically shown on Figure 2.3. The three stages of the collision can be calculated by theory, with the use of the perturbative theory, but the difficulty of such calculations at high orders of the perturbative expansion makes it practically impossible to do. The three processes are calculated separately, with initial and final state radiations being calculated by the approach called the parton shower: the radiation process of each quark is calculated independently. The hard scattering itself can be calculated in leading order (LO, no radiative corrections, also called "born-level" and "tree-level"), next to leading order (NLO, first order radiative corrections), next to next to leading order (NNLO) and so on. Most commonly one radiative correction is used (NLO), which gives a result with an acceptable uncertainty, and is not difficult to calculate.

The process of the Z boson production in the Drell-Yan process is shown on Figure 2.4. The process in leading order involves only a quark and an antiquark producing a boson which in turn decays into a lepton-antilepton pair.

To properly calculate a theoretical prediction for such a process, the PDFs must be applied to both interacting protons. This is common problem of hadron colliders as opposed by lepton or *ep* ones (while *ep* colliders do need PDFs, they depend on it much less than the *pp* ones).

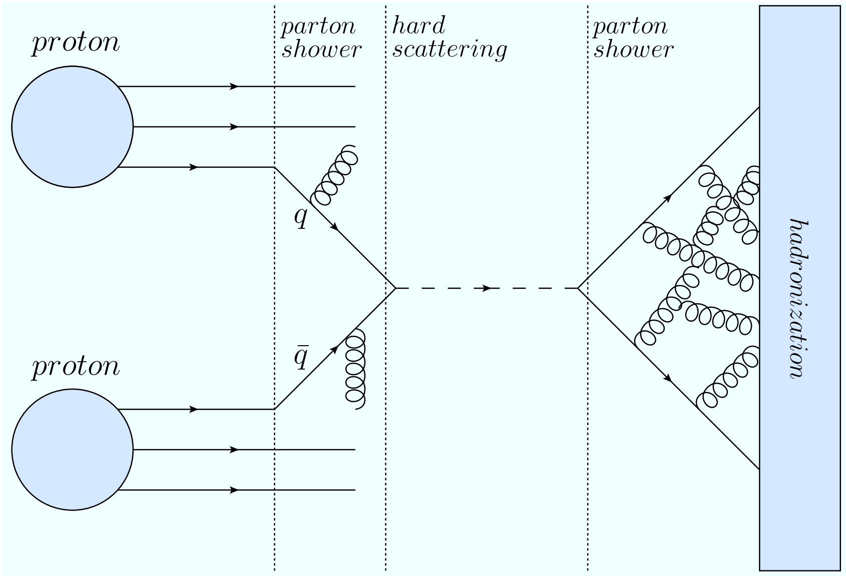

Figure 2.3: The deep inelastic scattering of two protons. The three main phases of the process are shown: initial radiation, the hard scattering itself, when the gauge boson is produced, and a final state radiation. If the gauge boson decayed into quarks, the hadronization process takes place in the end, when these quarks decay into color-neutral hadrons.

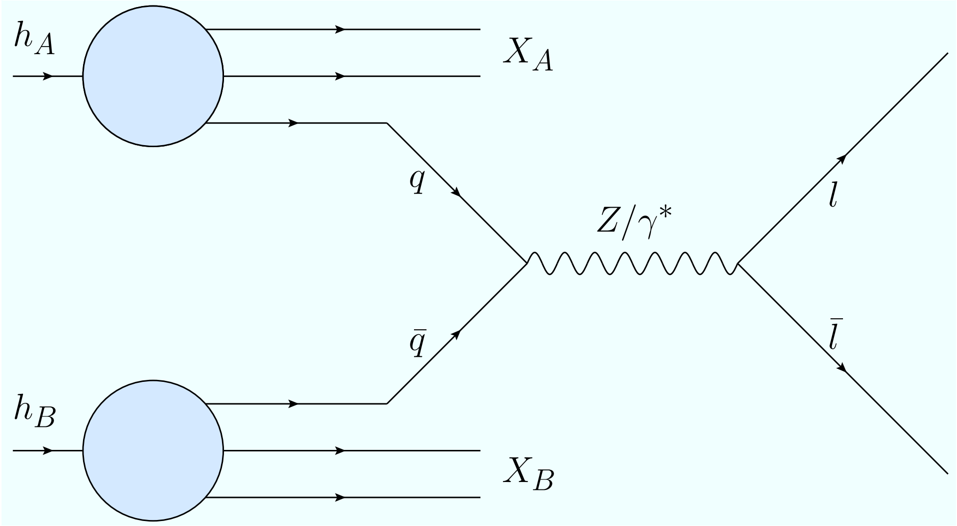

Figure 2.4: The Drell-Yan process in leading order. A quark from one hadron and an anti-quark from another annihilate and produce a vector boson (photon or Z) which decays into lepton-antilepton pair. The remaining quarks of the initial hadrons do not interact between each other.

But because of its high rest mass, hadrons can be accelerated to the much higher energies, which makes hadron colliders still preferable for certain tasks despite this shortcoming.

2.4 Theoretical predictions for the $Z \to ee$ cross-section

There are several processes in *pp*-collisions where the events can be clearly filtered from the background. The $W \to e\nu$ and $Z \to ee$ decays are the examples of such processes. $Z \to \ell\ell$ decay process in particular is widely used to test the various aspects of the standard model, since the decay is purely leptonic, and also can be easily theoretically predicted. The M_Z is calculated to a very high precision, as well as Γ_Z. ATLAS detector has a very good resolution for electrons, photons and muons, and the reconstruction of these particles has very good efficiency. Also, the $Z \to ee$ Drell-Yan process has a resonance in LHC, which helps to filter the events.

While the $Z \to \ell\ell$ measurement can be used for several things, including the determination of α constant and forward-backward asymmetry, the main application for the measured cross-section itself would be the PDF fits. The theoretical prediction for the cross-section of the Drell-Yan $Z/\gamma^* \to ee$ process at LO is as follows [76]:

$$\frac{d^2\sigma}{dM_{ee}dy} = \frac{4\pi\alpha^2(M_{ee})}{9} 2M_{ee} \cdot P(M_{ee}) \cdot \Phi(x_1, x_2, M_{ee}^2)\,. \tag{2.8}$$

Here M_{ee} is the mass of the boson, y is the boson rapidity, $P(M_{ee})$ is the propagator term and $\Phi(x_1, x_2, M_{ee}^2)$ - the parton distribution function depending on the x parameter of both quark and antiquark. This cross-section is a sum of contribution from both Z and γ^* process as well as their interference. For the photon process the propagator and the PDF are given as

$$P_\gamma(M_{ee}) = \frac{1}{M_{ee}^4}\,, \quad \Phi_\gamma = \sum_q e_q^2 F_{q\bar{q}}\,. \tag{2.9}$$

It can be seen that the propagator term P_γ suppresses the photon contribution for the high-mass ($M_{ee} \gg M_Z$) and the mass peak ($M_{ee} \approx M_Z$) analyses.

For the Z/γ interference contribution the same terms can be given as

$$\begin{gathered} P_{Z\gamma}(M_{ee}) = \frac{k_Z \cdot v_e \cdot (M_{ee}^2 - M_Z^2)}{M_{ee}^2 \cdot ((M_{ee}^2 - M_Z^2)^2 + (\Gamma_Z M_Z)^2)}\,, \quad \Phi_{Z\gamma} = \sum_q 2e_q v_q F_{q\bar{q}}\,, \\ k_Z = \frac{1}{4\sin^2\theta_W \cos^2\theta_W}\,, \quad \cos\theta_W = \frac{M_W}{M_Z}\,, \end{gathered} \tag{2.10}$$

Where θ_W is a weak mixing angle, M is the mass, and Γ is the width of the Breit-Wigner distribution, which corresponds to the width of the mass peak. The contribution of this component is proportional to the vector coupling of the electron v_e, which is close to zero, so the contribution is also suppressed.

And finally for the $Z \to ee$ process itself the terms are as follows:

$$P_Z(M_{ee}) = \frac{k_Z^2 \cdot (v_e^2 + a_e^2)}{(M_{ee}^2 - M_Z^2)^2 + (\Gamma_Z M_Z)^2}\,, \quad \Phi_Z = \sum_q (v_q^2 + a_q^2) F_{q\bar{q}}\,. \tag{2.11}$$

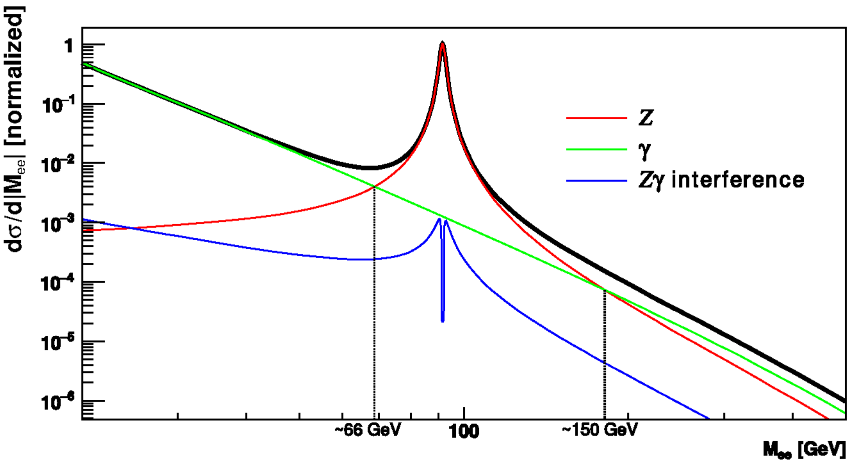

Figure 2.5: The theoretical predictions for the cross-sections of the Drell-Yan $Z/\gamma^* \to ee$ processes, normalized to $Z \to ee$ peak value. The cross-sections were calculated in leading order, using the CT10 PDF set.

As it is seen from (2.8), the PDFs are included in the cross-section formula as a direct factor, so the double-differential cross section can be directly used in PDF fits.

All the cross-sections can be seen together on Figure 2.5. The cross-section for $Z \to ee$ process is higher than that of $\gamma^* \to ee$ only around the peak region, starting from ∼66 GeV up to ∼150 GeV. The region is divided into two: the peak region (66 – 116 GeV) and the high mass region (116 – 150 GeV). The boundary between the regions is picked in such a way that the Z boson mass was at the center of the peak region.

The PDF decomposition of the two dominant processes is shown on Figure 2.6. There, the contribution from the various quarks to the final cross-section is shown. It can be seen that $Z \to ee$ central-central cross-section is dominated by $d\bar{d}$ interactions, while in case of the central-forward the $u\bar{u}$ is larger. For the $\gamma^* \to ee$ cross-section the $u\bar{u}$ interactions are by far the largest contributors.

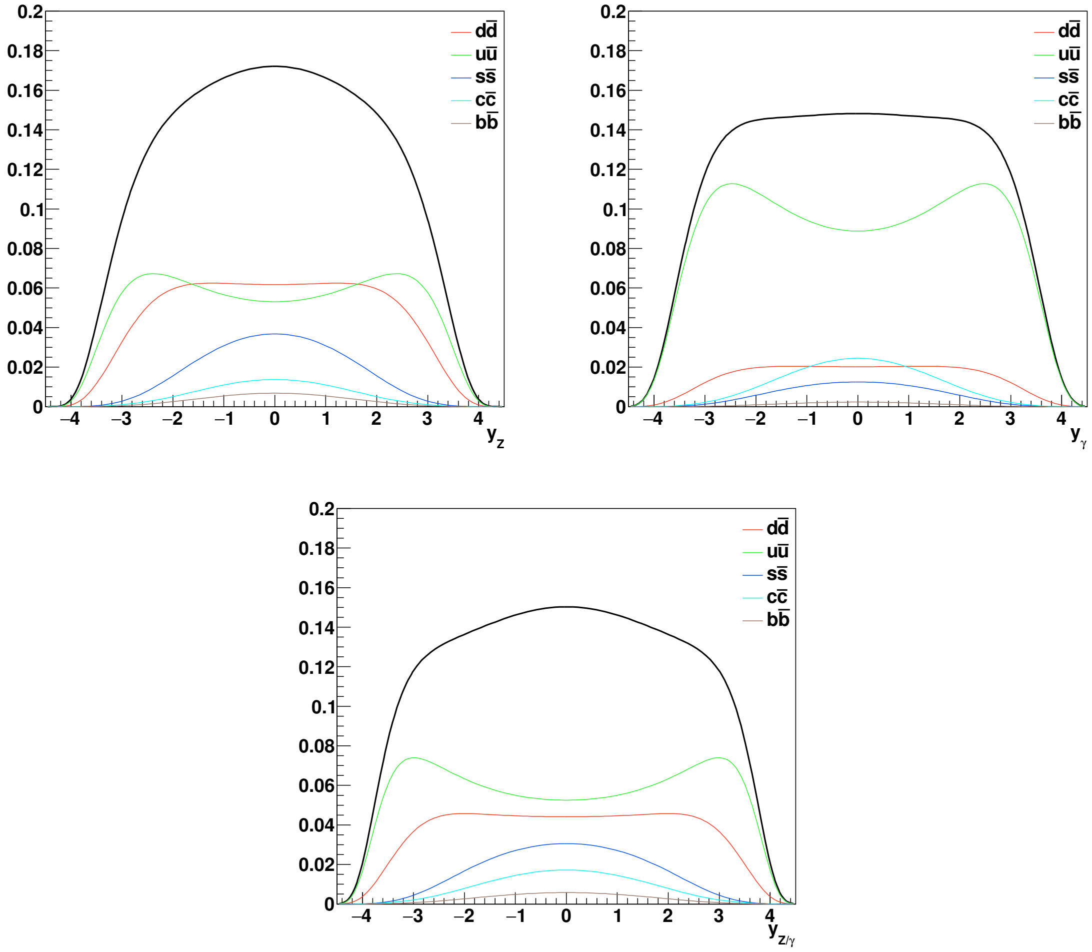

Figure 2.6: The PDF decomposition of the normalized cross-sections of the Drell-Yan processes. The decomposition of the $Z \to ee$ (left), $\gamma^* \to ee$ (right) and Z/γ interference (bottom) processes are shown. The cross-sections were calculated in leading order, using CT10 PDF set

CHAPTER 3

The LHC (Large Hadron Collider)

The LHC is the largest circular synchrotron collider in the world, which is designed to deliver *pp* collisions with energies up to 14 TeV and instantaneous luminosity up to 10^{34} cm^{-2}s^{-1}. The instantaneous luminosity represents the proportionality of the event rate and the cross-section for a given process: $N = \mathcal{L} \cdot \sigma$. The parameters is thus process-agnostic, and describes the collider itself in a way that it helps to estimate the amount of collisions happening in the detector. The consequence of the large $\mathcal{L}$ is a pileup, which is the amount of collisions per detector readout. With the increasing of the luminosity, the pileup also increases, flooding the detector with the particles from several simultaneous *pp*-collisions, making it hard to reconstruct the event. The techniques to overcome the pileup problem will be discussed in Section 8.

The LHC complex includes several accelerators with different sizes of rings which gradually increase the energy of the particles. All of them are shown on the Figure 3.1.

The full acceleration process of the protons looks like this:

1. The protons are injected into the Linear Accelerator 2 (Linac2). In case of lead ions Linac3 is used.
2. In case of protons, the bunches are then accelerated in the Proton Synchrotron Booster (Booster), while for heavy ions the Low Energy Ion Ring (LEIR) is used. Both of them pass the accelerated particles to Proton Synchrotron (PS) for storage until the needed amount of particles is pre-accelerated.
3. Next is the Proton Synchrotron - the first high-energy accelerator in this chain, its outputs is 25 GeV, and it was the largest CERN accelerator up until 1970s.
4. The next is the last preparatory accelerator in chain: the Super Proton Synchrotron (SPS). It also once was the most prominent CERN collider and, among other things, lead to the discovery of W and Z bosons during the experiments with $p\bar{p}$ collisions. Its output energy is 450 GeV.

After LHC is filled with the pre-accelerated particles, it starts its own acceleration process. It takes about 20 minutes to reach the energy of 3.5 TeV on which the collision took place during 2011. Next is preparatory stage during which the bunches are focused in order to increase

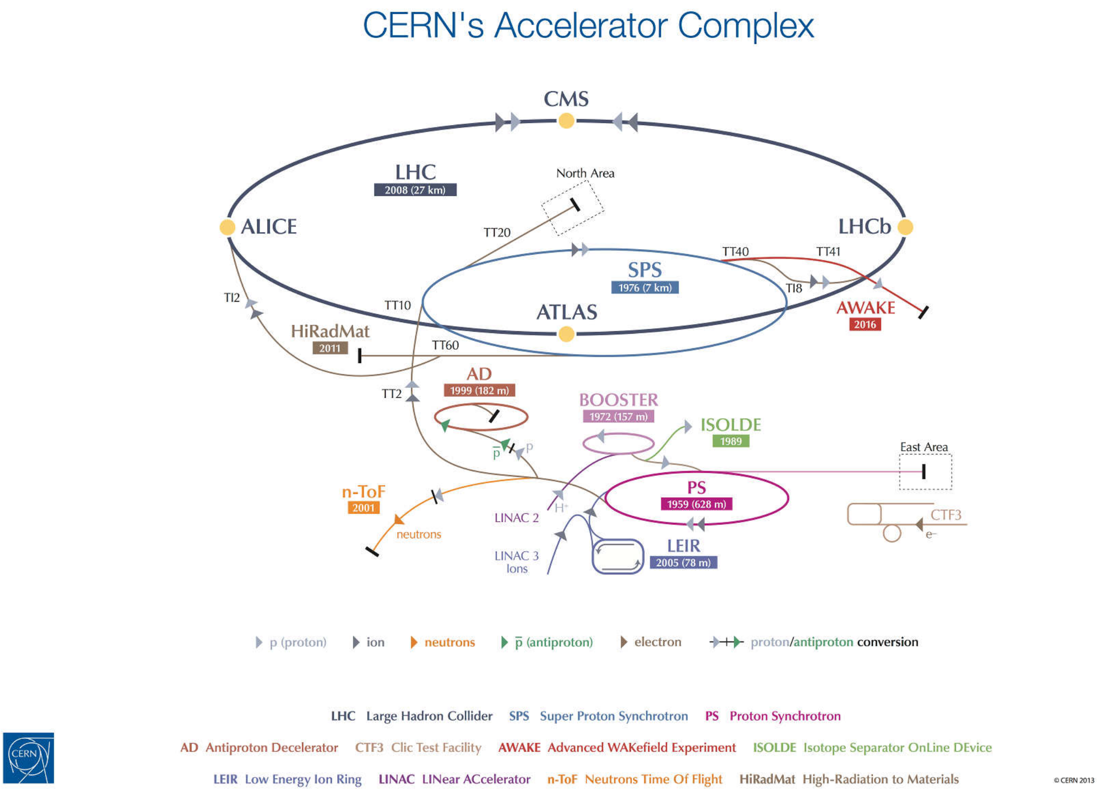

Figure 3.1: The LHC accelerator complex. For each accelerator the year of completion is shown. For circular accelerators the length of the ring is also shown. [77]

luminosity. If all goes well, the LHC goes into the state of "stable beams": the collisions are started and the detectors can start recording the data. Eventually, the beams loose their focus, the data-taking then stops, and the beams are dumped. The data-taking period is usually several hours long (up to 20) and ideally it lasts as long as the beams circulate the ring, but sometimes other problems arise which prevent data-taking for a period of time during the circulation.

There are 6 detectors which record data from the collisions on LHC.

- **ALICE (A Large Ion Collider Experiment)** This detector is designed to analyze heavy-ion collisions.
- **ATLAS (A Toroidal LHC ApparatuS) and CMS (Compact Muon Solenoid)** These are two general-purpose detectors which cover a wide range of HEP fields. They have differences in design though: ATLAS has less matter in the calorimeter and better muon detectors, while CMS is twice as heavy as ATLAS (has twice as much matter) and because of this has better EM calorimeter, but the detection of hadrons and muons is less precise.
- **LHCb (LHC-beauty)** This detector studies the b-quarks.
- **LHCf (LHC-forward)** This detector studies the forward particles, which behave similar to cosmic rays.
- **TOTEM (TOTal Electric and diffractive cross-section Measurement)** This detector measures the total *pp* cross-section.

Each detector operates independently from one another to enable cross-checking between experiments and increase the trustworthiness of the results.

During 2011 the LHC operated with the same energy of 3.5 TeV per beam and with more or less the same luminosity: the difference between the beginning of the data taking in april and the end in december is only about 4 times, as opposed to the ten thousand times, in which the luminosity increased during 2010 data taking. More on the data samples can be seen in Chapter 5.

CHAPTER 4

The ATLAS Experiment

The ATLAS detector is one of the two general purpose detectors at the LHC, and is designed for probing for p-p and heavy ion collisions. This detector represents the work of a large collaboration of several thousand physicists, engineers and technicians over a period of fifteen years of dedicated design, development, fabrication, installation and operation. There are several fields in which the researches are currently going in ATLAS collaboration, including Z and W boson decay, studies of the Higgs boson, supersymmetry, study on B-mesons, and others. This broad spectrum of researches makes high demands on the detector's complexity and the precision of the different sub-systems.

4.1 Physics requirements and detector overview

The ATLAS detector has a cylindrical shape, it is aligned along the beam line with the center situated at the interaction point. The coordinate system used to describe the detector follows its natural geometry: the interaction point is taken as an origin, while the z axis is put along the beam pipe, making the x-y plane transverse. The positive x-axis is defined to be pointing to the center of the LHC ring, and positive y-axis is defined to be pointing upwards. The direction on the z-axis is picked such as to form a right-handed coordinate system. The azimuthal angle φ is measured as usual around the beam axis, and the polar angle θ is the angle from the $z-$ axis.

The overview of the ATLAS detector is shown in the Figure 4.1. The main detector subsystems can be seen there: the innermost is the tracker, then goes the EM calorimeters, the hadronic calorimeters, and finally the muon spectrometers. There is also a magnet system, which is not a detector by itself, but is essential to the functioning of the whole system. All of the sub-detectors are briefly described below.

- The tracker (also called "the inner detector") records the tracks of the charged particles and is used to determine the charge and momentum.
- The EM calorimeters identify and measure the energy of EM particles: electrons, positrons and photons.

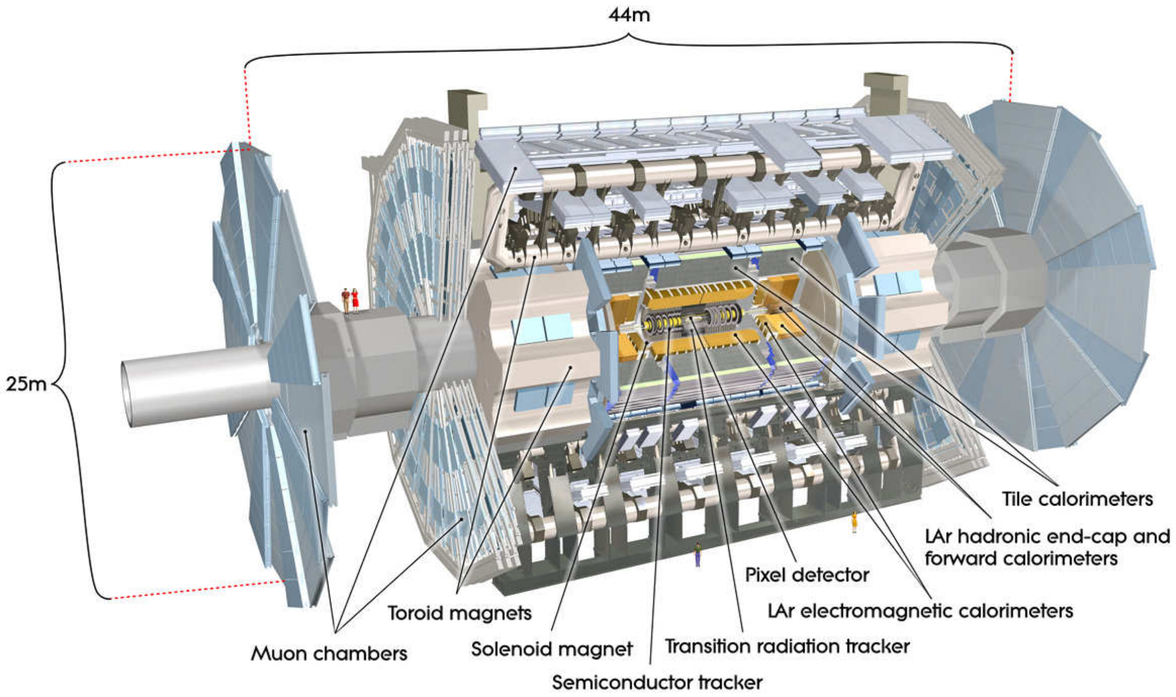

Figure 4.1: Overview of the ATLAS detector, with all the major sub-systems and the human-sized scale figures. [78].

- The hadronic calorimeters measure the energy of hadrons.
- The muon spectrometers identify and measure the energy, momentum and charge of the muons.

Based on their physical properties, different particles behave differently in these sub-detectors. The reconstruction of the particles rely heavily on the traces that particles leave in different parts of the detector.

- **Photons**, unless converted to the electrons, do not leave tracks in the tracker. Stop in the EM calorimeter and leave a narrow distinctive EM cluster of the deposited energy in it (the difference between EM and hadronic clusters can be seen in Figure 8.1).
- **Electrons** leave a track in the tracker, in the EM calorimeter behave similarly to photons: leave cluster with similar shape and properties.
- **Charged mesons and protons** leave a track in the tracker, leave a hadronic cluster in the EM calorimeter, which can be distinguished from the EM particles, stop in the hadronic calorimeter and possibly leaving a cluster in it.
- **Neutral mesons and neutrons** do not leave a track, leave a cluster in the EM calorimeter, distinguished by a relatively long decay time.

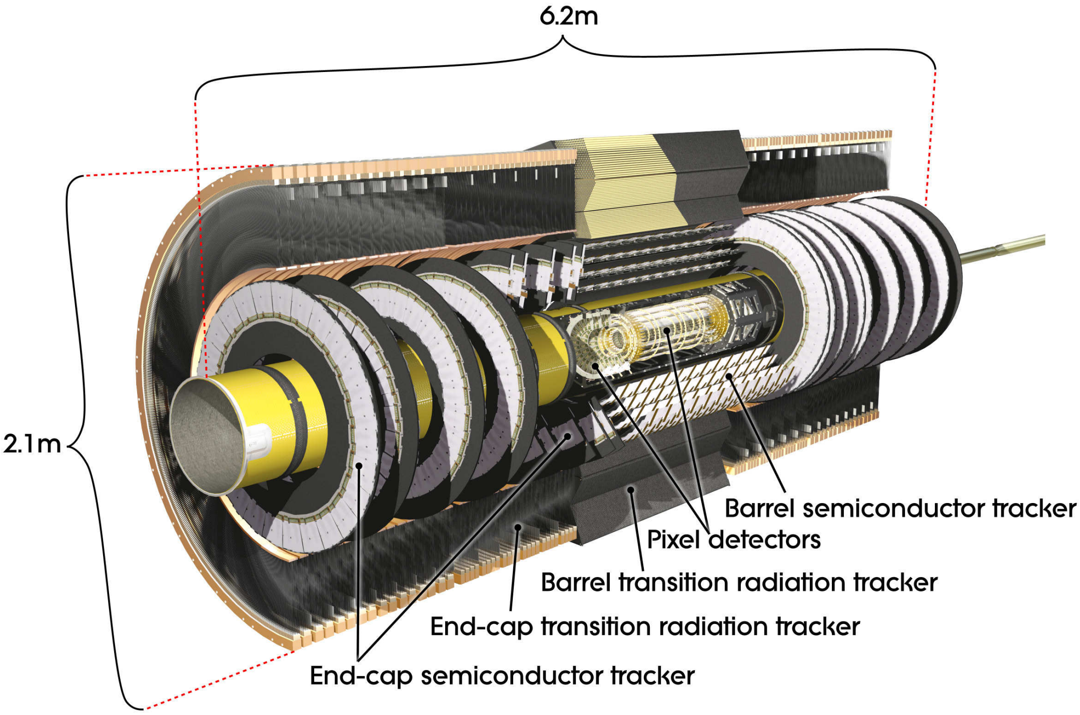

Figure 4.2: Overview of the ATLAS tracker. The SCT, TRT and pixel detectors are shown there. [78].

- **Muons** leave a track, leave a recognizable cluster in the calorimeters, which is associated with the so-called "minimum ionizing particles" (MIP), propagate further to the muon chambers and usually are not stopped by the detector.
- **Neutrinos** do not interact with the detector, and leave it without any traces. Are identified by the missing transverse energy.

Z-bosons are short-lived, and do not interact even with the innermost parts of the detector. What we detect and record are the decay products of the said particles.

4.2 Tracking

Because of the very high number of the events per second, the density of the tracks inside the inner detector is also very high. There are approximately 1000 particles from the collision point every 25 ns within the central eta region. To achieve the desired momentum and vertex resolution, high-precision measurements must be made with fine detector granularity. The tracker of the ATLAS detector consists of pixel and silicon microstrip (SCT) trackers, and the Transition Radiation Tracker (TRT). Combined they provide these features.

The layout of the tracker is illustrated in Figure 4.2. Its basic parameters are summarized in Tab. 4.1. The magnetic field with the intensity of 2 T generated by the central solenoid covers most of the tracker: it extends over a length of 5.3 m with a diameter of 2.5 m. The

Item		**Radial extension (mm)**	**Length (mm)**
Overall tracker envelope		$0<R<1150$	$0<\|z\|<3512$
Beam-pipe		$29<R<36$	
Pixel	Overall envelope	$45.5<R<242$	$0<\|z\|<3092$
3 cylindrical layers	Sensitive barrel	$50.5<R<122.5$	$0<\|z\|<400.5$
$2*3$ disks	Sensitive end-cap	$88.8<R<149.6$	$495<\|z\|<650$
SCT	Barrel envelope	$255<R<549$	$0<\|z\|<805$
	End-cap envelope	$251<R<610$	$810<\|z\|<2797$
4 cylindrical layers	Sensitive barrel	$299<R<514$	$0<\|z\|<749$
$2*9$ disks	Sensitive end-cap	$275<R<560$	$839<\|z\|<2735$
TRT	Barrel envelope	$554<R<1082$	$0<\|z\|<780$
	End-cap envelope	$617<R<1106$	$827<\|z\|<2744$
73 straw panels	Sensitive barrel	$563<R<1066$	$0<\|z\|<712$
160 straw panels	Sensitive end-cap	$644<R<1004$	$848<\|z\|<2710$

Table 4.1: The description of the geomentry of the ATLAS tracker [78].

precision tracking detectors (pixels and SCT) cover the region $|\eta| < 2.5$. As can be seen on the picture, they are arranged in concentric cylinders along the beam axis in the central area, while in the end-cap regions they are arranged in form of discs perpendicular to the beam. The highest granularity is achieved around the interaction point using silicon pixel detectors. The pixel layers are segmented in φ and z with typically three pixel layers crossed by each track. All pixel sensors are identical and have a minimum pixel size in $R - \varphi \times z - \varphi$ of 50×400 μm^2. The intrinsic accuracy in the central region are 10 μm (φ) and 115 μm (z) and in the end-cap regions are 10 μm (φ) and 115 μm (R). The pixel detector has approximately 80.4 million readout channels. For the SCT, eight strip layers (four space points) are crossed by each track. In the central region, this detector uses small-angle (40 mrad) stereo strips to measure both coordinates, with one set of strips in each layer parallel to the beam direction, measuring $R - \varphi$. They consist of two 6.4 cm long daisy-chained sensors with a strip pitch of 80 μm. In the end-cap region, the detectors have a set of strips running radially and a set of stereo strips at an angle of 40 mrad. The mean pitch of the strips is also approximately 80 μm. The intrinsic accuracy per module in the barrel are 17 μm (φ) and 580 μm (z) and in the disks are 17 μm (φ) and 580 μm (R). The total number of readout channels in the SCT is approximately 6.3 million.

A large number of hits (typically 36 per track) is provided by the 4 mm diameter straw tubes of the TRT, which enables track-following up to $|\eta| = 2.0$. The TRT only provides $R-\varphi$ information, for which it has an intrinsic accuracy of 130 μm per straw. In the central region, the straws are parallel to the beam axis and are 144 cm long, with their wires divided into two

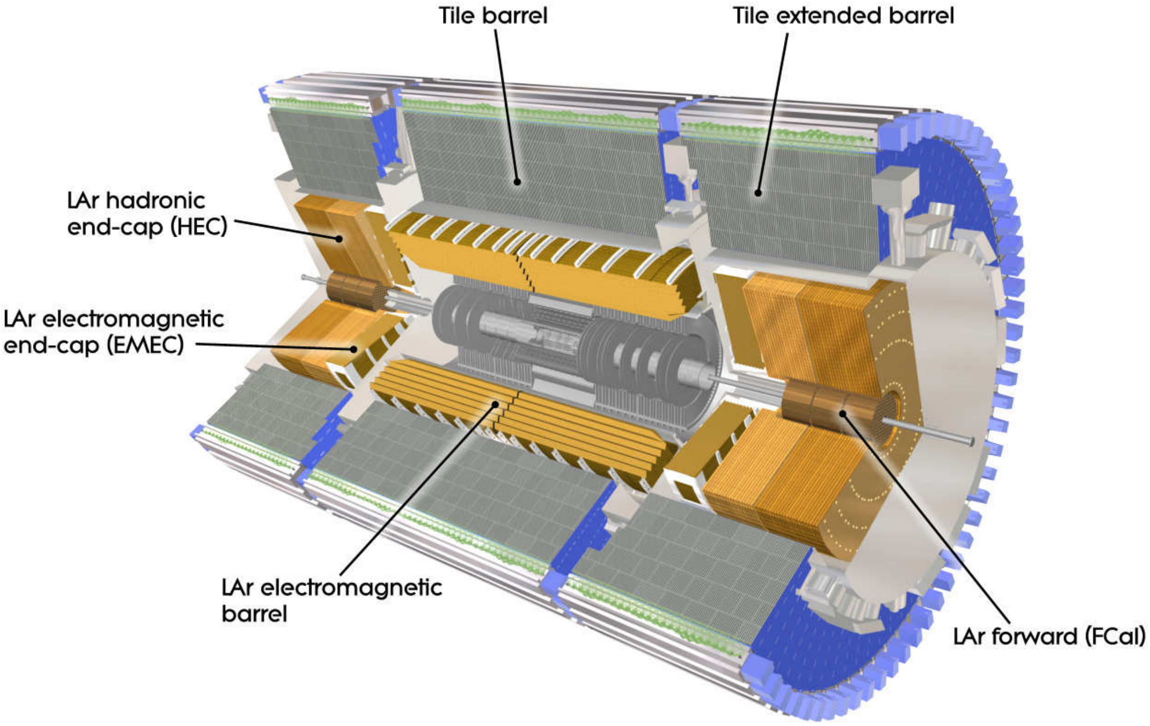

Figure 4.3: Overview of the ATLAS EM and hadronic calorimeters. [78].

halves, approximately at $\eta = 0$. In the end-cap region, the 37 cm long straws are arranged radially in wheels. The total number of TRT readout channels is approximately 351 thousands.

The combination of precision trackers close to interaction point with the TRT at a larger radius gives very robust pattern recognition and high precision in all $R\ \varphi$ and z coordinates. The straw hits at the outer radius contribute significantly to the momentum measurement, since the lower precision per point compared to the silicon is compensated by the large number of measurements and longer measured track length. The inner detector system provides tracking measurements in a range matched by the precision measurements of the electromagnetic calorimeter. The electron identification capabilities are enhanced by the detection of transition-radiation photons in the xenon-based gas mixture of the straw tubes. The semiconductor trackers also allow impact parameter measurements and vertexing for heavy-flavor and τ-lepton tagging. The secondary vertex measurement performance is enhanced by the innermost layer of pixels, at a radius of about 5 cm.

4.3 EM calorimeters

The EM calorimeter is divided into a barrel (central) part ($|\eta| < 1.475$) and two end-cap components ($1.375 < |\eta| < 3.2$), each housed in its own cryostat. The position of the central solenoid in front of the EM calorimeter demands optimization of the material in order to achieve the desired calorimeter performance. As a consequence, the central solenoid and the LAr calorimeter share a common vacuum vessel, thereby eliminating two vacuum walls. The barrel calorimeter consists of two identical half-barrels at positive and negative z, separated by a small gap (4 mm) at $z = 0$. Each end-cap calorimeter is mechanically divided into two coaxial wheels: an outer wheel covering the region $1.375 < |\eta| < 2.5$, and an inner wheel covering the region $2.5 < |\eta| < 3.2$. The EM calorimeter is a lead-LAr detector with accordion-shaped kapton electrodes and lead absorber plates over its full coverage. The accordion geometry provides complete φ symmetry without azimuthal cracks. The lead thickness in the absorber plates has been optimized as a function of η in terms of EM calorimeter performance in energy resolution. Over the region devoted to central analysis ($|\eta| < 2.5$), the EM calorimeter is segmented in three sections in depth. For the end-cap inner wheel, the calorimeter is segmented in two sections in depth and has a coarser lateral granularity than for the rest of the acceptance.

In the region of $|\eta| < 1.8$, a presampler detector is used to correct for the energy lost by electrons and photons upstream of the calorimeter. The presampler consists of an active LAr layer of thickness 1.1 cm in the barrel and 0.5 cm in the end-cap regions.

4.4 Hadronic calorimeters

The hadronic calorimeter consists of the tile calorimeter (the central part) and the hadronic end-cap calorimeter (HEC).

The tile calorimeter is placed directly outside the EM calorimeter envelope. Its central barrel covers the region $|\eta| < 1.0$, and its two extended barrels cover the range $0.8 < |\eta| < 1.7$. It is a sampling calorimeter using steel as an absorber and scintillating tiles as active material. Both barrel and extended barrels are divided azimuthally into 64 modules. Radially, the tile calorimeter extends from an inner radius of 2.28 m to an outer radius of 4.25 m. It is segmented in depth in three layers, approximately 1.5, 4.1 and 1.8 interaction lengths (λ) thick for the barrel and 1.5, 2.6, and 3.3 λ for the extended barrel. The total detector thickness at the outer edge of the tile-instrumented region is 9.7 λ at $\eta = 0$. Two sides of the scintillating tiles are read out by wavelength shifting fibers into two separate photomultiplier tubes. In η, the readout cells built by grouping fibers into the photomultipliers are pseudo-projective towards the interaction region.

The Hadronic End-cap Calorimeter (HEC) consists of two independent wheels per end-cap, located directly behind the end-cap electromagnetic calorimeter and sharing the same LAr cryostats. To reduce the drop in material density at the transition between the end-cap and the forward calorimeter (around $|\eta| = 3.1$), the HEC extends out to $|\eta| = 3.2$, thereby overlapping with the forward calorimeter. Similarly, the HEC η range also slightly overlaps that of the tile calorimeter ($|\eta| < 1.7$) by extending to $|\eta| = 1.5$. Each wheel is built from 32 identical wedge-shaped modules, assembled with fixtures at the periphery and at the central bore. Each wheel is divided into two segments in depth, for a total of four layers per end-cap. The wheels closest to the interaction point are built from 25 mm parallel copper plates, while those further away use 50 mm copper plates (for all wheels the first plate is half-thickness). The outer radius of the copper plates is 2.03 m, while the inner radius is 0.475 m (except in the overlap region with the forward calorimeter where this radius becomes 0.372 m). The copper plates are interleaved with 8.5 mm LAr gaps, providing the active medium for this sampling calorimeter.

4.5 Forward calorimeters

The forward calorimeter (FCAL) covers the biggest eta range ($3.1 < |\eta| < 4.9$) and combines both EM and hadronic parts.

It is integrated into the end-cap cryostats, as this provides clear benefits in terms of uniformity of the calorimetric coverage as well as reduced radiation background levels in the muon spectrometer. In order to reduce the amount of neutron albedo in the inner detector cavity, the front face of the FCAL is recessed by about 1.2 m with respect to the EM calorimeter front face. This severely limits the depth of the calorimeter and therefore calls for a high-density design. The FCAL is approximately 10 interaction lengths deep, and consists of three modules in each end-cap: the first, made of copper, is optimized for electromagnetic measurements, while the other two, made of tungsten, measure predominantly the energy of hadronic interactions. Each module consists of a metal matrix, with regularly spaced longitudinal channels filled with the electrode structure consisting of concentric rods and tubes parallel to the beam axis. The LAr in the gap between the rod and the tube is the sensitive medium. This geometry allows for excellent control of the gaps, which are as small as 0.25 mm in the first section, in order to avoid problems due to ion buildup.

4.6 Muon spectrometers

The conceptual layout of the muon spectrometer is shown in Figure 4.4. This system is based on the magnetic deflection of muon tracks in the large superconducting air-core toroid magnets, instrumented with separate trigger and high-precision tracking chambers. Over the range $|\eta| < 1.4$, magnetic bending is provided by the large barrel toroid. For $1.6 < |\eta| < 2.7$, muon tracks are bent by two smaller end-cap magnets inserted into both ends of the barrel toroid. Over the middle region $1.4 < |\eta| < 1.6$, usually referred to as the transition region, magnetic deflection is provided by a combination of barrel and end-cap fields. This magnet configuration provides a field which is mostly orthogonal to the muon trajectories, while minimizing the degradation of resolution due to multiple scattering. The anticipated high level of particle flux has had a major impact on the choice and design of the spectrometer instrumentation, affecting performance parameters such as rate capability, granularity, aging properties, and radiation hardness.

In the barrel region, tracks are measured in chambers arranged in three cylindrical layers around the beam axis; in the transition and end-cap regions, the chambers are installed in planes perpendicular to the beam, also in three layers.

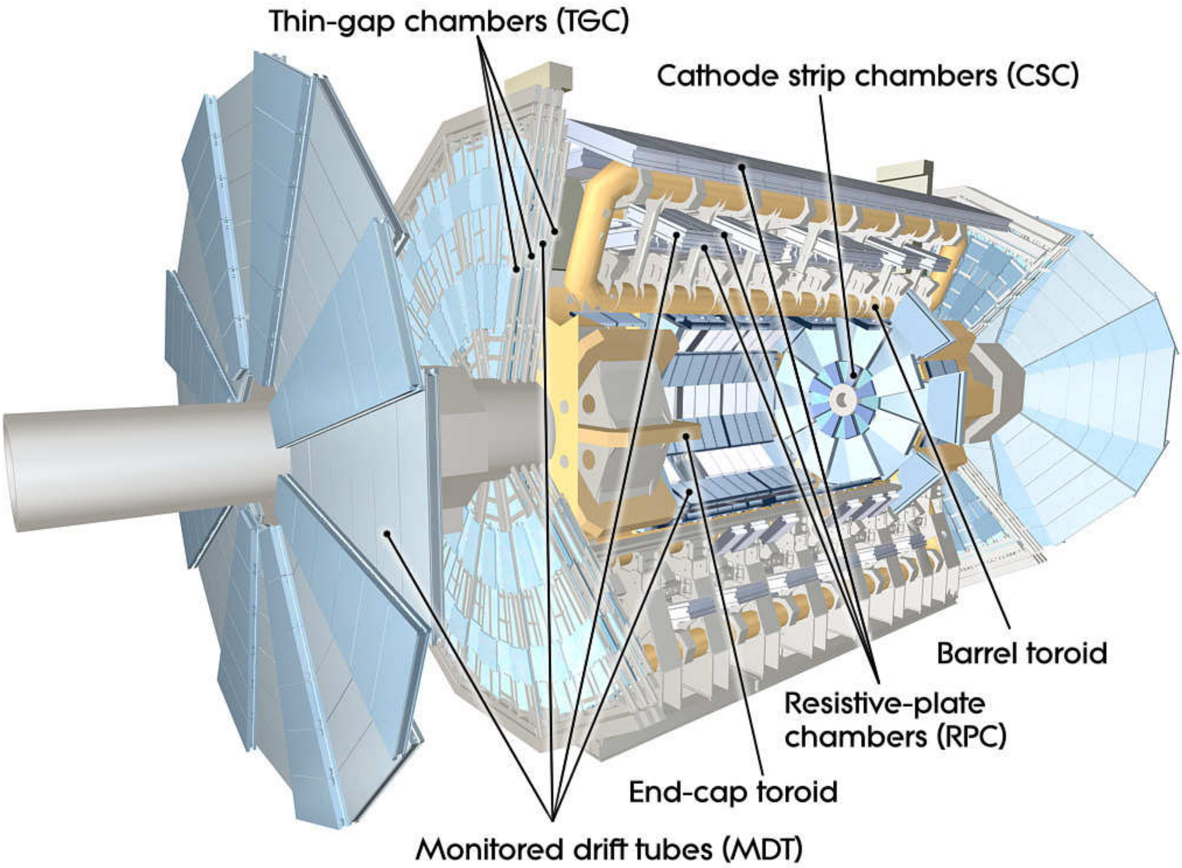

Figure 4.4: Overview of the ATLAS muon chambers. [78].

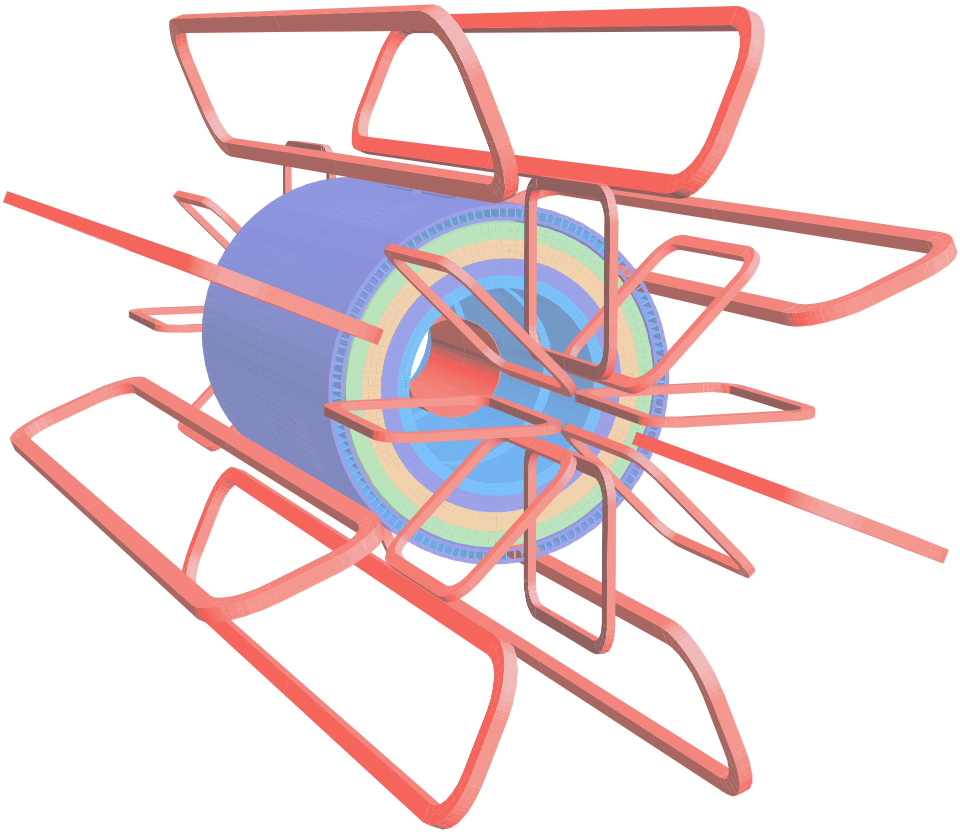

Figure 4.5: Overview of the ATLAS magnet system. [78].

4.7 Magnet system

ATLAS features a unique hybrid system of four large superconducting magnets. This magnetic system is 22 m in diameter and 26 m in length, with a stored energy of 1.6 GJ. This systems covers the volume approximately 12000 m^3 (defined as the region in which the field exceeds 50 mT), and engulfs all of the four main layers of detectors (as seen on Figure 4.1). The spatial arrangement of the coil wingdings is shown in Figure 4.5. The ATLAS magnet system consists of:

- a solenoid, which is aligned with the beam axis and provides a 2 T axial magnetic field for the inner detector, while minimizing the radiative thickness in front of the barrel electromagnetic calorimeter;
- a barrel toroid and two end-cap toroids, which produce a toroidal magnetic field of approximately 0.5 T and 1 T for the muon detectors in the central and end-cap regions, respectively.

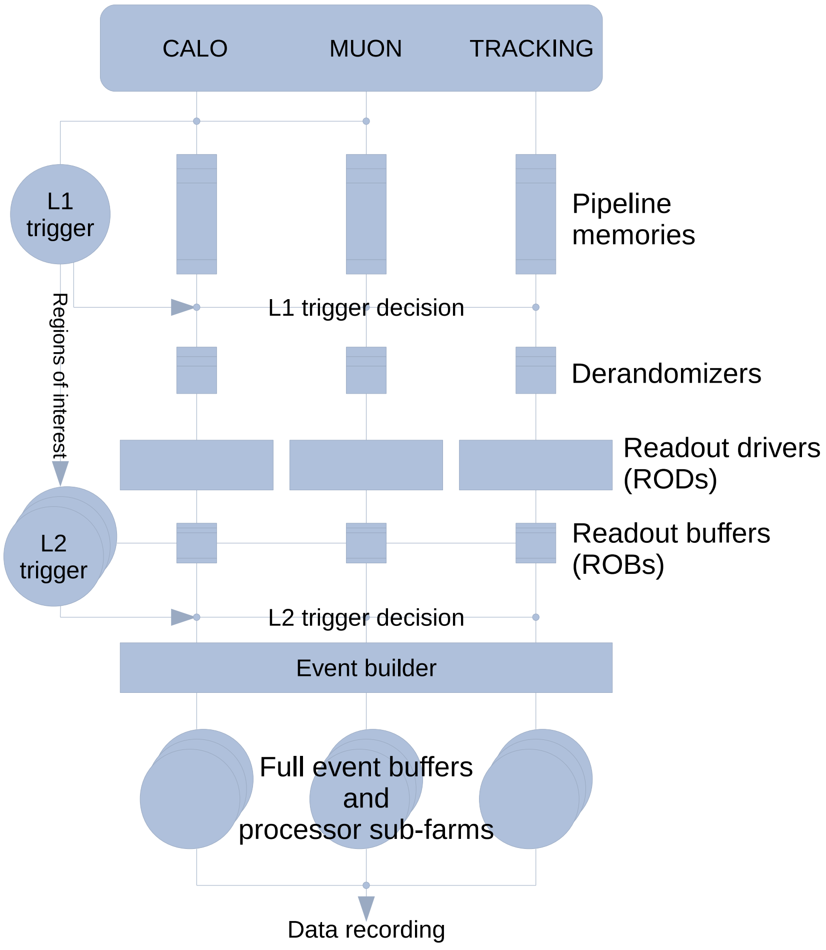

Figure 4.6: Diagram of the ATLAS trigger and readout system.

4.8 Online triggers and readout

The readout system of the ATLAS detector is closely connected with the online trigger system, which consists of two trigger layers (the so-called L1 trigger and L2 trigger), and one event filter [79]. The frequency at which LHC delivers bunch collisions is by design 40 MHz (every 25 ns), although throughout 2011 data taking it was 20 MHz (every 50 ns). It is physically impossible to reconstruct and record every of these 40 millions events per second. And what's more important, only a fraction of these events contain the hard scattering *pp* collision, so most of the events would be useless even if we managed to record them all. The gradual system of triggers makes an on-the-fly decision whether the event has an actual *pp* collision or not. The L1 trigger works on the frequency of LHC bunches crossing. This trigger is fully hardware, so it takes a decision in a matter of nanoseconds during the time while the signal from the detectors travels the cables to the readout drivers (RODs). The L1 triggers makes only the rough assumptions about the event. It calculates the rough amount of energy deposited in the parts of the calorimeters and muon chambers, and determines so-called "regions of interest" (ROIs), which are passed to the next level trigger, to get a closer look at. The next level trigger is called the L2 trigger and is software based. It provides the rate of events up to 60 KHz and makes its decision while the event is stored in a read-out buffer (ROB). Its output event rate is 5 KHz. The final stage is an event filter which outputs the events at the average rate of 400 Hz. At this rate the events are saved to the output streams. The L2 trigger and the event filter are also collectively called the High Level Trigger (HLT), since they study the event much deeper then the L1 trigger, and work on reconstructed event, rather then the deposited energy, which is what the L1 trigger do. The precision of the L1 trigger is 500 MeV and it only measures the total amount of the deposited E_{T} in the calorimeter towers (and consequently, the amount of missing E_{T}). The L2 trigger attempts a partial reconstruction of the event in ROIs which are passed down from the L1 trigger as well as track reconstruction, and the event filter does the full event reconstruction in these regions.

The full reconstruction of the filtered event is then done by the large on-site computer farm, and then stored by the use of the data acquisition system (DAQ).

CHAPTER 5

Data Samples

The data samples is the actual information about collisions recorded by the detector. This information is divided into periods, runs and luminosity blocks (LB). The luminosity block is the smallest of the three, its duration is decided by the ATLAS central trigger processor, and usually is one minute. The data taken within one LB is considered to have constant luminosity, which is calculated separately and stored in the luminosity database. To calculate the instantaneous luminosity, ATLAS uses several specialized detectors: the Minimum Bias Trigger Scintillators (MBTS), which determines the start of the bunch crossing, the Beam Conditions Monitor (BCM) which was originally designed to monitor the beam losses and prevent the inner detector damage, but the data from which can be used to calculate luminosity, and the LUCID detector (LUminosity measurement using a Cherenkov Integrating Detector), which is specially designed to measure luminosity by the use of the Cherenkov radiation. The data from BCM and LUCID is captured during the data-taking, and is later scaled to the luminosity and beam conditions values provided by the LHC [80]. The run represents the data taken during one continuous period of time. It can't be longer that one beam injection, but could be shorter, if some problems that lead to a halt in data taking were encountered during the injection. The period is a group of runs with the same detector conditions. Each period represents different setup of the detector and/or triggers and/or collider itself.

In 2011 there were 13 periods from A to M. Periods A and C were not physical runs, and the period B had only 16.98 pb^{-1} worth of data while having the conditions substantially different from all the other runs and thus was excluded from the analysis.

During some of the runs there were discovered problems with the detector or with the triggers, which compromised the data. The LBs during which these problems occur should be excluded from the analysis, and it is done using the good run list (GRL) which lists all the runs and LBs which should be used. In this analysis the common GRL of the WZ group (`data11_7TeV.periodAllYear_DetStatus-v36-pro10_CoolRunQuery-00-04-08_WZjets_allchannels_DtoM.xml`) is used.

The amount of data collected from the detector can be measured by its integrated luminosity. In Section 3 a definition of the instantaneous luminosity is given, which represents the amount of delivered data per unit of time. By integrating the instantaneous luminosity over data-taking time we can calculate the total amount of data delivered by LHC. When referring

Period	Run Range	Lumi [pb^{-1}]	Max Lumi [$\text{cm}^{-2}\text{s}^{-1}$]	Default SE trigger
D	179710-180481	178.816	6.65×10^{32}	EF_e20_medium
E	180614-180776	50.176	8.37×10^{32}	EF_e20_medium
F	182013-182519	152.187	1.11×10^{33}	EF_e20_medium
G	182726-183462	560.837	1.27×10^{33}	EF_e20_medium
H	183544-184169	278.271	1.27×10^{33}	EF_e20_medium
I	185353-186493	399.205	1.90×10^{33}	EF_e20_medium
J	186516-186755	232.931	2.02×10^{33}	EF_e20_medium
K	186873-187815	660.211	2.35×10^{33}	EF_e22_medium
L	188902-190343	1568.848	3.28×10^{33}	EF_e22vh_medium1
M	190503-191933	1121.768	3.61×10^{33}	EF_e22vh_medium1

Table 5.1: The list of 2011 ATLAS data periods used in the Z analysis.

the luminosity without indication of whether it is instantaneous or integrated, it usually mean that the integrated luminosity is implied. The data taking process is also not absolutely effective, there are losses from trigger failures, DAQ system overloads, and just errors that prevented data taking at some period of time. The process of translating of the recorded luminosity to the delivered luminosity is thus not trivial, but can be done automatically by the use of the special tool [1], so in all the calculations only the delivered luminosity is used.

The total luminosity for full data set used in the analysis was calculated by summing the luminosity from all LBs and equals to $4.58\,\text{fb}^{-1}$ with the systematic uncertainty 1.8% [80]. The timeline of data collection can be seen on Figure 5.1. The list of all periods with corresponding run numbers, integrated luminosity, maximum instantaneous luminosity and the default single electron trigger (which is the trigger used for the $Z \to ee$ central forward analysis) is shown in Tab. 5.1. The triggers for the analysis were chosen because they were the lowest unprescaled single electron triggers for the corresponding periods. The process of prescaling is done for the low-energy triggers, because we have no resources to record all the events that match these triggers, so we record only the known fraction of them, e.g. one out of three. For the analysis to remain unbiased, the use of the unprescaled trigger is important. The single-electron trigger was used because of the detector geometry and the trigger system set-up: the trigger is only working in the central part of the detector, so while the central-central analysis uses the di-electron trigger, because both of the electrons is expected to be in the central area, the central-forward analysis has to use the single-electron one.

---

[1] Can be found here `https://atlas-lumicalc.cern.ch/`

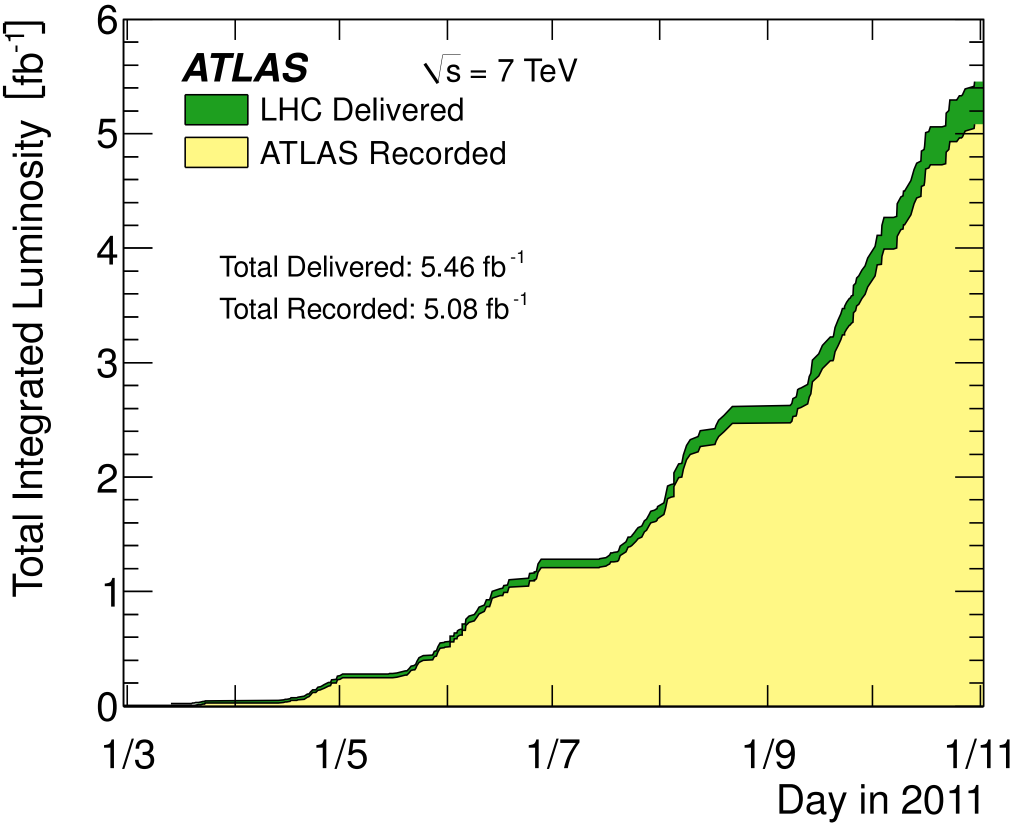

Figure 5.1: The integrated luminosity recorded by the ATLAS detector during 2011. [81]

CHAPTER 6

Monte Carlo (MC) Samples

In order to analyze the data we use the computer-generated so-called pseudo-data samples using the software that simulates the physical processes that happen in the detector. This pseudo-data is also called "Monte Carlo" or MC and its purpose is to construct the data samples based on the theoretical predictions of our physical model. Ideally, the MC samples should be as close to the experimental data as possible, allowing us to inspect all stages of the analysis with a great accuracy. MC is used for tuning of the reconstruction algorithms (see Section 8), calibration of the calorimeter (see Section 7), calculation of the efficiencies (see Section 12), estimation of the background (see Section 13), and finally for the comparison of the data to theoretical predictions (see Section 14). Unfortunately, we are unable to reproduce data samples precisely, so some corrections are made by means of reweightings (see Section 6.4).

The process of of MC samples generation consists of several stages, which can be seen in the diagram of the MC production chain in Figure 6.1. Here the short descriptions of every step of the production are given:

1. The simulation of *pp* collisions, which involves the production and the decay of high-energy particles (done by the MC generators, see Section 6.1).
2. The simulation of interactions between the high-energy particles and the detector material (done by the Geant4 software [82], see Section 6.2).
3. The simulation of the detector response based on the amount of deposited energy in different parts of the detectors (done by the ATLAS software).
4. The reconstruction process runs the same way as for the experimental data samples, it is fully described in Chapter 8.

The simulation process takes a lot of time, with the most time-consuming process being the simulation of the particles passage through the detector, or even more precise, through the EM-calorimeters, as the calorimeters consist of very dense materials (e.g. lead and liquid argon) and hence the incoming high-energy particles produce showers with the tens of thousands of lower-energy particles. There are several techniques used to speed up this process, but most of them produce results that are different from the standard not-optimized simulation, which

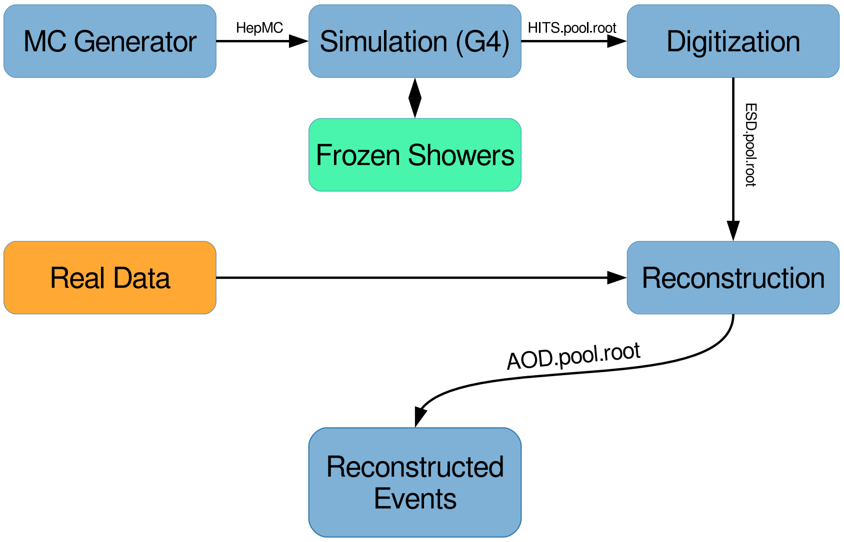

Figure 6.1: Diagram of the ATLAS MC production chain

makes them unusable for many types of analysis (including $Z \to ee$). The only technology which gives the result close enough to the standard simulation to be enabled for all analysis samples by default is the Frozen Showers, which will be fully described in Section 6.2.1. In the following sections the details of the steps involved in the MC production chain are discussed. In Section 6.1 the details of the various MC generators (first step) are given, and in Section 6.2 the rest of the production chain is discussed, with the focus on the simulation of the passage of the high-energy particles through the detector (second stage) and the digitization process (third stage). The reconstruction process is discussed fully in Section 8.

6.1 MC generators used in ATLAS experiment

The first stage of the MC production is the simulation of the pp collision itself. The simulation of this process is based on the Standard Model, and tries to account for every significant aspect of it. The core of the simulation is the calculation of the matrix element (ME) of the pp interaction, which can be done in different orders. The simplest case is the leading order (LO), which is the bare Drell-Yan diagram in case of the $Z \to ee$, with no loops or extra legs. The simulations in the leading order are not precise, and generally the next to leading order (NLO) or next to next to leading order (NNLO) are used instead, with one or two extra loops/legs respectively. The calculation of the matrix element at higher orders is very complex, and in order to increase the precision of the simulation the additional particles are simulated outside of the ME. Additional QCD particles are generated using the “parton shower” (PS) technique, which simulates the QCD radiation from each parton independently. The PS technique is widely adopted and used in many MC generators. Additional QED radiation is generated in a similar way by the independent package named “Photos” [83], with the similar technique. This package can be used in conjunction with other MC generators.

Here is the list of the MC generators used in ATLAS analyses:

- Herwig [84] is a general-purpose event generator for high-energy processes, with particular emphasis on the detailed simulation of QCD parton showers. The program provides a full simulation of hard lepton-lepton, lepton-hadron and hadron-hadron scattering and soft hadron-hadron collisions in a single package, and has the following special features:
  - Initial- and final-state QCD jet evolution with soft gluon interference taken into account via angular ordering.
  - Color coherence of (initial and final) partons in all hard subprocesses, including the production and decay of heavy quarks and supersymmetric particles.
  - Azimuthal correlations within and between jets due to gluon interference and polarization.
  - A cluster model for jet hadronization based on non-perturbative gluon splitting, and a similar cluster model for soft and underlying hadronic events.
  - A space-time picture of event development, from parton showers to hadronic decays, with an optional color rearrangement model based on space-time structure.

  In the current analysis Herwig was used to provide the parton showering for other generators.

- Pythia6 [85] (and an updated version Pythia8 [86]) is a generator with the goal to provide as accurate as possible a representation of event properties in a wide range of reactions, within and beyond the Standard Model, with emphasis on those where strong interactions play a role, directly or indirectly, and therefore multihadronic final states are produced. The physics is then not understood well enough to give an exact description, instead the program has to be based on a combination of analytical results and various QCD-based models.

- Powheg [87] is a hard scattering event generator for heavy quark production in hadronic collisions. It is accurate at the next-to-leading order in QCD, and it can be interfaced with shower Monte Carlo programs like Herwig and Pythia6, in such a way that both the leading logarithmic accuracy of the shower and the NLO accuracy of the ME are maintained in the output. This generator is the main MC generator used in 2011 analyses.

- Mc@Nlo [88] is a practical implementation, based upon the Fortran Herwig and Herwig++ event generators, of the Mc@Nlo formalism, which allows one to incorporate NLO QCD matrix elements consistently into a parton shower framework.

- Sherpa [89, 90] is a multi-purpose tool which contains a very flexible tree-level matrix-element generator for the calculation of hard scattering processes within the Standard Model and various new physics models. The emission of additional QCD partons off the initial and final states is described through a parton-shower model without the need of an additional generator. This generator is only for the signal MC only.

6.1.1 Signal MC

The part of Monte Carlo simulation which represents $Z \to ee$ events is called "signal MC". The signal MC is the main component of all the simulated MC. Its samples are used for the data unfolding (deconvolution), which is the process that aims to translate the number of reconstructed events into the true number of events in each bin. The unfolding procedure is described in Section 11. As well as Standard Model itself, the MC generators have parameters which can't be theoretically predicted, and should be found empirically. This process is called "MC tuning", and is done separately for every experiment, because the tune which will describe well one experiment won't fit for other. The tunes used in ATLAS are described in [91, 92].

The other important part of MC customization is the PDF set. The definition of the PDF can be seen in Section 2.2. The PDF sets used in the current analyses are CT10 NLO for the matrix element and CTEQ6L1 for the showering. They are decribed in [66, 93].

6.1.2 Background MC

The part of Monte Carlo simulation which represents different processes which can be misinterpreted as $Z \to ee$ is called "background MC". There are several background processes that can be simulated using MC, and most of them (all but one) are electroweak processes, that is why the background MC is also called an "electroweak background" as opposed to the "multi-jet background" (or "QCD background") which is the background from the multi-jet hadronic processes, which cannot be reliably simulated.

We use seven different types of backgrond MCs:

- $W \to e\nu$, the decay of a W boson into an electron and a neutrino. This process can be misinterpreted as Z decay if another electron is reconstructed in the same event, most notably, when a jet is misinterpreted as an electron (a "fake electron").
- $W \to \tau\nu$, the decay of a W boson into a τ-lepton and a neutrino. Can be misinterpreted if the τ-lepton decays into an electron, and another unrelated electron is reconstructed, as in the previous case.
- $Z \to \tau\tau$, the decay of Z boson into two τ-leptons. Can be misinterpreted if at least one tau decays into electron, and another electron is reconstructed. The case of both tau decaying into electrons and Z boson constructed from them is also possible, since the mass window is wide enough for that.
- $t\bar{t}$ events, which have lots of decay modes, and thus can be misinterpreted as almost anything, including $Z \to ee$. The most common case is $t\bar{t}$ decaying into $W^+W^-b\bar{b}$, and thus falling into the WW category.
- WW, can be misinterpreted if both bosons decay into $e\nu$.
- WZ, and ZZ events. Although such events contain genuine Z bosons, our analysis requires to exclude them. So the misinterpretation of either of them as a single Z event (by losing the extra electrons, or with a non-leptonic decays) is a background for us.

6.2 MC simulation process in ATLAS

Although the whole process of the production of the MC samples can be considered as "simulation", in this context "the simulation process" refers to the particular stage of the whole production chain: the simulation of the passage of the high-energy particles through the matter of the detector. It is done using the Geant4 software and the highly-accurate 3D model of the detector. The simulation in Geant4 is done as a discrete step-by-step process, with the length of the step being calculated dynamically for each particle, based on particle kinematics and the physical processes that happen to that particle. Because of that the simulation of the particles in vacuum takes much less time than in heavy matter. That is the reason why the majority of the simulation time is spent in calorimeters: they are built of the densest materials with the explicit purpose to stop as many particles as possible. The output of the simulation stage is "hits", the 4D vertexes of energy deposits in sensitive areas of the detectors.

The next stage is to simulate the work of the detector itself, or to convert the energy deposits into detector response, which are usually voltages in the read-out channels. This process is called "digitization", because its output are "digits" that are provided by the read-out channels. During this stage all features of the detector logic are simulated (e.g. electronic noises or channel-dependent variations). This is done by the internal ATLAS digitization software, and because it requires an ultimate knowledge of every particular sub-detector, parts of it are maintained by separate groups related to the respective sub-detectors.

The last step in the production chain is the reconstruction. It is the same for both MC and experimental data samples, as the digitization process aims to provide the same data as we get from the detector during production runs. During this step the responses from the detector are reconstructed into physical objects, which is done in two steps. In the first step the response from the trackers is reconstructed as tracks and the response from the calorimeters is reconstructed as clusters. During the second stage the tracks and clusters are combined into the physical particles. The second stage differs between several so-called "flavors" of the analysis, implementing various reconstruction algorithms for them. The flavors of this stage of reconstruction include e/gamma, jet/EtMiss/tau, b tagging, and muon. $Z \to ee$ analysis uses the first: e/gamma reconstruction. This process is done using the internal ATLAS reconstruction software. More on the reconstruction process with respect to the real data from the detector is described in Section 8.

The results of the reconstruction are stored in the special format called AOD (Analysis Data Object), which is also developed internally by ATLAS. AODs can be read by the ATLAS analysis framework, which gives easy access to all reconstructed objects.

6.2.1 Frozen Showers

The frozen showers system (FS) is designed to speed up the Geant4 simulation process inside the EM calorimeters. The main principle of FS is to substitute the low-energy particles with the EM-showers, which are pre-simulated and stored in the libraries (see Figure 6.2). These libraries must be generated in advance for each calorimeter and for each type of particles which

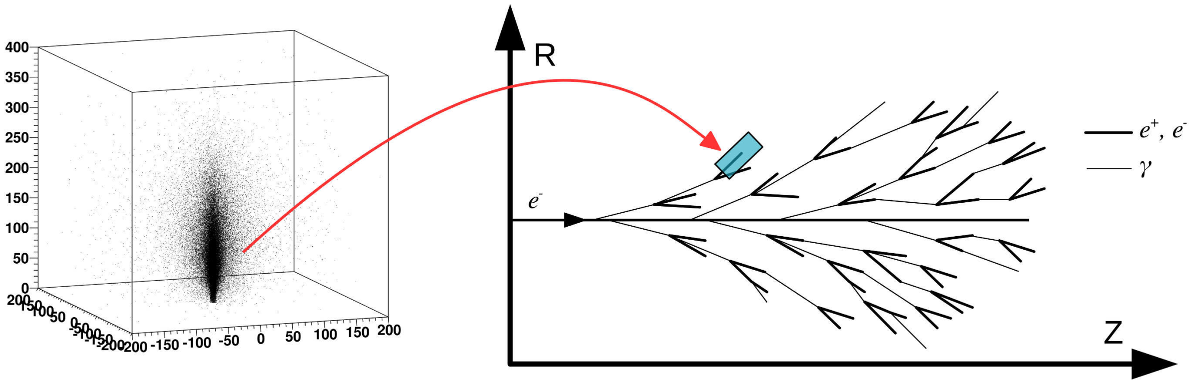

Figure 6.2: Diagram showing the shower substitution of the low-energy particle, during the high-energy particle simulation.

is needed to be fast-simulated during the production. The generation process consists mostly of the low-energy particles simulation and recording the information about every energy deposition this particle made. The array of these deposits or “hits” passes through several post-processing procedures in order to reduce its size, and becomes a “shower”.

The generation of the shower library is thus a preparatory procedure, which needs to be done every time when something is changed in the Geant4 simulation process. The examples are the change of the Geant4 package version, or the change in the detector geometry. Usually these changes applied between the MC campaigns, which means that the new set of libraries needs to be generated for each campaign. In order to improve results of FS-enabled simulation the libraries are then tuned: the shape and the energy response of the stored showers are slightly changed to provide the changes needed in the resulting simulation.

The processes of the library generation (and tuning) and the production use of the FS system would be described separately in the two following sections.

6.2.1.1 FS library generation

The library is the set of the showers simulated from the low-energy particles of the same type (electron, photon, etc.). The library should be able to provide the shower for any particle of this type within the determined energy bounds and inside the corresponding sub-detector. Thus, the showers populating the library should also be generated with all the possible energies and in all of the sub-detectors volume. To do this we need to generate the low-energy particles (as during the generation stage described in Section 6.1) with different energies and different vertexes that covers continuously both volume and energy range.

The easiest way to do it is to use a so-called “particles gun”: a tool that can create a particle of arbitrary type, momentum and vertex. This way we will get a library uniformly populated by particles in every part of its kinematic space. This approach has two major disadvantages. First, it reduces the quality of the simulation. As we can’t match all of the particle parameters while searching for the suitable shower within the library (it will take too much time and require the libraries of enormous sizes), we disregard some of them and introduce large bins on some others. Because of that the matched shower can have substantially different properties than the required particle. The second problem is the oversized library. During the production simulations the libraries corresponding to some part of the kinematic space (e.g. with the lowest energy of $0 - 10$ MeV as opposed to $500 - 1000$ MeV) are requested more often than others. This makes some showers overused and some other underused, making the results of the simulation worse and introducing the redundant memory footprint.

The better way to handle this is to generate the library using the processes similar to the usual MC production chain. It is called a two-staged library generation. The first stage is to conduct the normal simulation of the MC samples, but on much lesser scale: only hundreds of events are required. During the simulation, every time when a low-energy particle is requested to be fast-simulated using FS, the parameters of this low-energy particle are saved as a starting point for the shower. As the starting points tend to be clustered tightly around the track of the initial high-energy particle, only the fraction of the initial starting points is used for library generation in order to rarify them and get a more even coverage of the detector's volume. The sample coverage of all the EM calorimeters in ATLAS detector can be seen in Figure 6.3. It can be seen that most of the starting points are in the border regions of the calorimeters, while the central regions are considerably less occupied. It also can be seen that the starting point distribution depends on η more than on any other geometry variable, which justifies the choosing of it as the main geometry variable for the library binning. The second stage is the simulation itself. During this stage the starting points are taken one-by-one and simulated using the standard simulation infrastructure, producing the showers, which in turn go to the final library. The density distribution of the simulated hits within the shower can be seen in Figure 6.4. It can be seen the the shower is distributed mostly along the direction of the initial particle. It is important to note, that the scale of this plot in that direction is twice than that of the lateral directions, so in reality the shower is even more stretched along that line.

The library generated with the latter method contains the showers evenly distributed throughout the whole kinematic plane. The sample coverage can be seen in Figure 6.5. The distribution of the library density follows the natural occurrence of the showers during the production simulation, with lower-energy showers being more common than the higher-energy ones. The coarse η-binning ensures that the appropriate shower will be found for every particle in this kinematic region.

This way of library generation solves all the problems mentioned above. The bin population problem does not occur because we produce the showers based on the physical MC samples, and the resulting size of each kinematic bin is in direct dependence of the number of times this bin is used. This allows to reduce the size of the library and yet make a bigger diversity.

The post-processing stage consists of merging of the adjacent hits and of removing the far-standing hits that won't contribute to the reconstructed cluster anyway. Also, during this stage the size of the shower is calculated. It is used for containment check during the production (the check that the substitution shower is geometrically fully contained within the target detector volume). The post-processing parameters can be found in Table 6.1.

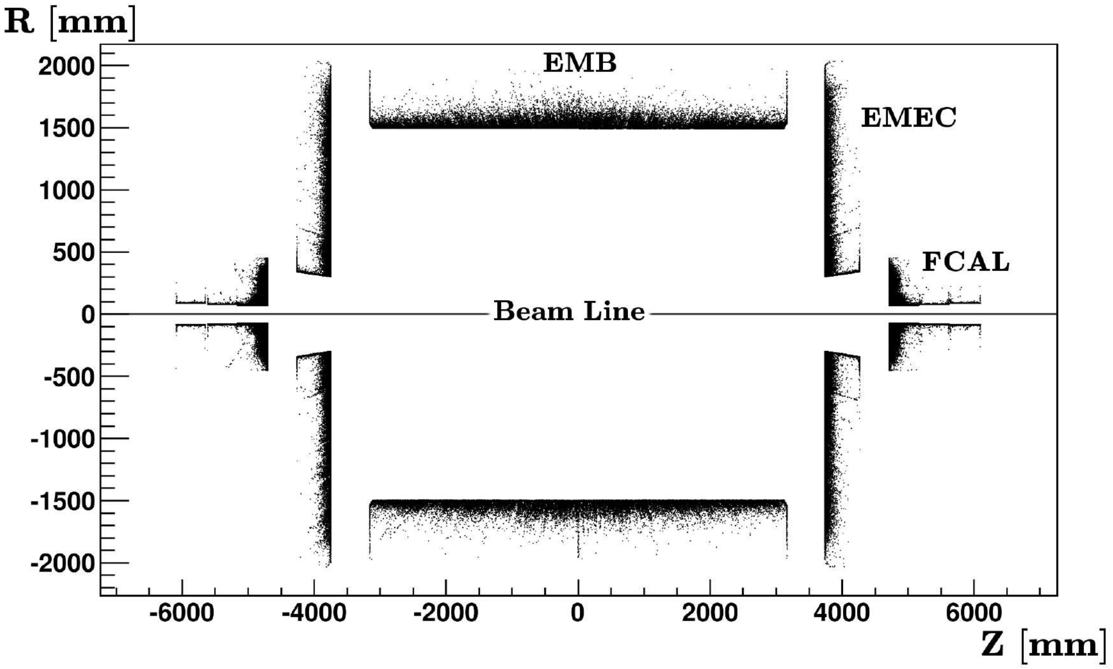

Figure 6.3: The first stage of the 2-staged library production: FS starting point generation. Every dot represents the starting point of a shower, the outlines of the different calorimeters can be easily seen.

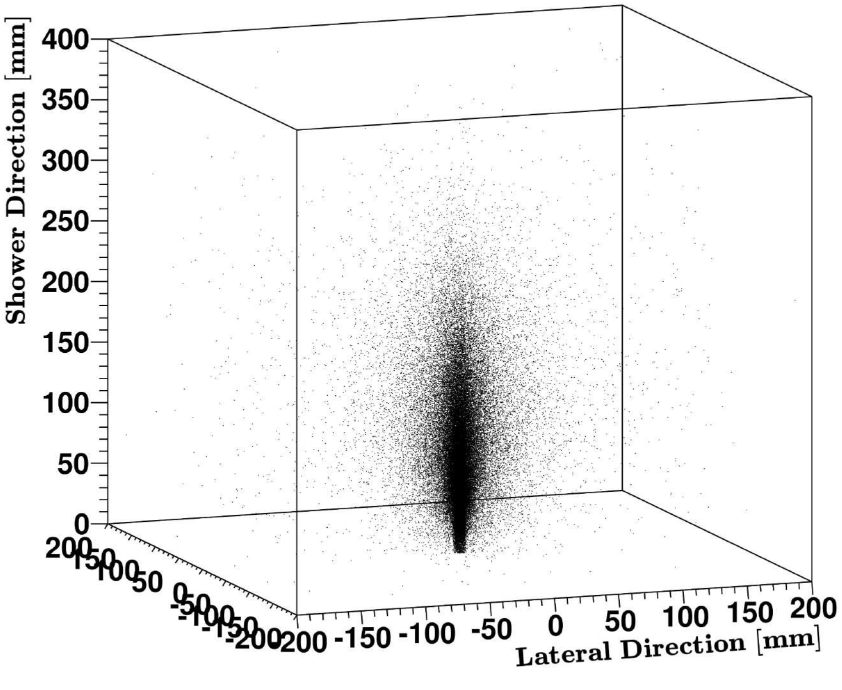

Figure 6.4: The second stage of the 2-staged library production: the simulation of the shower. Every dot represents the hit, which is the energy deposit within the active material of the calorimeter. The scale of shower direction is twice than that of the lateral spread.

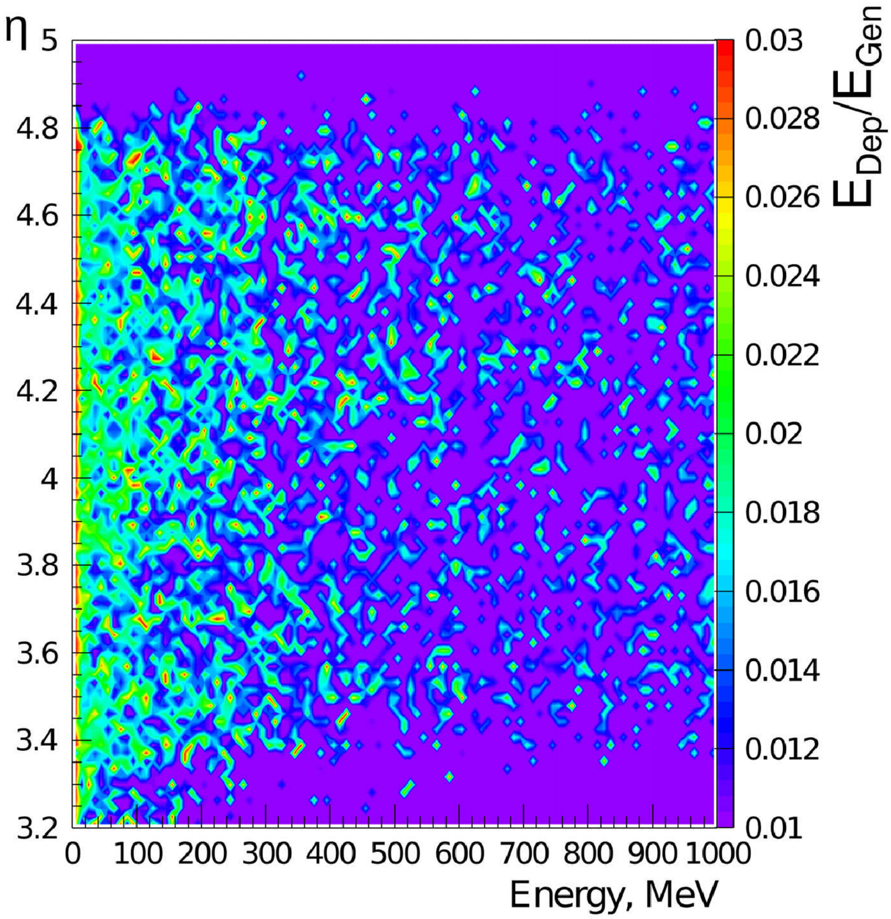

Figure 6.5: The diagram showing the population of the FCAL library for electrons over η-energy kinematic plane. The color scale shows not the density of the showers, but rather the energy responce, i.e. the amount of energy registered by the calorimeter versus the initial energy of the starting point. The density of the showers can be derived from the amount of the purple zero-level, which means "no showers present in this region". It can be seen that the average response of the calorimeter is about 2% and also that the lower-energy bins are much more populated than the higher-energy bins.

The general frozen showers parameters	
Detectors used	FCAL1, FCAL2, FCAL3
Type of the particle	photons, electrons, neutrons
Energy range	$E_\gamma < 10$ MeV, $E_e < 1000$ MeV, $T_n < 100$ MeV
Containment requirement	$\Delta E_{shower} > 98\%$
The library post-processing parameters	
Generation clustering cutoff	$(\Delta R_{cluster})^2 < 25$ mm
Generation truncation cutoff	$R^2_{hit} < 50000$ mm, $\Delta E_{shower} < 1\%$

Table 6.1: Main parameters used for the frozen shower libraries in FCAL

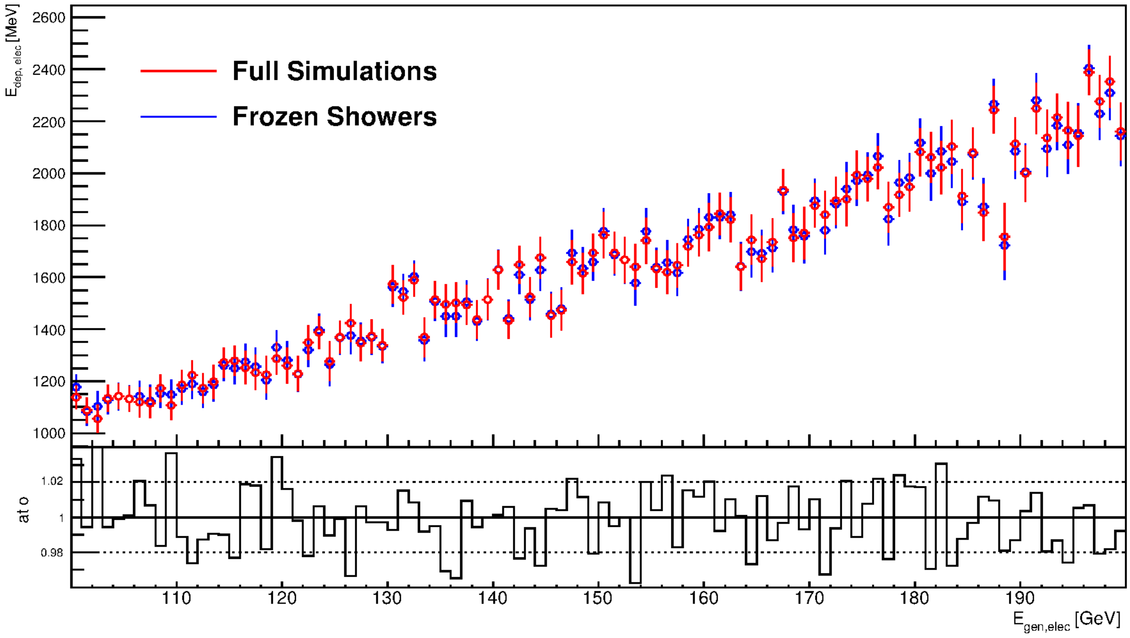

Figure 6.6: The comparison of the simulated detector response with Frozen Showers enabled and disabled (full simulation). This is the single electron event simulation in FCAL region at energies 100-200 GeV.

The tuning of the library can then be applied manually in order to make the results of the FS simulation closer to the standard simulation (also called "full simulation") or data. As this is a process that can't be (as of yet) done automatically, it requires lots of time and effort.

6.2.1.2 FS production use

During the production run the simulation software checks constantly if any particle agree with the fast-simulation criteria, which is the energy range (should be low enough) and the sub-detector containment (the particle should be far enough from the edges of the sub-detector volume for shower to fit within). The exact values of the aplicable ranges can be seen in Table 6.1. The containment check is energy-dependent, because the sizes of the showers grow with energy, and the more energetic particles should be further from the edges in order for shower to fit.

When the particle with the proper parameters is found, it is then removed from the simulation and replaced with the shower. Before the deposition, the shower is scaled to fully correspond to the particle in energy.

For the MC11c and MC11d campaigns, the data from which is used in this analysis, frozen showers system was enabled by default in FCAL. Several studies showed that the differences introduced by the FS is negligible compared to the differences between MC and data, while the simulation speedup was about 25%. The smallness of the errors introduced by the FS compared to other fast simulation methods (most notably - FastCaloSim) led to the misunderstanding, when the simulation with the FS system enabled was called "full simulation" as opposed to

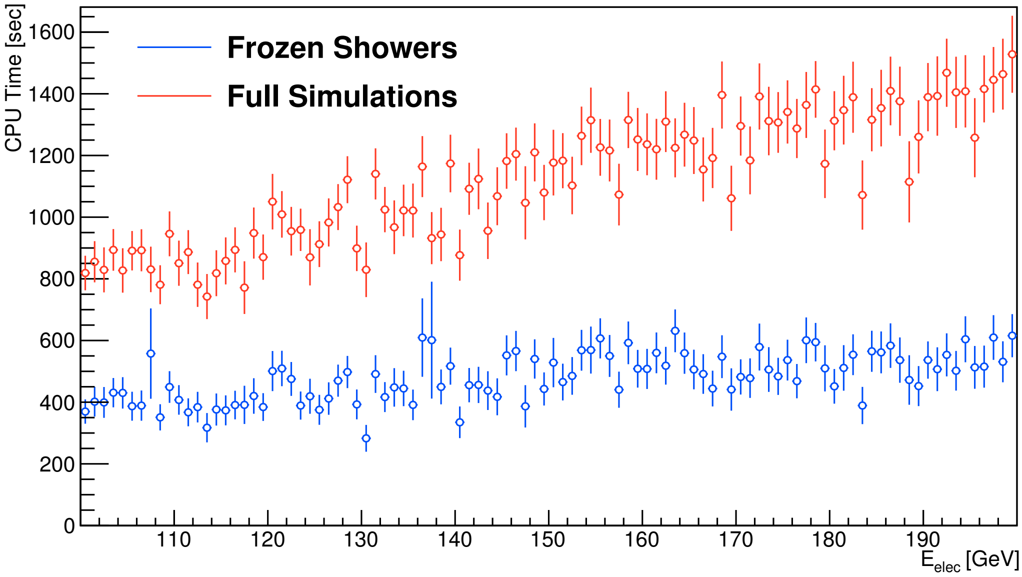

Figure 6.7: The simulation speed-up for single electrons events in FCAL region with energies 100-200 GeV.

other, less precise but faster methods, which were called “fast simulation”. In this terminology, all of the MC samples used in this analysis are full simulations. But in this chapter, the “full simulation” always means “with the frozen showers disabled”.

The sample comparison of the default, non-accelerated MC samples with the samples with enabled frozen showers can be seen in Figure 6.6. It can be seen that the difference between frozen showers enabled and disabled (full simulation) is about 2%, which is well within the statistical uncertainty. The simulation speed-up can be seen in Figure 6.7. It can be seen that the CPU time for FS-enabled simulation is almost independent of the electron energy, and is two to three times quicker than the full simulation. On higher energies the speed-up is even more significant, and FCAL region is the one region with the highest number of the high-energy particles.

Apart from the energy scale, another important feature of the simulated electrons is the shower shape variables which are used for electron identification. It is especially important for forward electrons, since with absence of the tracker information the shapes are the only discriminatory variables that help to identify the electrons (see Section 8.2 for details). The full list of the shower shape variables can be found in Tab. 8.1 in Section 8.2. The comparison of the shower shape variables can be seen in Figures 6.8 to 6.13. All plots are shown in arbitrary scale with the two plots containing the same number of electrons.

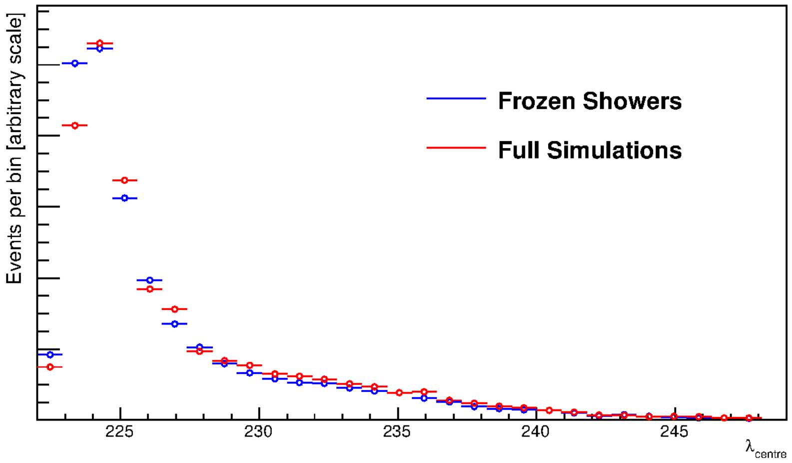

Figure 6.8: The shower depth variable. The distance of the shower barycenter from the calorimeter front face measured along the shower axis. Single electron events in FCAL region at 500 GeV. The scale is arbitrary.

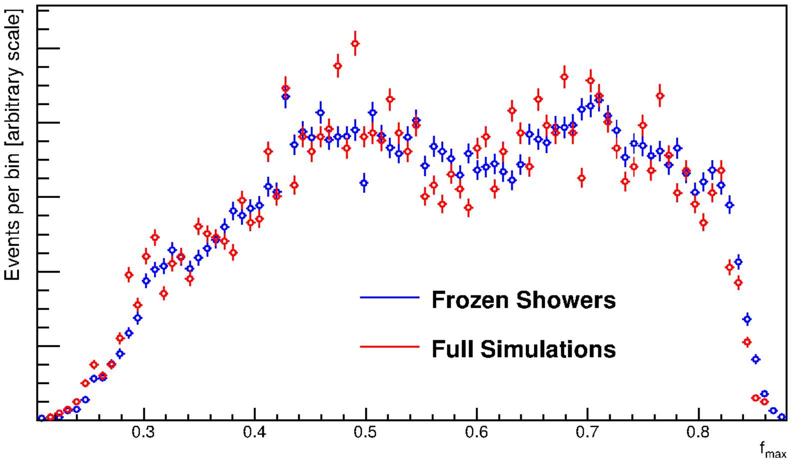

Figure 6.9: Maximum cell energy variable. Fraction of the cluster energy in the most energetic cell. Single electron events in FCAL region at 500 GeV. The scale is arbitrary.

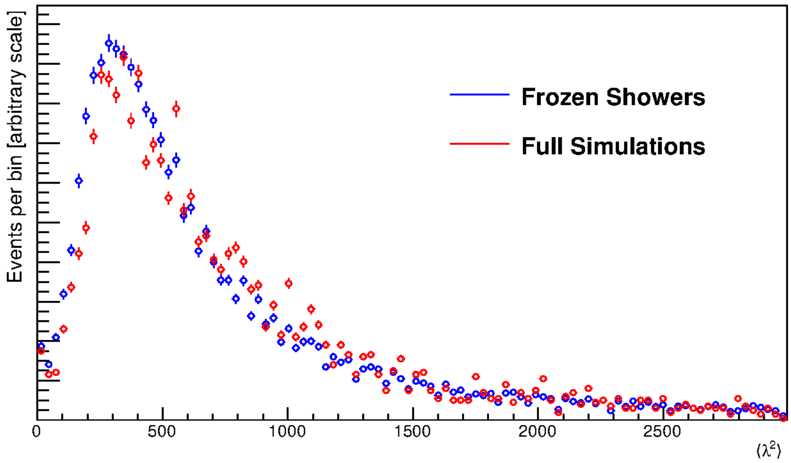

Figure 6.10: Longitudinal second momentum. Second momentum of the distance of each cell to the shower center in the longitudinal direction (λ_i). Single electron events in FCAL region at 500 GeV. Single electron events in FCAL region at 500 GeV. The scale is arbitrary.

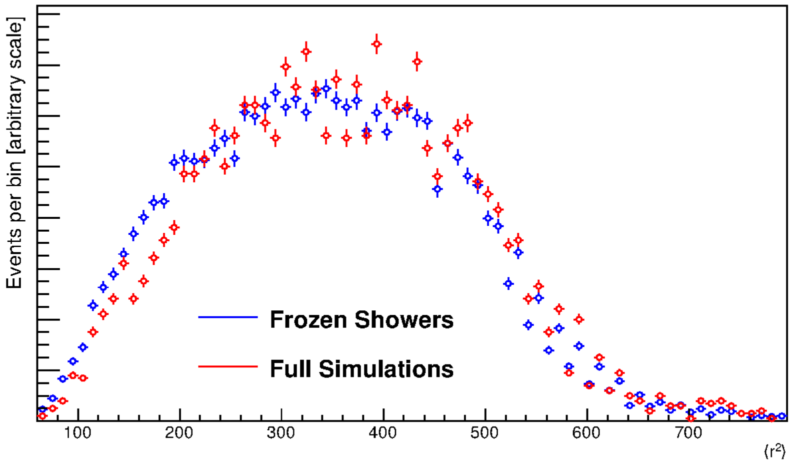

Figure 6.11: Transverse second momentum. Second momentum of the distance of each cell to the shower center in the transverse direction (r_i). Single electron events in FCAL region at 500 GeV. The scale is arbitrary.

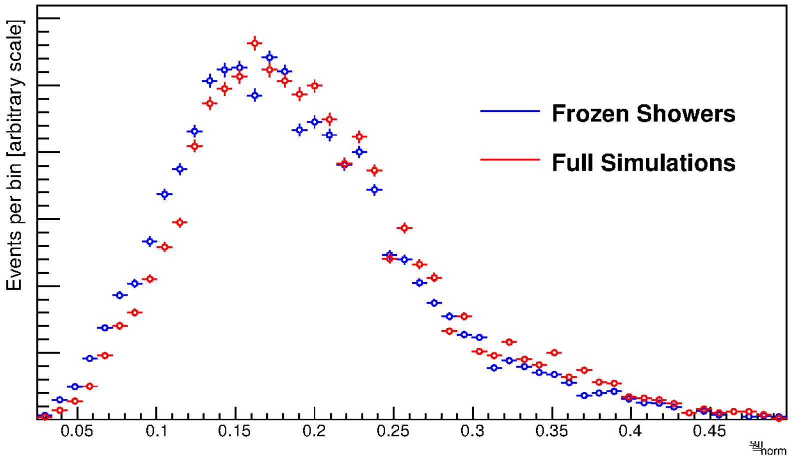

Figure 6.12: Normalized lateral momentum. $w_{\mathrm{norm}} = \frac{w_2}{w_2+w_{\mathrm{max}}}$ where w_2 and w_{max} are second momenta of r_i for different weights per cell. Single electron events in FCAL region at 500 GeV. The scale is arbitrary.

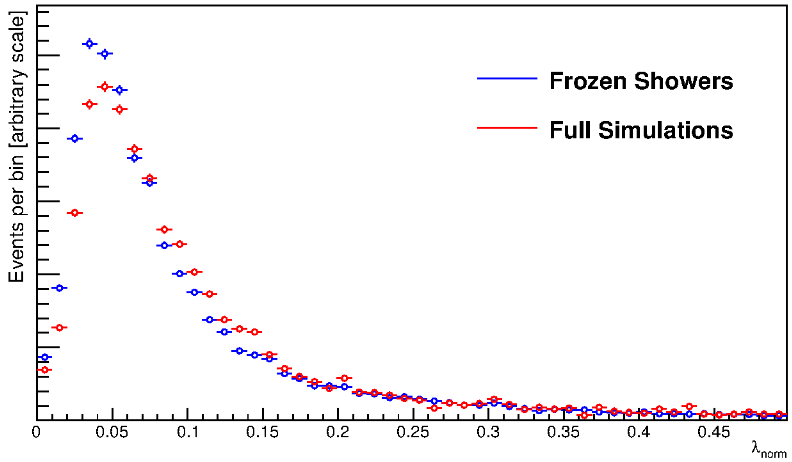

Figure 6.13: Normalized longitudinal momentum. $\lambda_{\mathrm{norm}} = \frac{\lambda_2}{\lambda_2+\lambda_{\mathrm{max}}}$ where λ_2 and λ_{max} are second momenta of λ_i for different weights per cell. Single electron events in FCAL region at 500 GeV. The scale is arbitrary.

Data set	Generator	σ·BR·ϵ_{filter} [nb]	N_{evt} [10^6]
108303^{d}	PowhegPythia6	1.006 (5%)	20
126006	PowhegHerwig	1.006 (5%)	10
106087 & 129913	Mc@Nlo	0.990 (5%)	5+5
147770	Sherpa	1.070 (5%)	10

Table 6.2: Signal Monte Carlo samples. The sample marked with ^{d} was taken from the MC11d campaign, the others are from the MC11c. The third column represents the filter ratio for the sample, and shows how much raw data corresponds to an event in this sample. The number in brackets is the theoretically predicted uncertainty. The fourth column shows the number of events in the sample.

6.3 MC samples used in analysis

During this analysis the MC samples from both MC11c and MC11d campaigns were used. The "d" is chronologically the fourth sample produced for the 2011 data, and the "c" is the third. The decision to make new samples is usually made when some errors in GEANT software or in ATLAS geometry are discovered. The latest "d" sample fixes all such known errors, which affected the electron performance in various cases. The "d" is thus used in cases where the electron performance is important. The main generator used for both signal and background was Powheg with the parton showering provided by Pythia6. The cross-check was done by the same Powheg with the PS done by Herwig and by Mc@Nlo also with the Herwig-provided showers. For the Mc@Nlo and Powheg matrix element calculations the CT10 NLO PDF set is used, while showering was performed with CTEQ6L1PDF. The list of MC signal periods that was used can be found in Tab. 6.2, the periods for MC background events are in Tab. 6.3.

6.4 Reweightings

The MC samples have a number of known shortcomings, and some data distributions are not described well. To fix this the reconstruction level reweightings based on MC/data samples comparisons, different MC generators comparison on the generation (truth) level, or using the other ATLAS analyses are applied. The weights are applied based on the truth information and are validated using the closure tests. The list of corrections is this:

- **Vertex Spread in z-direction Reweighting** is based on the z component of the vertex and aims to decrease the spread of the beam spot in z-direction of MC, which is significantly smaller in data (for data $\sigma_z \approx 56$mm, while for narrow beam spot MC sample $\sigma_z = 75$mm and for wide beam spot $\sigma_z = 90$mm). The `VertexPositionReweightTool` is used for that. The effect of this correction can be seen in Figure 6.14.

Process	Data set	Generator	σ·BR·ϵ_{filter} [nb]	N_{evt} [10^6]
$W^+ \to e^+\nu$	108297$^{\mathrm{d}}$	PowhegPythia6	6.160 (5%)	23
$W^- \to e^-\bar{\nu}$	108300$^{\mathrm{d}}$	PowhegPythia6	4.300 (5%)	17
$W^+ \to e^+\nu$	113186	PowhegHerwig	6.160 (5%)	16
$W^- \to e^-\bar{\nu}$	113184	PowhegHerwig	4.300 (5%)	12
$W^+ \to e^+\nu$	106080	Mc@Nlo	6.160 (5%)	16
$W^- \to e^-\bar{\nu}$	106081	Mc@Nlo	4.300 (5%)	12
$W \to \tau\nu$ Np0	107700	AlpgenHerwig	8.285 (5%)	3.4
$W \to \tau\nu$ Np1	107701	AlpgenHerwig	1.560 (5%)	2.5
$W \to \tau\nu$ Np2	107702	AlpgenHerwig	0.452 (5%)	3.8
$W \to \tau\nu$ Np3	107703	AlpgenHerwig	0.122 (5%)	1
$W \to \tau\nu$ Np4	107704	AlpgenHerwig	0.0307 (5%)	0.25
$W \to \tau\nu$ Np5	107705	AlpgenHerwig	0.00835 (5%)	0.07
$W \to \tau\nu$	107054	Pythia6	10.460 (5%)	1
$W^+ \to e^+\nu$	147412$^{\mathrm{d}}$	PowhegPythia8	$6.160 \cdot 0.1510$ (5%)	15
$W^- \to e^-\bar{\nu}$	147415$^{\mathrm{d}}$	PowhegPythia8	$4.300 \cdot 0.1404$ (5%)	10
$Z \to \tau\tau$ Np0	107670	AlpgenHerwig	0.834 (5%)	6.6
$Z \to \tau\tau$ Np1	107671	AlpgenHerwig	0.168 (5%)	1.3
$Z \to \tau\tau$ Np2	107672	AlpgenHerwig	0.0508 (5%)	0.81
$Z \to \tau\tau$ Np3	107673	AlpgenHerwig	0.0140 (5%)	0.22
$Z \to \tau\tau$ Np4	107674	AlpgenHerwig	0.00355 (5%)	0.06
$Z \to \tau\tau$ Np5	107675	AlpgenHerwig	0.00093 (5%)	0.02
$Z \to \tau\tau$	106052	Pythia6	0.990 (5%)	3
$Z \to \tau\tau$	147418$^{\mathrm{d}}$	PowhegPythia8	$0.990 \cdot 0.263$ (5%)	6
$\gamma\gamma \to ee$	129652	Pythia8	$2.41 \cdot 10^{-3} \cdot 0.7$ (40%)	0.5
$t\bar{t}$	105200$^{\mathrm{d}}$	Mc@Nlo	0.1773 (6.2%) · 0.555	1.5
WW	105985$^{\mathrm{d}}$	Herwig	$44.9 \cdot 0.389 \cdot 10^{-3}$ (7%)	1.5
WZ	105987$^{\mathrm{d}}$	Herwig	$18.5 \cdot 0.310 \cdot 10^{-3}$ (7%)	1
ZZ	105986$^{\mathrm{d}}$	Herwig	$6.02 \cdot 0.212 \cdot 10^{-3}$ (7%)	0.25

Table 6.3: Background Monte Carlo samples. The samples marked with $^{\mathrm{d}}$ were taken from the MC11d campaign, the others are from the MC11c. The third column represents the filter ratio for the sample, and shows how much raw data corresponds to an event in this sample. The number in brackets is the theoretically predicted uncertainty. The fourth column shows the number of events in the sample.

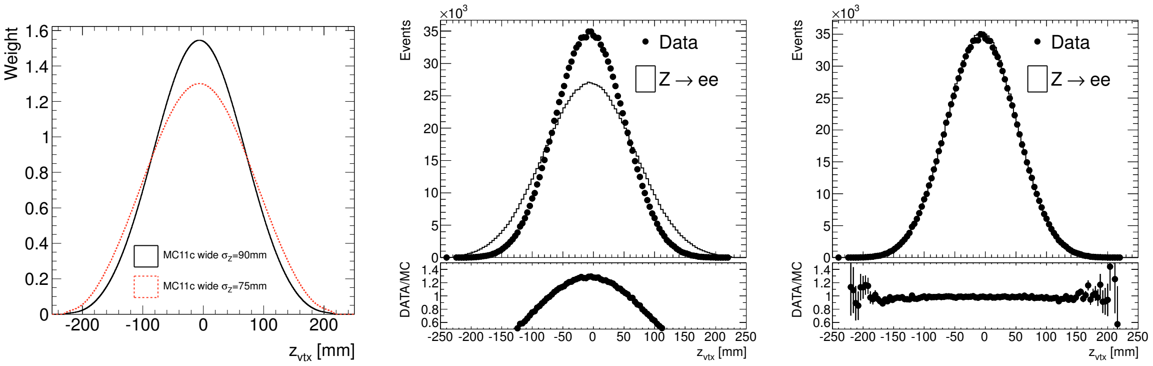

(a) z_{vtx} weights (b) Before z_{vtx} reweight (c) After z_{vtx} reweight

Figure 6.14: The effect of the vertex spread correction applied to MC11c samples. The corrections for MC11d remained the same.

- **Pileup reweighting** is based on the pileup conditions used during the MC generation, which were found not to be the same as the conditions during the real data taking throughout 2011. The comparison of the cumulative pileup conditions from various MC and data periods is shown in Figure 6.15.

- Z **Boson** p_{T} **Reweighting** is based on the p_{T} distribution of the Z bosons, which doesn't describe data well by the MC signal generators used for this analysis. The results from ATLAS Z ϕ^* and p_{T} analyses [94] were used for it, and it was done using the `BosonPtReweightingTool`. The differences between various MC generators in describing the Z boson p_{T} distribution is shown in Figure 6.16.

- Z **Boson Line Shape Reweighting** is the reweightings aimed to fix the fundamental shortcomings of the MC generators caused by the electroweak order not being high enough. This reweighting is done using the `LineShapeTool`. See [95] for details. The effect of the reweighting can be seen in Figure 6.17.

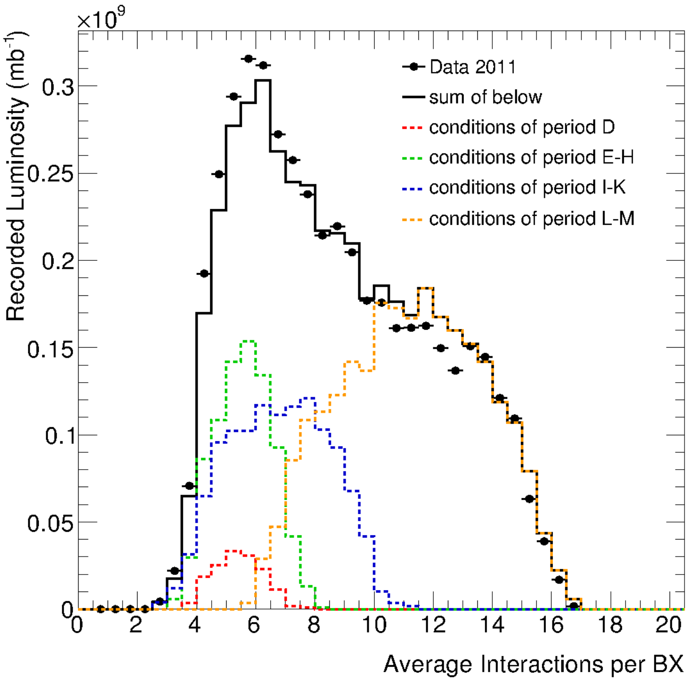

Figure 6.15: The comparison of the pileup conditions of the MC11c and 2011 data. The pileup conditions for different MC periods is also shown.

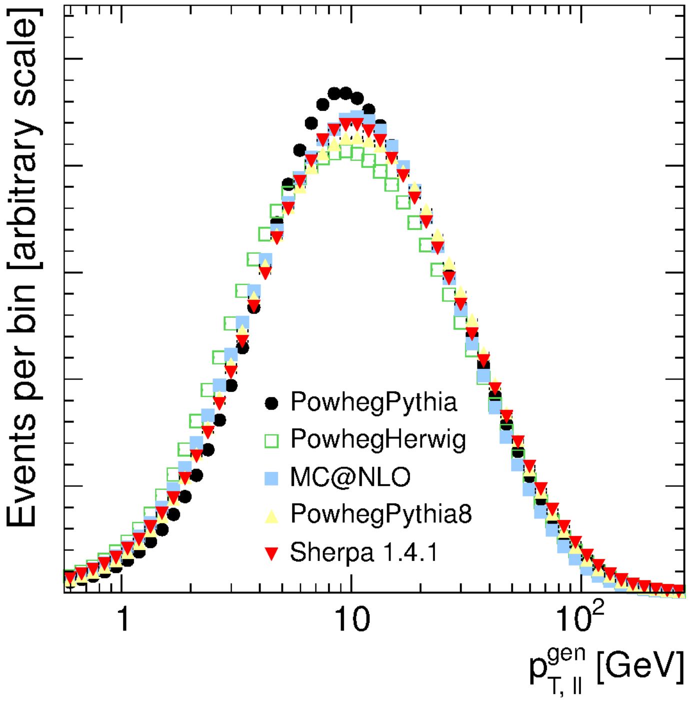

Figure 6.16: The comparison of the shapes of Z boson p_{T} distribution for various MC generators. Distributions are normalized to arbitrary scale.

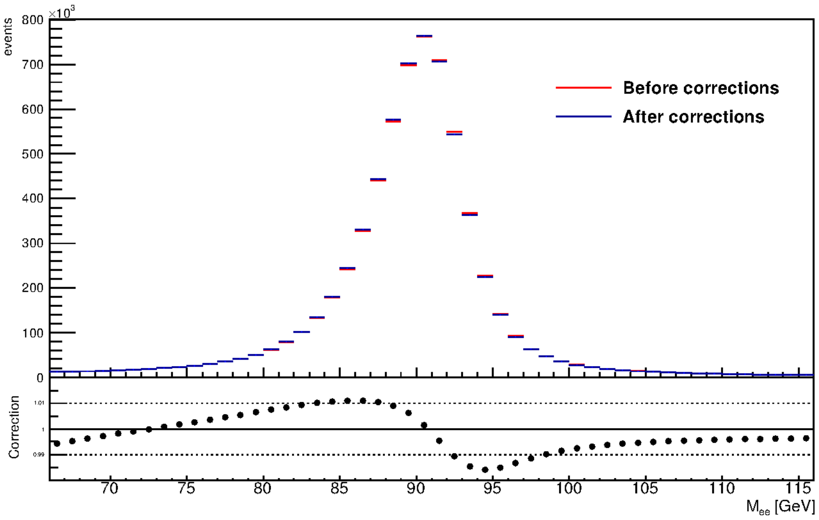

Figure 6.17: The effect of the LineShape reweighting in the Z boson peak mass distribution.

CHAPTER 7

Calibration of the EM calorimeter

EM calorimeter registers only about 1.5% of the total energy that the particle deposits in that calorimeter. There are several reasons for that: some energy is deposited in the presampler (i.e. outside of the calorimeter), some energy is deposited away from the main cluster and is not caught by the clustering algorithms, but most importantly, there is the energy that is deposited in the so-called dead material. Both the accordion-shaped central calorimeter and the tube structured forward calorimeter have most of its mass composed of the non-sensitive materials. Because of this design, the calorimeters must be calibrated in order to reconstruct the true energy of the particles. Here the process of the calibration of the EM calorimeters will be described. The process consists of the χ^2 minimization of the theoretically predicted, reconstructed energy and the truth (initial) energy of the MC sample. The MC sample is simulated using Geant4, the deposited energy is calculated based on the precise geometry model of the detector, the energy of the initial particles is then reconstructed using the theoretical model with several free parameters, and the parameters are then locked with the use of the approximation method.

7.1 Theoretical overview

The theoretically predicted formula for reconstruction of the energy is as follows

$$\begin{aligned} E_{e/\gamma} = {} & \underbrace{a(E_{tot}^{acc}, |\eta|) + b(E_{tot}^{acc}, |\eta|) \cdot E_{ps}^{clLAr} + c(E_{tot}^{acc}, |\eta|) \cdot (E_{ps}^{clLAr})^2}_{\text{energy in front}} \\ & + \underbrace{\frac{s_{cl}^{Acc}(X, \eta)}{f_{out}(X, |\eta|)} \cdot \left(\sum_{i=1,3} E_i^{clLAr} \right)}_{\text{energy in accordion}} \cdot \underbrace{(1 + f_{leak}(X, |\eta|))}_{\text{longitudal leakage}} \cdot F(|\eta|, \varphi) , \end{aligned} \tag{7.1}$$

where

- $a(E_{tot}^{acc}, |\eta|)$, $b(E_{tot}^{acc}, |\eta|)$ and $c(E_{tot}^{acc}, |\eta|)$ are the parameters that are used to correct the reconstructed energy based on the total energy deposited in the accordion structure (E_{tot}^{acc}) and η. The first two parameters are commonly called offset and slope. The third parameter was assumed to be negligible ($c = 0$).

- X is the longitudinal barycenter of the EM shower, thus representing shower depth. It is calculated as
$$X = \frac{\sum\limits_{i=0}^{3} E_i^{clLAr} \cdot X_i}{\sum\limits_{i=0}^{3} E_i^{clLAr}}, \tag{7.2}$$
where E_i^{clLAr} is the amount of energy deposited in the vsrious compartments of the calorimeter: presampler in case $i = 0$ and strip, middle and back for the subsequent i values respectively, and X_i is the depth, expressed in radiation length, of the longitudinal center of each compartment computed from the center of the ATLAS detector. The parameters E_i^{clLAr} are also used in eq. 7.1 directly.

- E_{ps}^{clLAr} is the part of the cluster energy measured in the presampler and corrected for the energy deposited in the passive materials.

- $s_{cl}^{Acc}(X, \eta)$ is a correction factor to the Accordion sampling fraction in the cluster.

- $f_{out}(X, |\eta|)$ is the correction for the lateral leakage of the shower, i.e. the energy deposited in the calorimeter outside the cluster.

- $f_{leak}(X, |\eta|)$ is the correction for the longitudal leakage of the shower.

- $F(|\eta|, \varphi)$ is the correction for the expected performance of the ATLAS detector, as described in [96].

As there is no presampler in the region of the outer wheel of the EMEC, as well as the forward region of the detector (can be effectively summarized as $|\eta| > 1.8$), the E_{ps}^{clLAr} parameter is parameterized there as the function of the barycenter (see eq. 7.2) and the fractions of the energy deposited in every compartment of the calorimeter.

The coefficients of this equation were optimized with several MC samples with different fixed energies ranged from 5 GeV to 1 TeV.

The reconstruction of the converted and unconverted photons is done using the same technique as for the electrons, with the coefficients approximation being done separately.

7.2 Calibration procedures

In order to reconstruct the energy of the EM-particles, several procedures are conducted, the overview of which can be seen in Figure 7.1. The steps are as follows:

1. The EM cluster properties, including its longitudinal development, and additional information from the ATLAS inner tracking system, are calibrated to the original electron and photon energy in simulated MC samples. The calibration constants are determined using a multivariate algorithm (MVA), with its optimization being performed separately

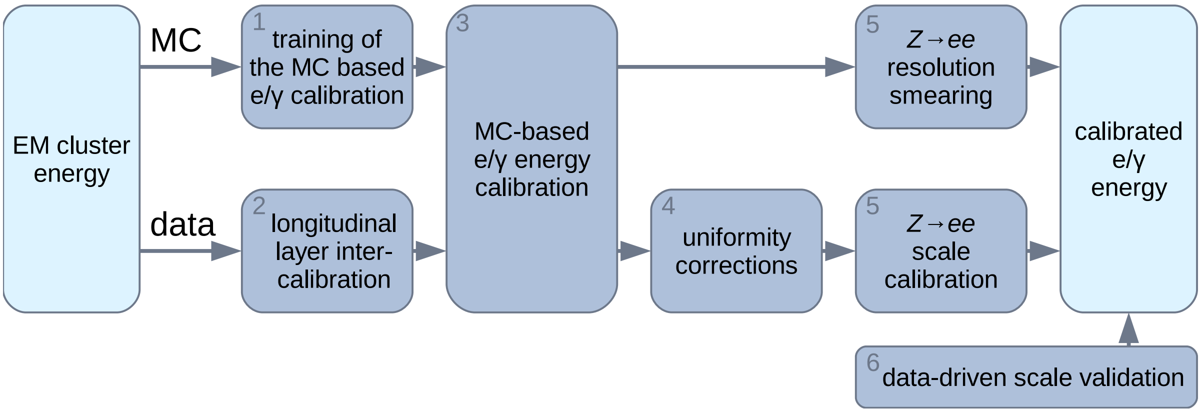

Figure 7.1: Schematic overview of the stages of the calibration procedures for the electrons and photons in ATLAS.

for electrons and converted and unconverted photons. For this calibration to work properly, the geometry of the detector must be described as precise as possible, so that the interactions of the particles with the detector material were accurate. The material distribution is measured in data using the ratio of the energy in the first-layer to the energy in the second-layer in the longitudinally segmented EM calorimeter. Measuring this ratio in data with different samples (electrons and unconverted photons) allows for a precise determination of the amount of material in front of the calorimeter and provides some sensitivity to its radial distribution.

2. Since the EM calorimeter is longitudinally segmented, the step is taken to equalize the scales of the different longitudinal layers in data with respect to simulation, prior to the determination of the overall energy scale, in order to ensure the correct extrapolation of the response in the full p_{T} range used in the various analyses.

3. The e/γ response calibration based on MC simulation is applied to the cluster energies recorded both from collision data and MC samples.

4. A set of corrections are implemented to account for response variations not included in the simulation in specific detector regions, e.g. non-optimal high-voltage regions, geometric effects such as the intermodule widening or biases associated with the LAr calorimeter electronic calibration.

5. The overall electron response in data is calibrated so that it agrees with the expectation from simulation, using a large sample of $Z \to ee$ events. Per-electron scale factors are extracted and applied to electron and photon candidates in data. The studies of the $Z \to ee$ samples showed that the resolution in data is slightly worse than that in simulation, and appropriate corrections are derived and applied to simulation to match the data.

6. The calibrated electron energy scale is validated with electron candidates from $J/\psi \to ee$ events in data. The resulting scale is dependent on η and p_{T}. The scale factors extracted from $Z \to ee$ events are assumed to be valid also for photons, with the photon-specific systematic uncertainties, which is validated with photon candidates from $Z \to ll\gamma$ events from the collision data.

The detailed description of the calibration process can be found in [97].

7.3 Forward calorimeter calibration

Because of the high non-uniformity of the forward calorimeter, the special approach to its calibration was needed. The determination of the entry point of the particle becomes an important task, because the calorimeter response depends very much on the distance between this point and the closest LAr-filled gap (the sensitive material of the FCAL). The absence of the tracker in the forward region makes this task no easier. Each readout channel in FCAL contains four adjacent LAr-filled gaps, and the entry point is calculated as a weighted average of the centers of the readout channels. The calibration error is mostly caused by the low precision of the entry point determination. The exact details of the procedure can be read in [98].

7.4 Fast simulation impact

Since both the MC11c and MC11d samples used in this analysis incorporate the results of the frozen showers fast simulation, the studies of the scaling of the calibration results were conducted [99]. The measurements were done on the central-forward $Z \to ee$ events in the peak mass window. The results of the comparison between samples with enabled and disabled frozen showers fast simulation system showed a difference in $\sim 1\%$, which was then stored as a calibration correction for future use in the analysis.

CHAPTER 8

Event Reconstruction

The reconstruction is the last stage of the data preparation and is the same for both genuine detector data and MC samples. The reconstruction process aims to interpret the output of the detector and to guess which particle could cause such response. Different analyses requires different focus on different types of particles, and because of that there are many reconstruction algorithms which make emphasis on different aspects of particles behavior. There are also several groups in ATLAS each of them is working on the algorithms for certain type of particles. For $Z \to ee$ analysis the electrons are used, and the group studying the details of the electron and photon reconstruction is called "e/gamma". The group suggested several algorithms for the reconstruction of both electrons and photons. The photons are not very important for $Z \to ee$ analysis (although the study of the photons can improve the background estimation for the $Z \to ee$ process, for this analysis it was not done), whereas the algorithms for electrons will be highlighted in this chapter. In section 8.1 the reconstruction algorithms itself will be described, while in sections 8.2 and 8.3 there will be descriptions of methods to increase the quality of the reconstruction.

8.1 Electron reconstruction

There are several algorithms that are used to reconstruct the EM-particles (electrons and photons), each of them reconstructs its own set of particles for every event. To distinguish which particle was reconstructed by what algorithm, the "author" field was introduced. The field consists of 5 bits each of them can be 1 or 0 depending on whether the corresponding algorithm reconstructed that particular particle (one particle can be reconstructed by more than one algorithm). The list of algorithms is as follows:

- **AuthorElectron** Electron reconstructed by standard cluster-based algorithm. It requires both EM cluster and a matching track.
- **AuthorSofte** Electron reconstructed by the track-based algorithm. This algorithm doesn't require EM cluster, only the track. This author can overlap with the previous.

- **AuthorPhoton** Photon reconstructed by standard cluster-based algorithm. This is the only method available for photons.
- **AuthorFwd** Electron reconstructed by the Forward cluster-based algorithm. As the inner detector doesn't provide tracks for $\eta > 2.5$, the algorithm for forward particles uses only the cluster, and is tuned to be used in the forward detectors.
- **AuthorRConv** Photon that is duplicated with electron. This author is used to mark the special cases when both electron and photon reconstruction algorithms return positive for the same particle.
- **AuthorTrigElectron** and **AuthorTrigPhoton** Mark the trigger particles. The triggers were discussed in Sec. 4.8.

Because of the much difference between the algorithms for central and forward electrons, the reconstruction process for both will be discussed separately.

8.1.1 Central

The central electron is the electron with $|\eta| < 2.5$. In this area of the detector both EM calorimeter and tracker are present, so the reconstruction algorithms can make use of both. In the central region there are two EM calorimeters: EMB and the outer ring of the EMEC, and the standard cluster-based algorithm behave slightly different in them. In the current analysis only the central electrons reconstructed by the standard algorithm were used. This algorithm consists of three main stages [100]: the initial search for an EM-cluster, the track matching and the final reconstruction of the electron candidate. For the initial search the sliding-window algorithm is used with the size of 3×5 cells in units of $0.025\eta \times 0.025\varphi$ each. The seeding energy threshold for the algorithm is 2.5 GeV, and from the MC simulation of W and Z decays, the efficiency is expected to be about 97% at $E_{\mathrm{T}} = 7$ GeV and almost 100% at $E_{\mathrm{T}} > 20$ GeV. During the second stage every cluster is matched with a track reconstructed in the inner detector. The reconstruction of the track is pretty straightforward: it is seeded by the hit in the innermost layer of the tracker, and then propagated outside by connecting the closest hit of the adjacent layer [101]. The matching algorithm tries to find the track with the impact point within of $|\Delta\eta| < 0.05$ and $|\Delta\varphi| < 0.1$. The size of $\Delta\varphi$ is taken bigger to account for the possible bremsstrahlung losses during the pass of the solenoidal magnetic field. If there are several such tracks, the closest one is chosen, with the priority given to the tracks with the hits in pixel detector or SCT (as opposed to the TRT, see section 4.2). If no track can be found, the candidate is classified as a photon, and the photon-reconstruction algorithm is used for it. The final stage is the calculation of the cluster energy and other cluster variables. It is during this stage, when the differences between EMB and EMEC come into play. The size of the window differs for these two detectors: it is 3×7 cells in EMB and 5×5 in EMEC in the same units of $0.025\eta \times 0.025\varphi$. The η and φ spatial coordinates of the electron are taken from the matched track at the interaction vertex, the energy is calculated from the cluster. Still, all the variables from both cluster and matched track are saved and available separately for the needs of the analysis.

8.1.2 Forward

The forward region of the calorimeter starts from $\eta = 2.5$ and includes two detectors: the inner wheel of the EMEC and FCAL. There is no tracker in this region, so the reconstruction algorithm deals only with clusters. Because of this the reconstruction algorithm can't make a difference between electrons and photons, and electrons and positrons. For this region another cluster-construction algorithm is used which is called "topological clustering" [102]. This algorithm is very effective at noise suppression, which is very important for forward region. The algorithm is seeded by a single cell with an energy significance which is above a high signal to noise ratio threshold. Then the cluster is expanded by adding the neighbor cells with the said ratio being above the medium threshold, and then finalized by taking in all the cells above low threshold. The standard configuration for this algorithm for EM calorimeters is called "EM 633", with the thresholds being 6, 3 and 3 respectively. If the process of cluster expanding proceeds to the hadron calorimeter, the configuration "Had 420" is used. The spatial coordinates of the reconstructed electron is then calculated as a barycenter of the cluster. This algorithm produces the variable-sized cluster, as opposed to the sliding-window algorithm, which produces a cluster with a fixed size. Because of the three-dimensional nature of the cluster expanding used in the algorithm, it is very effective in suppressing the pileup. The effectiveness in terms of electron reconstruction is predicted (via MC simulation) to be above 99% for the electrons with $E_{\mathrm{T}} > 20$ GeV. To be reconstructed, the electron candidate must have $E_{\mathrm{T}} > 5$ GeV, and have no significant energy deposits in the hadron calorimeter.

8.2 Electron identification

The electron identification is the next step of the data preparation, and is aimed to reduce the number of false-positive cases of the reconstruction algorithms such as background hadrons from semileptonic decays or photon conversions. The identification is implemented using several cuts on cluster, track, and combined cluster-track variables. For use in the analysis, three sets of cuts were introduced, with every consecutive being a superset of the predecessor. These sets are named loose, medium and tight. Each one of them is more effective in background suppression than the previous, but is less effective in terms of identification efficiency, as the identification efficiency also drops (see Section 12).

The description of these identification criteria is described below.

- **Loose**: This is the least demanding criteria, that performs only a basic cuts on the reconstructed electron candidate. It takes into account the shower shape variables from the EM calorimeters and the hadronic leakage information. The shower shape variables were previously mentioned in Sec. 6.2.1.2. The list of the variables is given in Tab. 8.1, while the distributions can be seen in Figures 6.8 to 6.13. The distributions usually have peaks, where the “good” electrons are located, and tails, with “bad” electrons. The thresholds for each variable is picked experimentally. The criteria also increases the requirements on the quality of the track and of the track-cluster matching. It improves the rejection of the hadronic background by a factor of ~ 5 in the range $30 < E_{\mathrm{T}} < 40$ GeV compared to the bare reconstruction algorithms, while not affecting the identification efficiency.

- **Medium**: This is a more demanding version of the “loose” criteria, with a stricter requirements on the same variables. It also introduces several new requirements, mostly on the track, the most important one being the requirement of the hit in the innermost layer of the tracker, which aims to suppress the photon conversion background. It is ~ 10 times more efficient in background rejection than “loose”, but has a drawback of having a worse identification efficiency.

- **Tight**: This one makes a full use of all the identification tools available. In addition to more strict requirements for every variable used in “medium”, it also makes new: on the track extension in the TRT and on the ratio between track momentum and cluster energy. It also takes into account the list of reconstructed photon conversions associated with the same vertex. Overall, it increases the background rejection by the factor of two with respect to “medium”.

- **Forward Id**: For the forward region of the calorimeter, the identification criteria follow the similar pattern as for the central region, because of lack of the tracking information, only the shower parameters are taken into account. The shower shape, the longitudal, transverse and normalized lateral momenta are all used for the identification process. In 2011, the pileup increased drastically on the forward region, so the criteria became more strict, and are derived from the previous data. The thresholds come in four bins based on the number of primary vertexes reconstructed in the event ($N_{PV} = 1-3$, $4-6$, $7-10$, > 10). All the three criteria use the same set of variables, but progressively increase the thresholds, with the *fwdTight* rejection factor being 2 to 3 times bigger than the *fwdLoose* one.

The criteria for the forward electrons are different, since the forward region lacks the tracker, and has a significantly higher pileup. The cuts are applied to the cluster itself, and take into account such parameters as longitudinal second momentum, transverse second momentum, normalized lateral momentum and so on. The fact that the reconstruction algorithm for forward region produces a three-dimensionally shaped cluster helps greatly. The loose, medium and tight criteria are also defined for the forward region, but work on the same variables, only with consecutively stricter requirements.

Starting from 2011 the new set was introduced which was more attuned to the data and was more effective at background-suppression. The new set was called “IsEM++” criteria (the previous was called just “IsEM”), and consist respectively of loose++, medium++ and tight++. The difference between the sets is mostly the tunes to the variables thresholds.

Name	Description	Variable
Shower depth	The distance of the shower barycenter from the calorimeter front face measured along the shower axis	λ_{center}
Maximum cell energy	Fraction of the cluster energy in the most energetic cell	$f_{\max}$
Longitudinal second momentum	Second momentum of the distance of each cell to the shower center in the longitudinal direction (λ_i)	$\langle\lambda^2\rangle$
Transverse second momentum	Second momentum of the distance of each cell to the shower center in the transverse direction (r_i)	$\langle r^2\rangle$
Normalized lateral momentum	Calculated as $\frac{w_2}{w_2+w_{\max}}$ where w_2 and $w_{\max}$ are second momenta of r_i for different weights per cell	w_{norm}
Normalized longitudinal momentum	Calculated as $\frac{\lambda_2}{\lambda_2+\lambda_{\max}}$ where λ_2 and $\lambda_{\max}$ are second momenta of λ_i for different weights per cell	λ_{norm}

Table 8.1: The shower shape variables used in the forward electron identification.

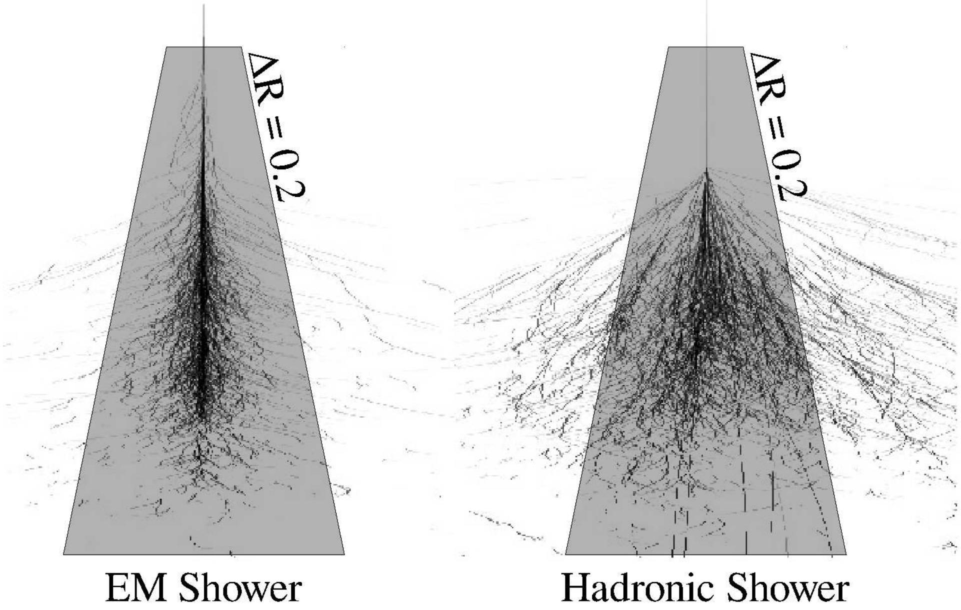

Figure 8.1: A diagram showing the usual shape of EM and hadron showers, and how isolation cones cover these showers.

8.3 Electron isolation

To further suppress fake electron background, the isolation check is also used. The isolation check relies on Etcone variable, which is the sum of the energy in a cone surrounding the cluster, excluding the cluster itself. The cone is calculated using the η-φ-r polar coordinates as a space around the cluster bounded by constant lateral shift from the cluster's reconstructed coordinates $\Delta R = \sqrt{\Delta\eta^2 + \Delta\varphi^2}$. The radius of the lateral shift that was used is written in the name of the variable, so there are several of them, e.g. Etcone20, Etcone40, etc, where 20 or 40 means $\Delta R = 0.20, 0.40$ [103]. The Etcone variable can use cluster E_{T} as well as track E_{T}, and different isolation criteria use one or another or both. The said criteria is just the cut on the ratio of the Etcone energy to the cluster energy. If the ratio is low, we are dealing with the high-isolation electron. This is the best-case scenario. The higher values of the ratio means low-isolation electron, the high error in energy reconstruction is expected for this kind of electrons. The high value of the ratio means that the electron is most likely a fake: a misidentified muon or hadron jet with a mismatched track.

For $Z \to ee$ central-forward analysis, the isolation cuts named Iso98 for Etcone20 and Iso97 for Ptcone40 were used for the central electron. It allowed to reduce the background to the factor of 2, while still retaining the electron efficiency of 97-98%.

CHAPTER 9

Analysis Software (ZeeD)

ZeeD ($Z \rightarrow ee$ DESY) is a software solution, developed internally by the DESY ATLAS Standard Model group. It is based on the ATHENA framework that is largely used in ATLAS, but uses it mostly for the input data reading, the AOD format, which is a standard for ATLAS. For performance reasons, the first step in the analysis is the conversion of the data to ZeeD internal format called TTrees (this is actually the name of the class in the ROOT framework used in this format, but in this section any mention of TTrees refers to ZeeD data format). This conversion allows for substantial speedup of the analysis, as well as to considerably reduce the space needed for the data storage.

The later stages of the analysis include the selection (application of cuts), reweighting (in case of MC sampes) and plotting. ZeeD also allows to apply the systematic shifts as well as use ToyMC for uncertainties propagation studies.

The structure of ZeeD can be seen in Figure 9.1. During the analysis, `ZeeDLauncher` initializes the ATHENA framework and provides all the configurations first. The framework gives access to the input data files and the configuration parameters. Then `ZeedAnalysisLoop` starts to iterate through the events in the input files. For each event it may run several iterations of the analysis, if the systematic study is required (one iteration for each systematic shift). In case of ToyMC systematic study (the systematic propagation technique that will be discussed in Section 9.6), the number of iterations can be as high as several hundred. Each iteration is contained within a separate `ZeeDAnalysisChain` which represents the conditions of the required systematic shift (including the “no shift” case). The actual corrections and possible systematic shifts is applied inside `ZeeDCalculator`, which also takes input from several external tools developed inside ATLAS. Corrected (and possibly shifted electrons are then passed to the various `ZeeDFinder`’s, which then try to construct all possible boson candidates from them. Every analysis has its own finder which only constructs the bosons that comply with the respective analysis criteria, e.g. $Z \rightarrow ee$ central-central, $Z \rightarrow ee$ central-forward or $W \rightarrow e\nu$. The bosons are then passed to the `ZeeDAnalysisCutSelector` which applies the set of cuts to each boson candidate. There are several selectors, one for each set of cuts that is used in any analysis, sometimes with several variations for different cross-checks. After all cuts are applied, the boson candidate passing the tightest selection is considered to be the best candidate, and if it also passes all the cuts mandatory for the analysis, it is passed to `ZeeDHistManager` to be included in the final results. In the following sections all these stages and subsystems of ZeeD will be described in details.

9.1 TTrees

The data from the ATLAS detector comes in the form of the AOD files, which a special format based on the ROOT data file format and developed internally by the ATLAS. The format allows the seamless reading and writing of the various data objects (e.g. tracks, EM clusters, reconstructed particles, etc) within the ATHENA framework. In AOD files all the information reconstructed from the collision is stored. In case of simulated events (i.e. MC) there is also the information about the generated particles, the so-called “truth particles”, which can be used to determine the efficiency of the reconstruction algorithms and the analysis software.

Most of the information stored in the AODs is not used in the $Z \to ee$ analysis, which only needs reconstructed electrons. And not even all the information available for the electrons is needed, as we only apply cuts and construct various differential cross-sections. During the analysis workflow, ZeeD uses about 0.1% of all the information stored in the AODs, but because of the ATLAS framework structure, all the content of it should be read from the store and preloaded into the memory, which consumed most of the time needed for the analysis iteration. Also, because of the nature of the ATLAS data storages and the GRID farms used for the analysis, it was prone to errors, and it would require several attempts and consume much time to finish even one iteration.

The solution for this problem is to extract the needed information from the AOD files and store it in the simplified structure in ROOT ntuples. Similar solution was later used for the AOD successor - xAOD format. But whereas xAOD allows all this to be done automatically, for the 2011 the custom tool for manual conversion had been developed. The software chain for the TTree writing is the same as the analysis chain. The data is read from the AODs, the preselection cuts are applied to reduce the amount of data, and the output information is written out, which in this case is the raw events.

Because of this similarity, the same software - ZeeD - was used for the TTrees production as well. It is capable of reading data from AODs, it has all the cuts applicable for preselection, and it is capable of outputting any kind of data from the selected events. With the corresponding setup, the ZeeD workflow will be suitable for this production.

9.2 Boson Finder

The main target of all the analyses that are conducted using the ZeeD software are the Z bosons, so finding all the possible Z boson candidates in every event is always the first task. The ZeeD component that does that job is the boson finder class. On the basic level it just creates a boson candidate for every possible pair of electrons, but further in the analysis it keeps track of all the bosons and records all the intermediate results for each one. Ultimately, we won’t accept more than one boson from any event, so every boson candidate is assigned a

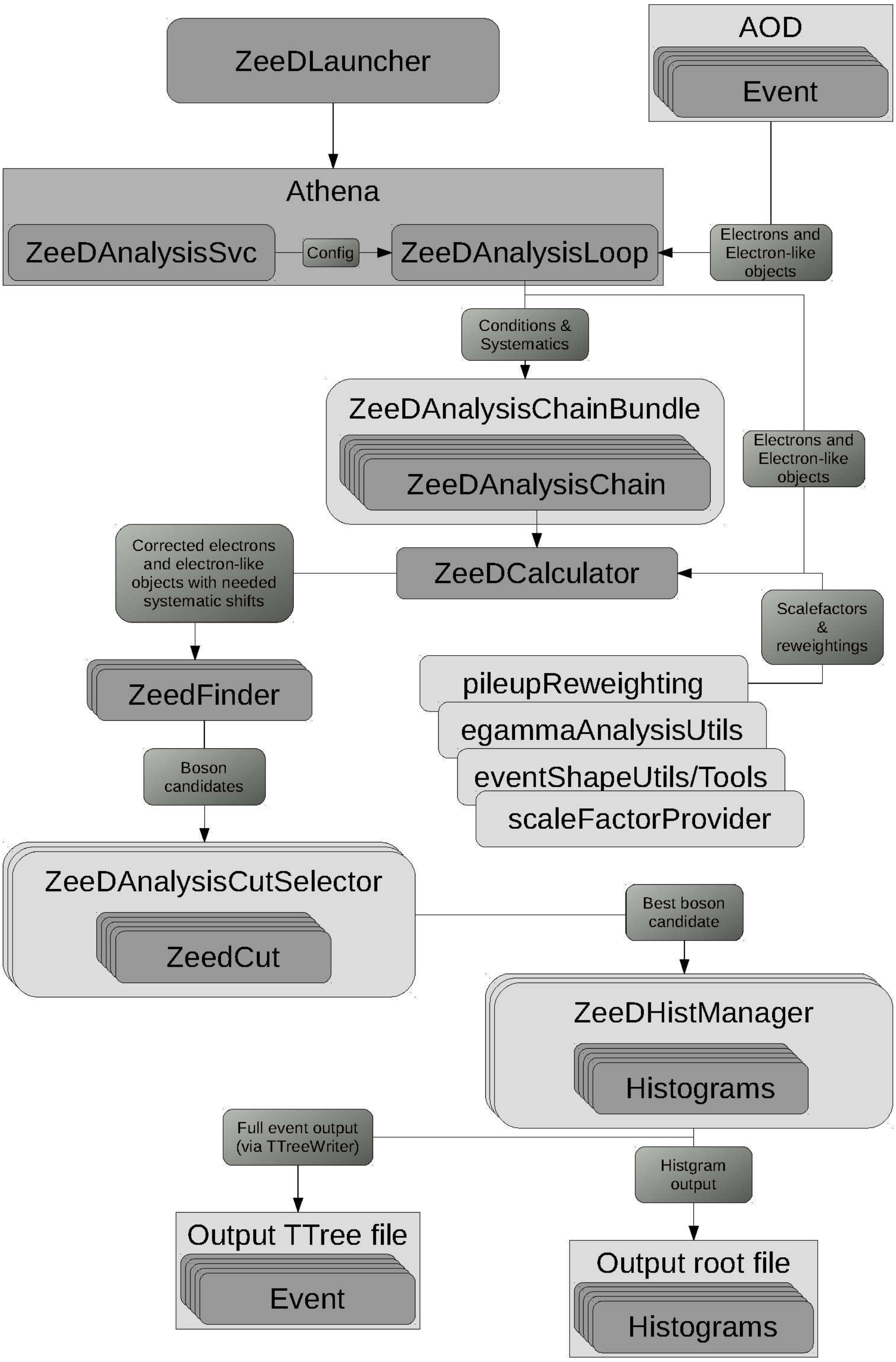

Figure 9.1: The functional flowchart of the ZeeD analysis software.

special “score” of how well it passes the various cuts: every passed cut adds one point to the boson’s score, except for one cut that checks that the di-electron mass is very close to M_Z, which adds ten points. When there are several boson candidates that pass all the required cuts, the candidate with the highest score is picked for the final results. In case of the final $Z \to ee$ analysis this situation is impossible, though, as we require not more than two suitable electrons. This mechanism is used for various tests and cross-checks.

9.3 Cuts

The analysis implications of different cuts will be discussed in the Section 10.2. Here we’ll discuss the technical aspects of the event selection.

From the technical point of view, every cut is a restriction on one or several variables of the reconstructed event. Every event can pass or fail a given cut, and the infrastructure should be able not only to provide information whether some event passed all the cuts or not (which is the only thing that is important for the analysis itself), but also to show the results of all the cuts separately. This is called a “cut-flow” and it is used for debugging purposes and cross-checking. In the situation when different groups using different software come to different results for the same analysis, the ability to find out on which cut every particular event was filtered out is very helpful. With it we can find out which cut gives different results across different analysis groups.

The other functionality important for the cuts facility is the cut reversal which is useful for the background estimation. The background estimation methods (discussed later in Section 13) require to select the events where electron pass some specific cuts, but fail some other specific cuts. To achieve that, the cuts framework construct the bit-mask for every event, where every bit corresponds to the cut, and displays whether that event passed or failed that cut. After the bit mask is composed, we can compare it to the desired bit-mask, and include or exclude the event from the analysis.

9.4 Reweighting

The reweighting of the MC events is used for the fine-tune of the simulation to the real data. The weights are calculated based on the well defined distributions in data (such as the trigger efficiencies) and bring the corresponding MC distributions in accordance with the data. The calculation of the weights is done using some well-measured process. For instance, $Z \to ee$ decay is good for calculating the trigger efficiency, since it has a low background in the peak region, and has two electrons which allows the use of the tag and probe method. The calculation of the weights is thus done by conducting the same analysis on MC and real data without any corrections, and then comparing the distributions, for which we want to introduce reweighting. Weights are usually applied in bins, so the result of the weight calculation would be a histogram, sometimes two-dimensional, which would cover the kinematic plane for the variable being reweighted. Apart from the weight itself, the statistical and systematical uncertainties for every bin are also calculated, and stored in the similar histograms.

After the weights are calculated, they are used during the analysis. The weights are picked for every event based on its properties, and then the final weight of the event is calculated by multiplying all the weights from different corrections. This weight is later used during the histograms plotting. Since every weight comes with the statistical and systematical uncertainties, they also contribute to the calculation of the final error for the analysis. The process of calculation of the impact of different uncertainties to the final combined error would be discussed in the Section 9.6.

9.5 Histogram managers

The results of the analysis are the histograms, showing the various distributions of the physical quantities. The facilities responsible for that are the histogram managers. Each manager represents some aspect of the analysis, and creates and fills one or several histograms, which are thus grouped in it by their role. Each of the managers can be attached or detached during the launch setup, which allows to conduct various analyses with the same software, as long as this analysis deals with electrons, muons, and missing E_{T} (the only kind of data that ZeeD extracts from the egamma data stream).

For the $Z \to ee$ analysis the important managers would be an electron manager (plots the various distributions of the electrons properties, such as energy, E_{T}, geometrical variables, etc), a ZCF manager (plots the properties of the central-forward Z-bosons), and (in case of MC samples) the truth managers (plots the truth information for the given event).

There is also one special histogram manager, which actually doesn't plot any histograms, but uses the same interfaces. It is the ZeeD TTree writer, which dumps out the content of the event in the ROOT tuples. This histogram manager is used to produce the TTrees that were previously discussed in Section 9.1.

9.6 Systematics and ToyMC

One of the most important aspects of the analysis is the uncertainty estimation. The uncertainties come in two forms: correlated and uncorrelated between bins. A statistical uncertainty is always considered to be uncorrelated, while the systematical uncertainty can be of both kind, as well as a mixture of them. Two methods of the uncertainty propagation exist: the offset method and the ToyMC method. The first method is usually employed in case of fully correlated uncertainties, and consists of calculating the results with all the source distributions shifted up or down by the amount of the corresponding uncertainty. The source distributions here are not only the data itself, but also all the scale factors and correction, which all come with their own uncertainties. Each uncertainty should be shifted separately and the shift in the produced result would amount to its propagated value.

The ToyMC method is more advanced as it allows to propagate both uncorrelated uncertainties, and the mixture of the correlated and uncorrelated ones in the form of so-called combined ToyMC. The method consists of producing of a high number of variations of the input data by the use of so-called biases, that are the Gaussian distributed shifts with the standard deviation equal to the value of the statistical and uncorrelated uncertainties

$$B^i = \Delta S_{\text{stat+uncor}} \cdot \text{Gauss}(0,1) \quad i = 0, ..., N_{\text{toys}}\,, \tag{9.1}$$

where B^i is a bias and N_{toys} is order of hundreds. In case of the combined ToyMC, all sources of the correlated errors also contribute to the bias

$$B^i = \Delta S_{\text{stat+uncor}} \cdot \text{Gauss}(0,1) + \sum_s S^k_{\text{cor},s} \cdot \text{Gauss}(0,1)\Bigg|_k \quad i = 0, ..., N_{\text{toys}}\,, \tag{9.2}$$

where B^i as again a bias, and s runs over all sources of the correlated uncertainties. The main difference in a treatment of the correlated and uncorrelated uncertainties is that the gauss value for $S_{\text{stat+uncor}}$ is constant bin-wise, so the whole distribution is shifted uniformly, while an case of $S^k_{\text{cor},s}$ every bin is treated independently, which is denoted by the index k which runs over bins. The biases are then applied (added) to the input data to construct a set of N inputs. After the unfolding procedure (see Sections 11.1 and 11.2 for the description of the unfolding) this results in N unfolded distributions. The distributions can then be fitted by gauss to find out the median value and an error, which would be the standard deviation of the fit, or alternatively, if the results of the analysis are intended to be used in a consequent ToyMC, then the distributions are combined into a covariance matrix in order to decompose it to nuisance parameters to find out the correlated and uncorrelated components of the unfolded uncertainties. More on the correlation studies can be read in [104].

ZeeD software offers an easy way to conduct a ToyMC uncertainty propagation through the system of so-called “shelves” or “analysis chains”, which is essentially a variation on the same analysis with different input parameters. With enabling the ToyMC method, ZeeD will create a large number of shelves (the default being 100) and automatically calculates the biases for every shelve by the use of the combined ToyMC method. The results for all the variations are then stored independently in the output file for future process.

CHAPTER 10

Event Selection

The event selection is one of the main phases of the analysis, which is focused on suppressing of as much as possible background events while keeping the signal events. The process of selecting the suitable events goes in three stages. The first stage is the online triggers, which, as name suggests, occurs during the data taking, even before the data is written on the storage. The specifies of the trigger work was described in the corresponding section (see Section 4.8). The other two stages are the pre-selection and analysis selection (or just selection), and they are specific to our analysis software ZeeD (described later in Section 9), although the division of the selection in such a way is a common practice because of the large amount of data. These two stages would be described in the following sections.

10.1 Analysis preselection

The goal of the preselection stage is to reduce the amount of data (by removing "non-interesting" events) while not biasing the samples in regards of the $Z \rightarrow ee$ analysis. There are two flavors of preselection: the two-electron preselection and the one-electron. The cut for the two-electron stream requires $p_{\mathrm{T}} > 14$ GeV for both electrons and the cut is $p_{\mathrm{T}} > 20$ GeV for one-electron. For the central-forward $Z \rightarrow ee$ analysis the single-electron stream is mostly used, but the di-electron is also used in some cases, for instance for the trigger efficiency scale factors calculation (tag&probe method). Such cuts do not affect any possible distribution within the $Z \rightarrow ee$ analysis, be it the signal or the background studies. During the preselection stage we also extract all the data that is relevant to the analysis, while disregarding all the rest of the data stream (e.g. muons, jets and so on). This allows us to reduce the physical amount of data from terabytes to just mere gigabytes, and to speed-up the analysis by the factor of hundreds. The resulting pre-selected data is very similar to the D3PD from the programming point of view (which is a commonly used data format that was developed after AOD, and was later incorporated in AOD successor - xAOD), but is designed specifically for the needs of $Z \rightarrow ee$ analysis (see Section 9.1 for details).

10.2 Analysis cuts

The application of cuts is one of the most important parts of the analysis. During this stage we try to suppress the background while keeping the signal intact. The cuts can be divided in three categories: the technical cuts, the kinematic cuts and the electron "goodness" cuts. The technical cuts are applied on a per-event basis. Here we check that no problems were encountered during the event taking. This includes a so-called good run list, which excludes the events taken during the runs with observed problems in the detector, and the OQ-map (object quality map) which is a list of a regions of the calorimeter which are known to be faulty, and so the cut excludes all the events with at least one electron depositing energy in one of those regions.

The kinematic cuts deal with the kinematic properties of the electrons: we require only two electrons, with one being inside the central region and one inside the forward region, both are reconstructed with the proper reconstruction algorithm and both meeting the selection requirements for the kinematic properties.

Finally there are cuts on the quality of the electrons, which involve passing certain IsEM criteria and a certain isolation criteria.

Every group of cuts will be described in details.

10.2.1 Data quality cuts

- **Good Run List**: This cut drops every event that was taken during the non-successful runs of the LHC. The list of the good runs is compiled by the Data Quality group and is the same for all analyses.
- **Object Quality Maps**: This cut drops every electron that was reconstructed inside one of the faulty regions of the calorimeter. The events with such electrons can still be used in the analysis, if they have another two good electrons.
- **LAr Veto**: This cut drops every event that was taken while the LAr calorimeter was malfunctioning, as indicated by the `LArErrorState` property.

10.2.2 Kinematic cuts

- **Two good electrons per event**: This cut drops all events that have the number of good electrons other than two. The Drell-Yan process produces exactly two electrons, so everything else is a background for our analysis. In case of central-forward analysis, the cut can be renamed as **1+1 good electrons per event**, as we require exactly one good electron in the central region, and one in the forward region.
- **Minimum electron p_{T}**: This cut drops all electrons with the $p_{\mathrm{T}} < 20$ GeV. We do not have adequate efficiency corrections for the electrons with low p_{T}.

- **Electron $|\eta|$**: This cut drops all electrons which have a cluster that is reconstructed outside the required η regions: $|\eta| < 2.47$ for the central electron and $|\eta| > 2.52$ for the forward electron.
- **Electrons are outside the crack regions**: This cut drops all electrons reconstructed inside the crack regions of the calorimeters. For the central electrons the cracks are $1.47 < |\eta| < 1.52$ and $|\eta| > 2.47$, for the forward electrons it is $3.16 < |\eta| < 3.35$
- **Z boson mass**: This cut drops all events with the di-electron mass outside the mass window range ($66 < |M_{ee}| < 116$ GeV for peak mass and $116 < |M_{ee}| < 150$ GeV for high mass regions).
- **Number of tracks at primary vertex**: This cut drops all events that do not have a vertex with at least three tracks.

10.2.3 Electron quality cuts

- **A track for the central electron**: This cut drops all events with the central electron having no track. The “author” cut which requires the specific author for every electron supersedes this cut, but it is kept for compatibility purposes.
- **Central electron IsEM**: This cut requires the central electron to satisfy the IsEM criteria (described in Section 8.2).
- **Forward electron IsEM**: This cut requires the forward electron to satisfy the IsEM criteria.
- **Central electron isolation**: This cut requires the central electron to satisfy the isolation criteria (described in Section 8.3).
- **Electron author**: This cut requires the proper author (described in Section 8.1) for both central and forward electron.

The cutflows, i.e. the tables that shows how many events pass any given cut, can be seen in Tab. 10.1 for data and in Tab. 10.2 for the signal MC sample. The relative efficiency shows how many events pass the cut relative to the previous cut, while the absolute efficiency shows the number of events relative to the total number of events.

Cut	events	ϵ_{rel} [%]	ϵ_{abs} [%]
All events (after pre-selection)	234255443		100.00000
primary vertex w. > 2 tracks	234127638	99.9454	99.94544
veto LAr noise bursts	233365291	99.6744	99.62001
$\lvert\eta_{cnt}\rvert < 2.47$, $2.5 < \lvert\eta_{fwd}\rvert < 4.9$	138946695	59.5404	59.31418
excl. $1.47 < \lvert\eta\rvert < 1.52$	127877309	92.0334	54.58883
excl. $3.16 < \lvert\eta\rvert < 3.35$	124775277	97.5742	53.26462
$pt_e^{cent.} > 25\,\mathrm{GeV}$	74478333	59.6900	31.79364
$pt_e^{fwd.} > 20\,\mathrm{GeV}$	8404968	11.2851	3.58795
Author	8404244	99.9914	3.58764
good object quality	8338286	99.2152	3.55948
Tight++	1537446	18.4384	0.65631
FwdTight	370376	24.0903	0.15811
Iso98Etcone20	355029	95.8564	0.15156
Iso97Ptcone40	340852	96.0068	0.14550
single-lepton trigger	339235	99.5256	0.14481
MaxTwoGoodElectrons	339235	100.0000	0.14481
$66 < m_{ee} < 116$ GeV	321575	94.7942	0.13728
$116 < m_{ee} < 150$ GeV	7740	2.28	0.0033

Table 10.1: The cutflow for the $Z \rightarrow ee$ CF data selection both for peak and high mass windows.

Cut	events (weighted)	ϵ_{rel} [%]	ϵ_{abs} [%]
All events (after pre-selection)	19783527.83		100.00000
primary vertex w. > 2 tracks	19659928.15	99.3752	99.37524
veto LAr noise bursts	19659928.15	100.0000	99.37524
$\lvert\eta_{cnt}\rvert < 2.47$, $2.5 < \lvert\eta_{fwd}\rvert < 4.9$	12425328.01	63.2013	62.80643
excl. $1.47 < \lvert\eta\rvert < 1.52$	11837779.90	95.2714	59.83655
excl. $3.16 < \lvert\eta\rvert < 3.35$	11431076.75	96.5644	57.78078
$pt_e^{cent.} > 25\,\mathrm{GeV}$	7959710.26	69.6322	40.23403
$pt_e^{fwd.} > 20\,\mathrm{GeV}$	3207445.87	40.2960	16.21271
Author	3206917.09	99.9835	16.21004
good object quality	3186720.53	99.3702	16.10795
Tight++	2228171.55	69.9205	11.26276
FwdTight	1684155.81	75.5847	8.51292
Iso98Etcone20	1661813.91	98.6734	8.39999
Iso97Ptcone40	1629799.05	98.0735	8.23816
single-lepton trigger	1584699.06	97.2328	8.01019
MaxTwoGoodElectrons	1584699.06	100.0000	8.01019
$66 < m_{ee} < 116$ GeV	1542376.88	97.3293	7.79627
$116 < m_{ee} < 150$ GeV	42206.05	2.66	0.21

Table 10.2: The cutflow for the $Z \to ee$ CF MC selection both for peak and high mass windows. The number of events is corrected for weights.

CHAPTER 11

$Z \to ee$ cross section measurement

The measurement of the $Z \to ee$ production cross-section is the main purpose of this work, and the details of the methodology of the measurement are discussed in this chapter.

The ATLAS detector, like every other physical device, has its limitations, and the signal obtained from the detector is thus distorted. The process of estimating the results that would have been achieved with an ideal detector based on the results using the real detector is called the unfolding process (also called "deconvolution" or "unsmearing" in mathematical literature), and is the one of the most important stages of the measurement of the cross-section. The main idea of the unfolding is that if $f_{\text{meas}}(x)$ is the spectrum of a value measured using the real detector and $f_{\text{truth}}(x)$ is the the spectrum that would have been measured with an ideal detector, then

$$f_{\text{meas}}(x) = \int R(x|y)\, f_{\text{truth}}(y) dy \tag{11.1}$$

where $R(x|y)$ is the detector response function. In case of binned distribution this equation can be written as

$$v_i^{\text{meas}} = \sum_j R_{ij}\, v_j^{\text{truth}} \quad i, j = 1, ..., N \tag{11.2}$$

where v_i^{meas} and v_i^{truth} are the measured and ideal values accordingly. Generally speaking, the number of bins in v^{meas} and v^{truth} spectra can be different, and the matrix R_{ij} would be rectangular, but in this analysis the same binning is used for both. The main task of unfolding is to determine the response matrix, and then to calculate the unfolding matrix based on it. The easiest solution would be to just invert the response matrix:

$$v_i^{\text{truth}} = \sum_j R_{ij}^{-1}\, v_j^{\text{meas}} \quad i, j = 1, ..., N \tag{11.3}$$

which is not always the best choice, because it produces very large distortions in case of limited statistics. The task of propagating the systematic uncertainties through the unfolding process also must be solved.

There are two methods of unfolding that are usually employed by ATLAS analysis groups: the bin-by-bin correction, and the Bayesian unfolding [105]. There are several advantages and disadvantages in both methods, but the main criteria of the preference of the Bayesian or bin-by-bin unfolding lies in two important factors: purity and stability. These two factors are calculated as follows:

$$P^i = \frac{N^i_{\mathrm{rec\&gen}}}{N^i_{\mathrm{rec}}}\,, \;\; S^i = \frac{N^i_{\mathrm{rec\&gen}}}{N^i_{\mathrm{gen}}}\,, \tag{11.4}$$

where:

- $N^i_{\mathbf{rec\&gen}}$ is the sum of event weights which were generated and reconstructed in bin i.
- $N^i_{\mathbf{rec}}$ is the sum of event weights reconstructed in bin i.
- $N^i_{\mathbf{gen}}$ is the sum of event weights generated in bin i.

The purity is thus a measure of in-migration, which shows the amount of foreign events reconstructed in the given bin, while the stability is a measure of the out-migration, which shows the amount of events that were reconstructed in other bins for every given bin. In terms of response matrix, the distribution with high purity and stability will have a mostly diagonal matrix. This will warrant for a use of a bin-by-bin unfolding. This method, dealing with every bin independently, will produce a diagonal matrix. But if the migrations between bins are substantial, ignoring it will highly increase the distortions in the unfolded results, in which case the Bayesian unfolding becomes preferable. The results of the purity and stability studies for the $Z \to ee$ central-forward analysis suggested that the Bayesian unfolding would be more effective (see Figure 11.1 for the exact values of the purity and stability of the 2011 $Z \to ee$ central-forward analyses). In the following sections the methodology for both bin-by-bin and Bayesian unfoldings are shown. Also, the methodology of the result combination is explained, which mathematically is very close to unfolding, as it is the same inverse problem (when the same distribution is measured with several partially independent methods, their combination becomes a complicated task).

The differential cross-section measurement was done in absolute rapidity binning. The binning is the same for CC and CF analyses in the region that is covered with both of them, which allows for the easy combination of the results. The binning is shown in Tabs. 11.1 and 11.2. The mass binning for the double-differential CF analysis had only two bins: the peak-mass window $66 < m_{ee} < 116$ GeV and the high-mass window $116 < m_{ee} < 150$ GeV.

11.1 Bin-by-bin unfolding

The bin-by-bin unfolding doesn't take into account the migrations between bins, and works with every bin separately. The unfolded value can be translated into the cross-section value, and the formulae for both integrated and differential cross-sections are:

$$\sigma_{tot} = \sigma_Z \times BR(Z \to ee) = \frac{N - B}{C \cdot E \cdot A \cdot L_{int} \cdot \Gamma}\,, \tag{11.5}$$

where:

- N is the number of candidate events measured in data.

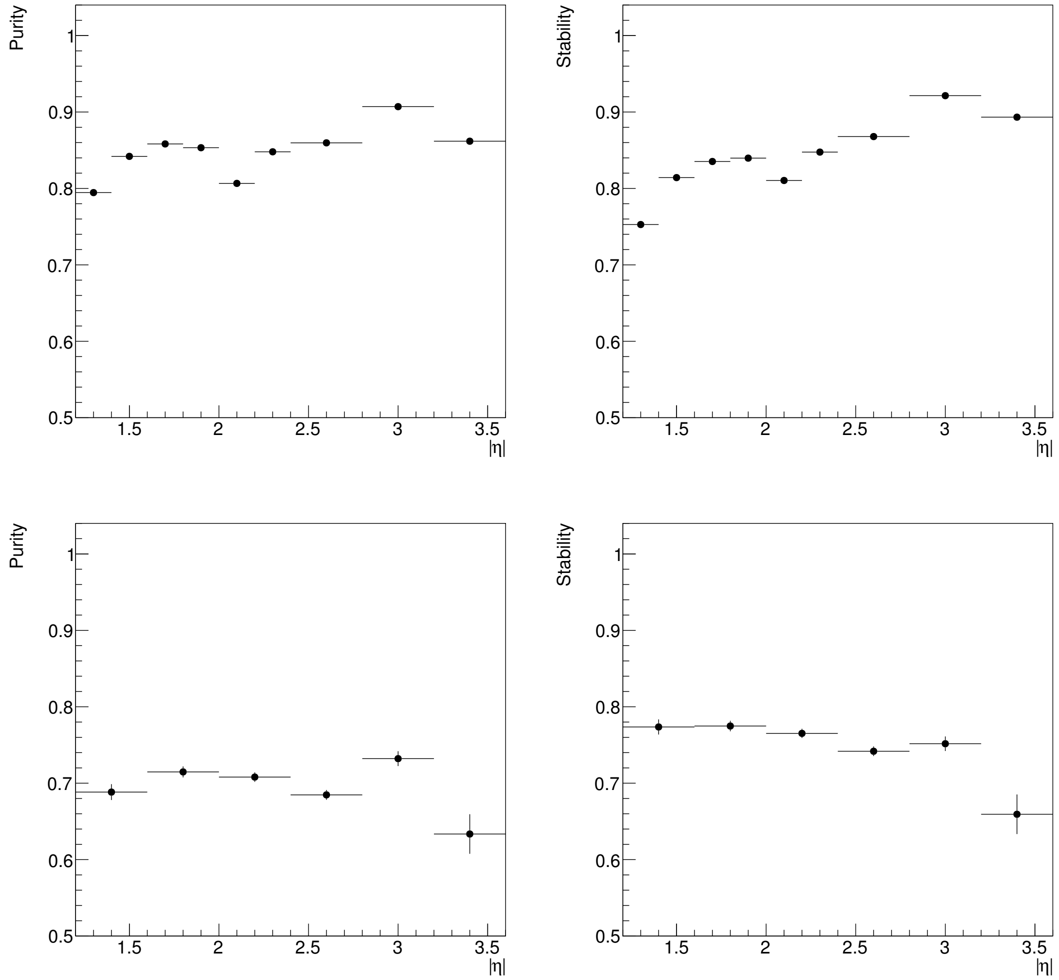

Figure 11.1: Purity (left) and stability (right) for the Z central-forward peak mass (top) and high mass (bottom) analyses. The plots were made using the $Z \to ee$ MC samples with standard CF analysis cuts.

Boundaries
$1.20 < \lvert y_Z \rvert < 1.40$
$1.40 < \lvert y_Z \rvert < 1.60$
$1.60 < \lvert y_Z \rvert < 1.80$
$1.80 < \lvert y_Z \rvert < 2.00$
$2.00 < \lvert y_Z \rvert < 2.20$
$2.20 < \lvert y_Z \rvert < 2.40$
$2.40 < \lvert y_Z \rvert < 2.80$
$2.80 < \lvert y_Z \rvert < 3.20$
$3.20 < \lvert y_Z \rvert < 3.60$

Table 11.1: Bins in $|y_Z|$ which are used for the $Z \to ee$ CF analysis for peak mass window ($66 < m_{ee} < 116$ GeV).

Boundaries
$1.20 < \lvert y_Z \rvert < 1.60$
$1.60 < \lvert y_Z \rvert < 2.00$
$2.00 < \lvert y_Z \rvert < 2.40$
$2.40 < \lvert y_Z \rvert < 2.80$
$2.80 < \lvert y_Z \rvert < 3.20$
$3.20 < \lvert y_Z \rvert < 3.60$

Table 11.2: Bins in $|y_Z|$ which are used for the $Z \to ee$ CF analysis for high mass window ($116 < m_{ee} < 150$ GeV).

- B is the number of background events (see Section 13 for further information on the background estimation).
- L_{int} is the integrated luminosity corresponding to the dataset.
- Γ is the bin width for differential measurements. Measurements in rapidity quantities η and y are done in absolute binning as final value, therefore Γ for them is doubled.
- C, E, and A are efficiency-acceptance corrections calculated from (binned) sum of weights of MC events generated or reconstructed with analysis cuts applied. They take the uncorrected event yield in steps to different levels:
  - The coefficient for a *genuinely experimental fiducial volume in each channel* as defined by the individual cuts is reached after dividing by

    $$C = \frac{N_{\mathrm{MC,rec}}}{N_{\mathrm{MC,gen,cutexp}}} \,. \tag{11.6}$$

    C is corrected for any discrepancy in the electron efficiencies between data and MC as described in Section 12. Here the sum of weights of MC events generated after experimental fiducial acceptance cuts ($N_{\mathrm{MC,gen,cutexp}}$) and the sum of weights of MC events after simulation, reconstruction and experimental selection ($N_{\mathrm{MC,rec}}$) enter.
  - The coefficient for a *common fiducial volume* is a theoretical extrapolation designed to unify the fiducial volumes of different flavors of $Z \to \ell\ell$ analyses. Since the electrons and muons are detected by the different parts of the ATLAS detector, these particles are detected in different parts of the kinematic space. The EM calorimeters that detect electrons have a coverage of $|\eta| < 5.2$, while muon chambers have $|\eta| < 2.4$. These differences in the kinematic coverage makes combination of the results of corresponding analyses a big challenge. Therefore the common fiducial volume covering both kinematic spaces is introduced.

    $$E = \frac{N_{\mathrm{MC,gen,cutexp}}}{N_{\mathrm{MC,gen,cutfid}}} \,. \tag{11.7}$$

    Here the sum of weights of MC events generated after common fiducial acceptance cuts ($N_{\mathrm{MC,gen,cutfid}}$) enters.

- The coefficient for a *total cross sections* is calculated by a larger theoretical extrapolation

  $$A = \frac{N_{\mathrm{MC,gen,cutfid}}}{N_{\mathrm{MC,gen,all}}} . \tag{11.8}$$

  Here the total sum of weights of MC events generated before any acceptance cuts except m_{ee} ($N_{\mathrm{MC,gen,all}}$) enters.

While calculating the C, E and A correction factors, the QED final state radiation (FSR) must be taken into account. The results of the MC generation are so-called *born level* leptons, which are the leptons before the FSR. To simulate FSR there are two tools in use in the MC production chain: PHOTOS which is the default tool used, and SHERPA which uses another FSR algorithm and is used for systematic uncertainties evaluation. After the FSR simulation, the resulting final state leptons are called *bare leptons*. The bare leptons represent the result of the actual collision much closer than the born leptons, but because of the work of the clustering algorithms during reconstruction, bare leptons are impossible to reconstruct. To overcome this problem, another level of FSR was introduced, which is *dressed leptons*. The dressed leptons are bare leptons with the inclusion of all FSR photons within the $\Delta R < 0.1$. The dressed leptons are the leptons that most closely represent the particles that are actually reconstructed by the reconstruction algorithms.

The calculation of the correction factors is always done on the born level, because the simulation on the born level is the best from the theoretical point of view (the FSR simulation is very approximate). The C, E and A then look like this:

$$C = \frac{N_{\mathrm{MC,rec}}}{N_{\mathrm{MC,genBorn,cutexp}}} ,\ E = \frac{N_{\mathrm{MC,genBorn,cutexp}}}{N_{\mathrm{MC,genBorn,cutfid}}} ,\ A = \frac{N_{\mathrm{MC,genBorn,cutfid}}}{N_{\mathrm{MC,genBorn,all}}} . \tag{11.9}$$

And for the bare and dressed levels the cross-sections are calculated with good approximation by using the δ^{bare} and $\delta^{\mathrm{dressed}}$ which are defined as:

$$\begin{aligned} \delta^{\mathrm{bare}} &= \frac{N_{\mathrm{MC,genBare,fidcut}}}{N_{\mathrm{MC,genBorn,fidcut}}} \quad \text{and} \quad \delta^{\mathrm{dressed}} = \frac{N_{\mathrm{MC,genDressed,fidcut}}}{N_{\mathrm{MC,genBorn,fidcut}}} \\ \sigma_{fid}^{\mathrm{Born}} \cdot \delta^{\mathrm{bare}} &= \sigma_{fid}^{\mathrm{bare}} \quad \text{and} \quad \sigma_{fid}^{\mathrm{Born}} \cdot \delta^{\mathrm{dressed}} = \sigma_{fid}^{\mathrm{dressed}} . \end{aligned} \tag{11.10}$$

In terms of unfolding matrix, the values C calculated in each bin and corrected to the dressed level go into the diagonal positions of the R_{ij}^{-1}. The results unfolded with this matrix is called the *true experimental fiducial cross-section*. The additional extrapolation using the matrix constructed from the values E will produce the *extrapolated fiducial cross-section*, and finally with the values A we will get the *common fiducial cross-section* which can be used for the combination. The results for all of these cross-sections can be seen in Section 14

11.2 Bayesian (D'Agostini's) iterative unfolding

The so-called Bayesian unfolding differs from the bin-to-bin unfolding in that it scales all the bins in a single pass, so the correlations between the different bins, as well as migrations, is better described. It is named after the Bayesian theorem for the conditional probability, which in case of cross-section unfolding can be presented as

$$P(C_i|E) = \frac{P(E|C_i)\,P(C_i)}{\sum\limits_l P(E|C_l)\,P(C_l)} \tag{11.11}$$

where C_i and E are the *cause* and *effect*, where the effect would be an observed event reconstructed within certain bin, and the causes are the true events that happen in the certain bin. $P(C_i)$ is then the initial probability of the event to happen within the certain bin, and $P(E|C_i)$ is the conditional probability of said event to produce the effect (reconstructed particles). The formula may appear useless, as the initial probabilities $P(C_i)$ that participate in it are actually the very thing we are trying to calculate. But as it was found, the values can be derived with the increasing number of observations, provided no assumptions were made on the values a priori. This iterative method of unfolding was developed by G. D'Agostini in 1995 [106] and was since widely used by many experiments. The conditional probabilities $P(E|C_i)$ can be derived from MC simulations, and are constant throughout the observations (iterations). The different types of MC generators, though, can provide different values for those probabilities, and hence must be used to determine the boundaries of systematic uncertainties.

To describe the unfolding method, lets assume $n(E)$ the number of observed events with the effect E, and

$$\hat{n}(C_i) = n(E)\,P(C_i|E) \tag{11.12}$$

is the true number of events with the cause C_i that caused this effect. Since every cause C_i can have several effects E_j, and the Bayesian formula holds for each of them, the probability $P(C_i|E_j)$ can be calculated as

$$P(C_i|E_j) = \frac{P(E_j|C_i)\,P_0(C_i)}{\sum\limits_l P(E_j|C_l)\,P_0(C_l)}\,. \tag{11.13}$$

Here the initial probability $P(C_i)$ was replaced with $P_0(C_i)$ to emphasize on the iterative nature of the method, which will be discussed later. Also it can be noted that $\sum_i P_0(C_i) = 1$ by definition, and $\sum_i P(C_i|E_j) = 1$ meaning that each effect must be produced by some cause. On the other hand, $\sum_j P(E_j|C_i)$ can be less than one, because a cause may produce no effect whatsoever, and hence this sum shows the efficiency of detecting the cause C_i in any possible effect

$$\epsilon_i = \sum_j P(E_j|C_i)\,. \tag{11.14}$$

With this, the true number of events can be estimated as

$$\hat{n}(C_i) = \frac{1}{\epsilon_i}\sum_j n(E_j)\,P(C_i|E_j) \quad \epsilon_i \neq 0\,, \quad \hat{N}_{\text{true}} = \sum_i \hat{n}(C_i) \tag{11.15}$$

where $P(C_i|E_j)$ is calculated from Eq. (11.13). From here, the values for the unfolding matrix can be calculated as

$$P(C_i) = \frac{\hat{n}(C_i)}{\hat{N}_{\text{true}}}\,. \tag{11.16}$$

The iterative unfolding procedure then goes as follows:

1. Pick an initial unbiased $P(C_i)$ distribution from the best knowledge of the unfolded process so that $n(C_i) = P(C_i)\,N_{\text{obs}}$. The uniform distribution can also work.
2. Calculate the next iteration of $\hat{n}(C_i)$ and $P(C_i)$ based on the previous distribution.
3. Make a χ^2 comparison between $\hat{n}(C_i)$ distributions before and after the iteration.
4. If χ^2 is not satisfactory, repeat from step 2.

The optimal number of the iterations depends on the statistical errors of the initial data. With infinite statistics, the number of iteration is not restricted by anything, and sufficiently big number of iteration will produce the true distribution with any precision. But for finite number of events, the number of iteration should be relatively small, as in the extreme case of infinite iterations, the resulting unfolding matrix equals to the inverted detector response matrix, which defies the whole purpose of the Bayesian method. But because of the quick convergence, even the first iteration results in the distribution which is close to the true. Usually, two to three iterations are chosen for the data unfolding.

For the uncertainty propagation the ToyMC method is used (see Section 9.6).

11.3 Combination of the several cross-sections

When calculating the cross-section for $Z \to \ell\ell$ decay, there are several independent channels from which the data is acquired. And the results produced from different sources overlap in some parts of the kinematic space. In theory, the calculated cross-section should be the same for all channels, but since the results come with uncertainties, it is not always the case. Let's assume that some value was measured as μ with the uncertainty of Δ. Assuming that the uncertainty is gaussianely shaped, the probability distribution for the true value m can be written as

$$P(m) = \frac{1}{\sqrt{2\pi}\Delta} \exp\left(-\frac{(m-\mu)^2}{2\Delta^2}\right) , \tag{11.17}$$

and the corresponding χ^2 function would be

$$\chi^2(m) = \frac{(m-\mu)^2}{\Delta^2} . \tag{11.18}$$

When there are several measurements of the same true value (μ_1, Δ_1), (μ_2, Δ_2) and so on, the combined probability function will be

$$P_{\text{comb}}(m) \sim \exp\left(-\frac{(m-\mu_1)^2}{2\Delta_1^2}\right) \cdot \exp\left(-\frac{(m-\mu_2)^2}{2\Delta_2^2}\right) \cdot ... \tag{11.19}$$

with the combined χ^2 being the sum if the individual ones $\chi^2_{\text{sum}} = \chi^2_1 + \chi^2_2 + ...$ So if we are to replace the multitude of measurements with a single average one, we are to rewrite the combined χ^2 in the form of

$$\chi^2_{\text{comb}}(m) = \frac{(m-\mu_{\text{ave}})^2}{\Delta^2_{\text{ave}}} + \chi^2_0 , \tag{11.20}$$

where μ_{ave}, Δ_{ave} and χ^2_0 can be found from

$$\mu_{\text{ave}} = \arg\min_m \chi^2_{\text{sum}}(m)\ , \ \ \chi^2_0 = \chi^2_{\text{sum}}(\mu_{\text{ave}})\ , \ \ \Delta_{\text{ave}} : \chi^2_{\text{sum}}(\mu_{\text{ave}} \pm \Delta_{\text{ave}}) = \chi^2_0 + 1\,. \tag{11.21}$$

The χ^2_0 shows the consistency of measurements, and for measurements to be consistent the relation $\chi^2_0/N_{\text{DoF}} \approx 1$ must hold true.

The same technique applies in case of measurements made in several bins, but only if the bins are fully independent, i.e. the uncertainties are fully uncorrelated. In case of the uncertainties correlated between bins, the calculation of the combined values becomes more complex. The systematic uncertainties also can be regarded as a results of experiments, and as such have a true and measured values and an uncertainty of its own with a similar relation $\chi^2_{\text{syst}} = (\alpha - \alpha_0)^2/\Delta^2_\alpha$. While we usually are unable to calculate α and Δ_α, it is not needed, since the covariance matrix decomposition which we do during the systematic uncertainty unfolding provide us with the nuisance parameters $b_s = (\alpha_s - \alpha_{0,s})/\Delta_{\alpha,s}$. With this in mind, the equation for χ^2 would look like

$$\chi^2(m, \vec{b}) = \sum_i \frac{\left(m - \mu_i - \sum_s \Gamma^s_i b_s\right)^2}{\Delta^2_i} + \sum_s b^2_s\,, \tag{11.22}$$

where i runs over all the combined measurements and s runs over all the sources of the correlated systematic uncertainties, $\vec{b}$ is composed of the nuisance parameters b_s, Δ_i is an uncorrelated and $\Gamma_{s,i}$ is correlated uncertainties.

For the combination of the several measurements with the same binning the combined χ^2 is not equal to direct sum of the individual ones, since all the measurements usually share some sources of the systematic uncertainties, so the instead of a direct sum, the χ^2_{sum} would look as such

$$\chi^2_{\text{sum}}(\vec{m}, \vec{b}) = \sum_k \sum_i \frac{\left(m_k - \mu_{k,i} - \sum_s \Gamma^s_{k,i} b_s\right)^2}{\Delta^2_{k,i}} W_{k,i} + \sum_s b^2_s\,, \tag{11.23}$$

where k runs over all bins, s runs over all sources of the systematic uncertainties for all measurements, and m_k substitute $\vec{m}$. $W_{k,i}$ is equal to 1 if the measurement i contributes to the bin k, and 0 otherwise. If the source k is insensitive to the source s of the systematic uncertainty, then Γ^s_k is equal to 0. The multibinned version of the combined χ^2_{comb} is constructed the same way as before

$$\begin{aligned}\chi^2_{\text{comb}}(\vec{m}, \vec{b}) = \sum_k \frac{\left(m_k - \mu_{k,\text{ave}} - \sum_s \Gamma^s_{k,\text{ave}}(b_s - b_{s,\text{ave}})\right)^2}{\Delta^2_{k,\text{ave}}} \\ + \sum_{k_1}\sum_{k_2}(b_{k_1} - b_{s,\text{ave}})(b_{k_2} - b_{s,\text{ave}})(A'_S)_{k_1 k_2} + \chi^2_0\,.\end{aligned} \tag{11.24}$$

The values $\vec{\mu}_{\text{ave}}$, $\vec{b}_{\text{ave}}$ and the matrix A'_S can be found from the minimization of the Eq. (11.23) with respect to the variables m_k and b_s, which can be expressed in the form of partial derivatives

$\partial\chi^2_{\mathrm{sum}}/\partial m_k = 0$, $\partial\chi^2_{\mathrm{sum}}/\partial b_s = 0$ or in the matrix form

$$\begin{pmatrix} A_M & A_{SM} \\ (A_{SM})^T & A_S \end{pmatrix} \begin{pmatrix} \vec{\mu}_{\mathrm{ave}} \\ \vec{b}_{\mathrm{ave}} \end{pmatrix} = \begin{pmatrix} \vec{c}_M \\ \vec{c}_S \end{pmatrix} , \tag{11.25}$$

where

- $A_M = \operatorname*{diag}_k \left(\sum\limits_i \frac{W_{k,i}}{\Delta^2_{k,i}} \right)$
- $A^{ks}_{SM} = -\sum\limits_i \frac{\Gamma^s_{k,i}}{\Delta^2_{k,i}} W_{k,i}$
- $A^{s_1 s_2}_S = \delta_{s_1 s_2} + \sum\limits_k \sum\limits_i \frac{\Gamma^{s1}_{k,i}\Gamma^{s2}_{k,i}}{\Delta^2_{k,i}} W_{k,i}$
- $c^k_M = \sum\limits_i \frac{\mu_{k,i}}{\Delta^2_{k,i}} W_{k,i}$
- $c^s_S = -\sum\limits_k \sum\limits_i \frac{\mu_{k,i}\Gamma^s_{k,i}}{\Delta^2_{k,i}} W_{k,i}$

In all of the above i runs over all measurements, k runs over all bins and s runs over all the systematic uncertainty sources. The final values for the combined results can thus be found as

$$\begin{aligned} A'_S &= A_S - (A_{SM})^T A^{-1}_M A_S M \\ \vec{b}_{\mathrm{ave}} &= (A'_S)^{-1} \left(\vec{c}_S - (A_{SM})^T A^{-1}_M \vec{c}_M \right) \\ \vec{\mu}_{\mathrm{ave}} &= A^{-1}_M \left(\vec{c}_M - A_{SM} \vec{b}_{\mathrm{ave}} \right) . \end{aligned} \tag{11.26}$$

The values for the statistical and uncorrelated systematical uncertainty can be found as

$$\Delta^2_{k,\mathrm{ave}} = \frac{1}{A^{kk}_M} = \frac{1}{\sum\limits_i \frac{W_{k,i}}{\Delta^2_{k,i}}} . \tag{11.27}$$

CHAPTER 12

Efficiency calculations

The reconstruction steps described in the Section 8 are not absolutely effective. The algorithms occasionally misinterpret particles and thus introduce the errors in the results. This margin of error is called the efficiency, and it is present for reconstructing both collision and MC samples. But to be able to compare collision data to theoretical predictions, the efficiency in both cases should be the same, which is not the case. To remedy this, the so-called "efficiency correction factors" were introduces for every step of the reconstruction chain: for trigger efficiency ($\varepsilon_{\mathrm{TG}}$), reconstruction efficiency ($\varepsilon_{\mathrm{Reco}}$), identification efficiency ($\varepsilon_{\mathrm{ID}}$), and isolation efficiency ($\varepsilon_{\mathrm{ISO}}$). The correction factor for every efficiency is defined as a ratio $\varepsilon^{\mathrm{data}}/\varepsilon^{\mathrm{MC}}$.

All efficiencies are measured using the tag-and-probe method, which require two electrons, one of which should pass the tight identification and would be called "tag", and the other should pass the weak identification and would be called "probe". If the "probe" also passes the tight identification, it is called "passing probe", and it is called "failing probe". The efficiency is then calculated as a ratio of the passing probes to the whole amount of tags, and is usually calculated in 2D binning of $|\eta|$ and p_{T}.

In the following sections all the efficiencies would be discussed separately.

12.1 Trigger efficiency

The efficiency of the electron triggers was determined with the help of the $Z \to ee$ data which gives a clear selection of electrons with wide range in both p_{T} and η. For the central-forward analysis one uses a single-electron trigger, but since we need two electrons for the tag-and-probe method, the trigger efficiency was calculated using the central-central $Z \to ee$ data. To get that data, the usual $Z \to ee$ CC cut chain was applied, but with identification (ID) and isolation (ISO) cuts being changed to that, required from the central electrons from the $Z \to ee$ CF and $W \to e\nu$ analyses. After that every electron was consecutively used as a "tag" and as a "probe", with the "tag" always being required to be matched to the single-electron trigger, and the efficiency of a successful match of the "probe" to the same trigger being evaluated.

The scale factors were calculated in three different mass windows of $70 \leq m_{ee} \leq 110$ GeV, $80 \leq m_{ee} \leq 100$ GeV, and $85 \leq m_{ee} \leq 95$ GeV, to vary the background level. The results from the middle mass window were used to define the central value of the scale factors, while the

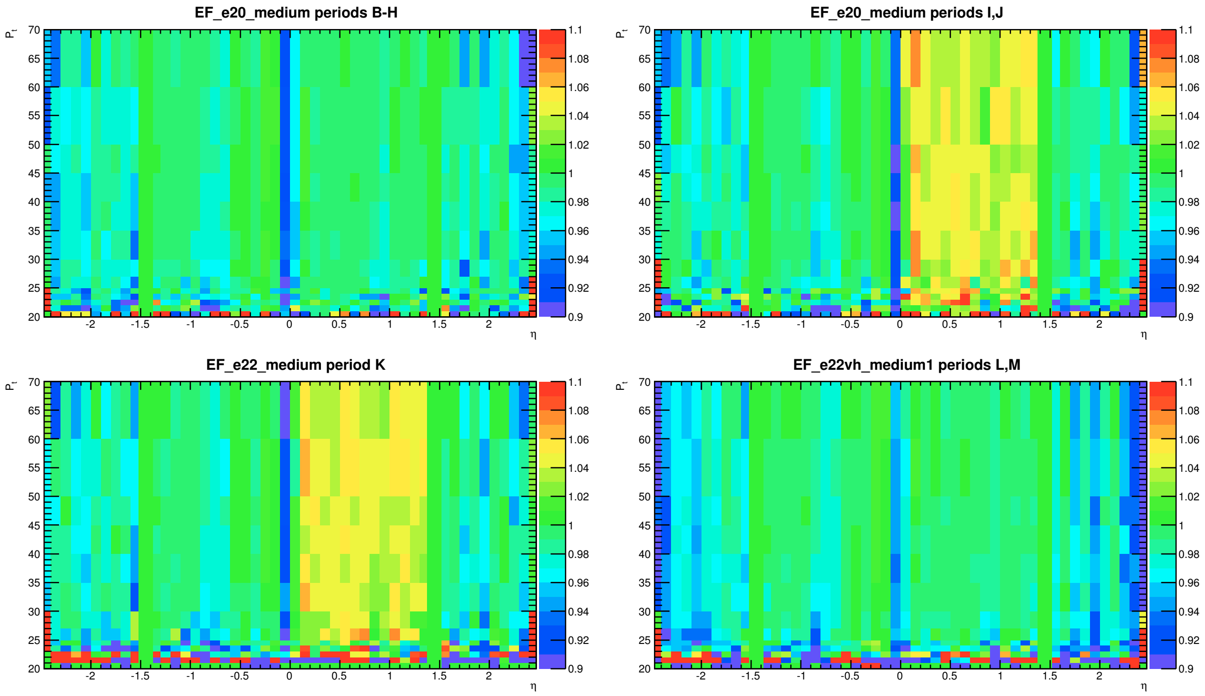

Figure 12.1: Scale factors for the default single-electron triggers used in the 2011 data. The plots were made using the $Z \to ee$ MC samples with standard CC analysis cuts with the additional requirements on electron ID and ISO from the CF analysis.

other two were used to derive a source of uncertainty. To evaluate the uncertainty further, a background subtraction via OS-SS pairs (opposite sign minus same sign) was performed. The central value was taken from the OS pairs and the full difference to the OS-SS sample was taken as another source of uncertainty.

The whole MC sample was divided into four periods, corresponding to data periods B-H, I-J, K and L-M. Each of these MC periods is distinguishable by its unique LAr calorimeter and trigger setups, and should be used separately in order to calculate the scale factors which are valid only for that particular period. After propagation to the final cross section measurement using the combined ToyMC method (see Section 9.6), the resulting uncertainty is typically 0.1% only.

The calculated trigger efficiencies as function of p_T and η for the default single-electron triggers used in the analysis are presented in Figure 12.1.

12.2 Reconstruction and identification efficiency

There are three separate efficiencies that contribute to the electron identification: the efficiency of the cluster reconstruction algorithm, the efficiency of the electron reconstruction algorithm, and the efficiency of the electron identification algorithm. Every subsequent algorithm only works if its predecessors succeeded, so all the three efficiencies are tied together, and may be explored together.

12.2.1 Central electron identification efficiencies

For the central electrons, the samples from the $Z \to ee$, $W \to e\nu$, and $J/\psi \to ee$ were taken in the kinematic intervals of $7 < E_{\mathrm{T}} < 50$ GeV and $|\eta| < 2.47$ [100]. The efficiencies and uncertainties were calculated separately for each channel, and then combined for the calculation of the scale factors to reduce the uncertainties. For all three channels the selection for the tag electron required it to be reconstructed inside the $|\eta| < 2.47$ range with at least six hits in the SCT and at least one hit in the pixel detector. Tight selection criteria are applied to the tag object, which is an electron in case of $Z \to ee$ and $J/\psi \to ee$ events, and is a E_{T}^{miss} in case of $W \to e\nu$. To further decrease the amount of background, additional cuts were applied to each channel separately.

For the $W \to e\nu$ channel the selection was tighten for the lower-mass events, i.e. the ones with the transverse energy $40 < E_{\mathrm{T}} < 50$ GeV and missing transverse energy $25 < E_{\mathrm{T}}^{miss} < 40$ GeV. For the tighter selection, the probe electron was required a $p_{\mathrm{T}} > 15$ GeV, and the event was discarded if more then one electron candidate satisfied the medium ID criteria. To reduce the amount of hadrons misidentified as electrons, two additional isolation criteria were added: the probe electron should be separated from any jet with $p_{\mathrm{T}} > 25$ GeV with a cone of at least $\Delta R > 0.4$, and similarly the E_{T}^{miss} vector should be separated from any jet with the same energy by the angular distance of at least $\Delta\varphi > 0.7$.

For the $Z \to ee$ channel the additional criteria included the $E_{\mathrm{T}} > 20$ GeV cut for the tag electron, as well as exclusion of the transition region $1.37 < |\eta| < 1.52$, and similar to isolation requirement for the probe electron from the $W \to e\nu$channel: no jets with $p_{\mathrm{T}} > 25$ GeV within the $\Delta R < 0.4$ cone. The OS cut was required for the selection, but the SS events were also counted for the OS-SS background substraction the same way as in the trigger efficiencies calculation. The mass window was tighten to $80 < m_{ee} < 100$ GeV to further suppress the background.

For the $J/\psi \to ee$ channel the additional filtering was very high due to more difficult reconstruction of the low E_{T} events. There are two types of events in this channel: prompt and non-prompt. The event is called prompt when it happens in the vicinity of the primary vertex, while the non-prompt J/ψ particles are displaced from the main vertex due to the relatively long lifetime of its parent b-hadron. The non-prompt events are usually surrounded by the hadronic activity which complicates the task of proper identification even further. To remedy this the events are split in two parts based on the lifetime of the J/ψ parent particle derived from the transverse shift of the event vertex from the primary vertex, with events with longer lifetime being non-prompt. The additional restriction are also put on the tag electron, which requires additional TRT hits and large isolation cones.

For the evaluation of the remaining amount of background, the discriminating variables are used for each of the channels. For $W \to e\nu$ the discriminating variable is the isolation: the sum of all energies from both electromagnetic and hadronic calorimeters is calculated for the cone around the probe electron, excluding the energy from the electron itself. The resulting quantity is then referred as $E_{\mathrm{T}}^{cone}(X)/E_{\mathrm{T}}$ where X is ΔR of the cone, usually 0.3. The background template is constructed by reversing the two criteria of the electron id: TRT

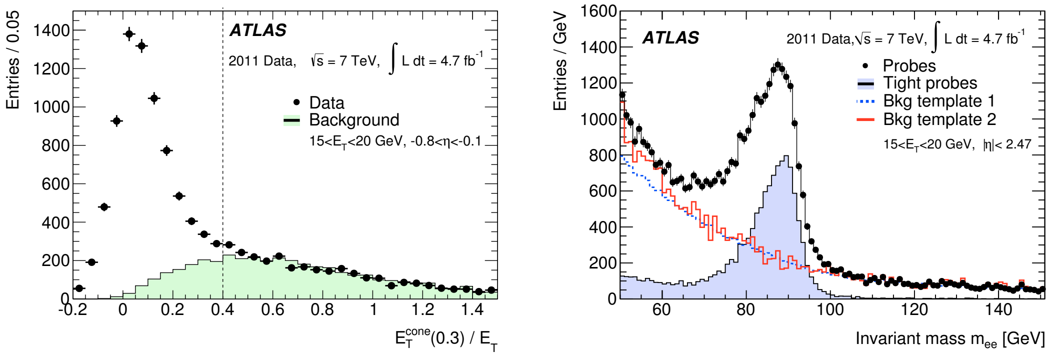

(a) $W \to e\nu$ (b) $Z \to ee$

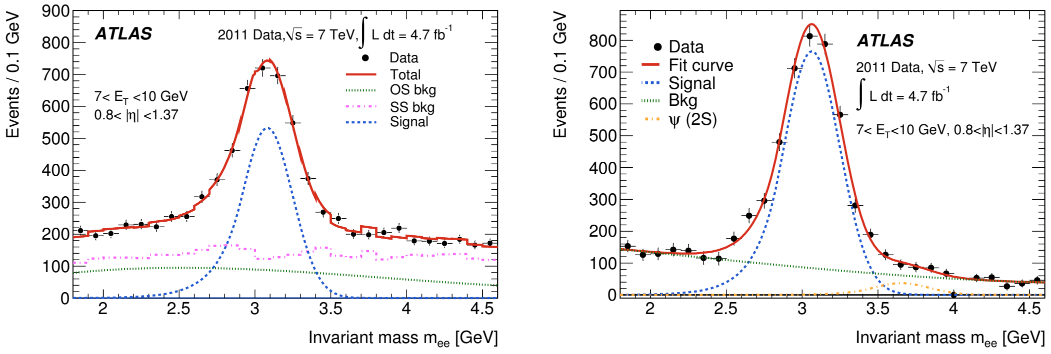

(c) $J/\psi \to ee$ prompt (d) $J/\psi \to ee$ non-prompt

Figure 12.2: Background estimation for different channels. (a) shows the $E_{\mathrm{T}}^{cone}(0.3)/E_{\mathrm{T}}$ variable of $W \to e\nu$ events for probes (black dots) and normalized background template. The black dashed line shows the threshold. (b) shows two normalized background templates for $Z \to ee$, see text for details. (c) and (d) show backgrounds for short-lifetime (prompt) and long-lifetime (non-prompt) $J/\psi \to ee$ events respectively, being decomposed to various components. [100]

high-threshold fraction from the tight ID, and the total shower width from the loose ID. The discriminating variable is used to determine which bins are more signal-dominated, and which are background-dominated (located below and above the threshold respectively), and then the template is fitted to data for the background-dominated bins, and scaled respectively for the signal-dominated ones. For the $Z \to ee$ events there are two discriminating variables, and thus two background templates available. The first one is the m_{ee} mass window, where the template is constructed from the events failing at least two loose ID cuts and with a significant amount of energy in a cone around the probe. The template is fitted to data in the high-energy mass window $m_{ee} > 120$ GeV. The second template is the same as for the $W \to e\nu$ events. For the $J/\psi \to ee$ channel the same mass window is used as for $Z \to ee$ channel. The template is constructed mainly from the same sign events with some additions made with Chebyshev polynomials.

For the uncertainties calculation, the shifting of various parameters is applied to all channels and the resulting shift in the efficiencies is observed. For the $W \to e\nu$ events the thresholds for the E_{T}^{miss} and m_t cuts are shifted, and the width of the cone for the discriminating variable is alternated to 0.4. For the resulting ∼80 samples the backgrounds are then evaluated using the same method, and the resulting spread of the efficiencies is calculated. For the samples used the signal/background ratio distribution in the signal region exhibits an RMS (Root Mean Square) of 30% at low E_{T} (15-20 GeV) and 25% at high E_{T} (35-40 GeV). For the $Z \to ee$ events the different mass-windows is used along with some alternative criteria for the tag electron. Both background templates are used, and in case of the isolation template the radius of the cone is also shifted, which gives in total about 120 samples. The S/B ratio distribution exhibits an RMS around 10%. For the $J/\psi \to ee$ channel the isolation criteria was shifted for the tag electron as well as the high TRT requirement. The varying mass window and the same sign cut are also used to produce a total of 76 and 52 samples for prompt and non-prompt events respectively, with RMS around 30%.

Since the events are statistically independent, their combination is used to produce the final results. Since it is data-to-MC ratio (which are scale factors, SFs) we are interested in, we can disregard the effects of the resolution or bin migration, since it will affect both data and MC similarly, and won't change the ratio. A global χ^2 minimization was used to calculate the SF for every particular bin, in 2D p_{T}-η binning. The formula for each bin is as follows:

$$\chi^2 = \sum_{i,k} \frac{\left[\mu^{i,k} - \mathrm{SF}^i - \sum_j \gamma_j^{i,k} \mathrm{SF}^i b_j\right]}{\left(\delta_{\mathrm{sta}}^{i,k}\right)^2 \mu^{i,k} \mathrm{SF}^i \left(1 - \sum_j \gamma_j^{i,k} b_j\right) + \left(\delta_{\mathrm{unc}}^{i,k} \mathrm{SF}^i\right)^2} + \sum_j b_j^2 \,, \qquad (12.1)$$

where i, k, and j run over the (E_{T}, η) bins, the three channels, and the correlated systematics, respectively. The variables $\delta_{\mathrm{sta}}^{i,k}$, $delta_{\mathrm{unc}}^{i,k}$, and $\gamma_j^{i,k}$ represent the relative statistical, uncorrelated, and correlated systematic uncertainties respectively. The nuisance parameters b_j are related to correlated uncertainties, which are dominated by the background subtraction uncertainties. The combined scale factors are given by SF^i. The resulting scale factors for some bins are shown in Figure 12.3.

12.2.2 Forward electron identification efficiencies

In the forward region of the calorimeters, the electron identification efficiency is measured with a $Z \to ee$ central-forward sample where a well-isolated $E_{\mathrm{T}} > 25$ GeV tag electron satisfying the tight requirement is identified in the central region of the calorimeter and the probe cluster with $E_{\mathrm{T}} > 20$ GeV is found in the forward region. As an additional cut the low E_{T}^{miss} is required for the event candidates to suppress the contributions from $W \to e\nu$ events. The invariant mass m_{ee} is fitted by the Crystal Ball function convoluted with a non-relativistic Breit-Wigner function with fixed Z width to model the signal, and a Landau function to model the background in a mass window of $55 < m_{ee} < 130$ GeV. The S/B ratio is ∼7 for the outer EMEC and ∼5 for the FCAL. The various shifts to the tag requirements and to the fit parameters were performed to determine the amount of the systematical uncertainties, the resulting scale factors for selected bins can be seen in Figure 12.4.

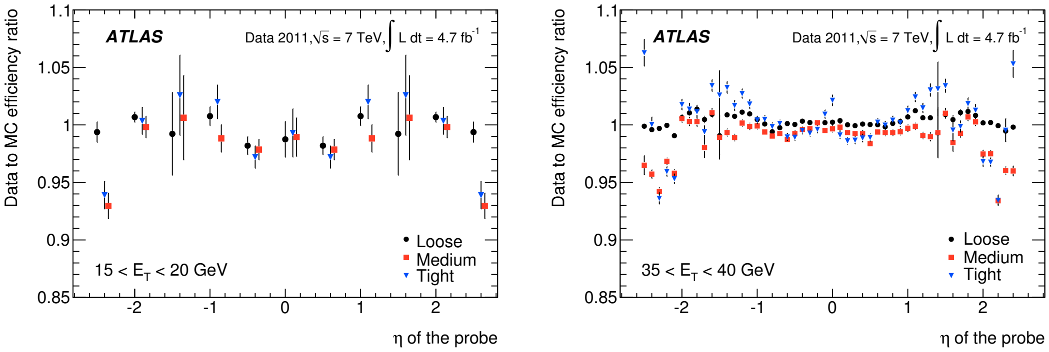

(a) $15 < E_{\mathrm{T}} < 20$

(b) $35 < E_{\mathrm{T}} < 40$

Figure 12.3: Examples of combined scale factors for the three identification criteria (loose, medium, tight) as a function of the pseudorapidity of the probe-electron η. Results are shown for different ranges of the probe electron energy. The error bars indicate the total uncertainties. [100]

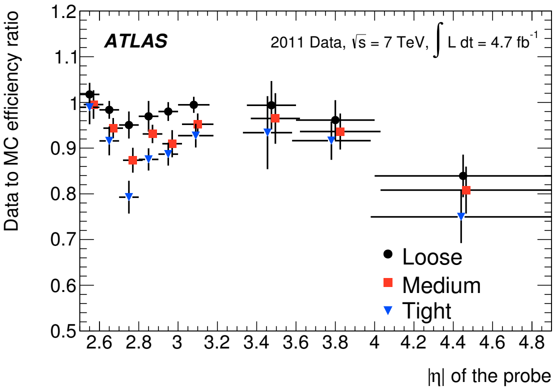

Figure 12.4: The scale factors for the forward electrons with $E_{\mathrm{T}} > 20$ GeV. The error bars correspond to the total uncertainties. [100]

12.2.3 Reconstruction efficiencies

For reconstruction efficiency measurements the events from the $Z \to ee$ channel are used for both central and forward electrons. As discussed in Section 8.1 the algorithm for the forward electrons is much more complex and gives an efficiency of about 97% at 7 GeV and ∼99% at 15 GeV. For the higher energies the efficiency of it is matched by that of the track reconstruction and cluster-track matching algorithms.

Efficiency values were measured for three samples:

- All reconstructed electron candidates in $Z \to ee$ channel;
- All the same electron candidates, but with additional requirement of the quality of the matching track, to match with the $J/\psi \to ee$ conditions described above;
- All reconstructed electron candidates with additional requirements on hadronic leakage and the track quality to match with the $W \to e\nu$ conditions described above.

The conditions for these measures follows that of the identification closely, except for the corrections for the photon conversions: the photons are included in the denominator when calculating the efficiency, provided they satisfy all the requirements. Naturally, that also means that the opposite sign requirement also doesn't apply.

For the background evaluation the same technique is applied: the background template is constructed using the inversion of several ID cuts (at least two from the loose ID not counting the ones dealing with the track) and failing the isolation requirement, and then normalized to the data in the high-mass region ($110 < m_{ee} < 250$ GeV).

The three samples together with the variations obtained from the variations of the background thresholds are used to find the systematic uncertainties with the same method as used in the identification efficiency calculation.

The resulting efficiencies can be seen in Figure 12.5. It can be seen that the systematical error increases greatly at $E_{\mathrm{T}} < 20$ GeV.

12.3 Isolation efficiency

In the central-forward event selection of $Z \to ee$ analysis the two additional isolation cuts are used in order to reduce the amount of the background: Iso98$E_{\mathrm{T}}{}^{\mathrm{cone20}}$ and Iso97$p_{\mathrm{T}}{}^{\mathrm{cone40}}$ one being for the track and the other for the cluster. The efficiency of the isolation is thus the fraction of the electrons that pass this additional cut:

$$\varepsilon_{\mathrm{Iso}} = \frac{N_{\text{probe with Iso}}}{N_{\text{all probe}}}, \quad \delta\varepsilon_{\mathrm{Iso}} = \frac{\sqrt{(1-2\varepsilon)\delta N^2_{\text{probe with Iso}} + \varepsilon^2 \delta N^2_{\text{all probe}}}}{N_{\text{all probe}}}, \tag{12.2}$$

where $\varepsilon_{\mathrm{Iso}}$ is the efficiency, and $\delta\varepsilon_{\mathrm{Iso}}$ is the corresponding statistical error.

The measurement was done with the $Z \to ee$ sample with the same setup, with the p_{T} cut of the probe electron being lowered to 15 GeV and mass window reduced to $80 < m_{ee} < 100$ GeV to remedy the increased background. The remaining background is negligible (less than 0.1%).

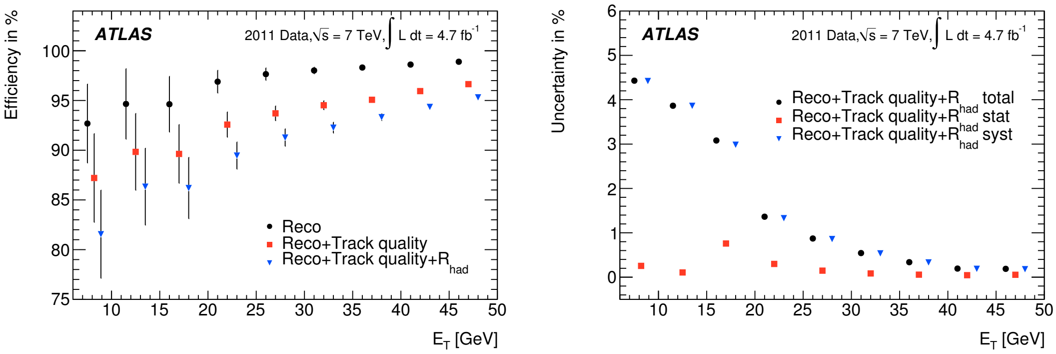

(a) Reconstruction efficiencies

(b) Systematical and statistical uncertainties

Figure 12.5: Reconstruction efficiencies for the central electrons, the error bars represent the total uncertainty, which can be seen fully in (b). [100]

The systematical error evaluation was done by shifting the mass window in the same way as the calculation of the trigger efficiencies, and by increasing the p_{T} cut for the tag electron to 24 GeV. The resulting efficiencies can be seen in Figure 12.6.

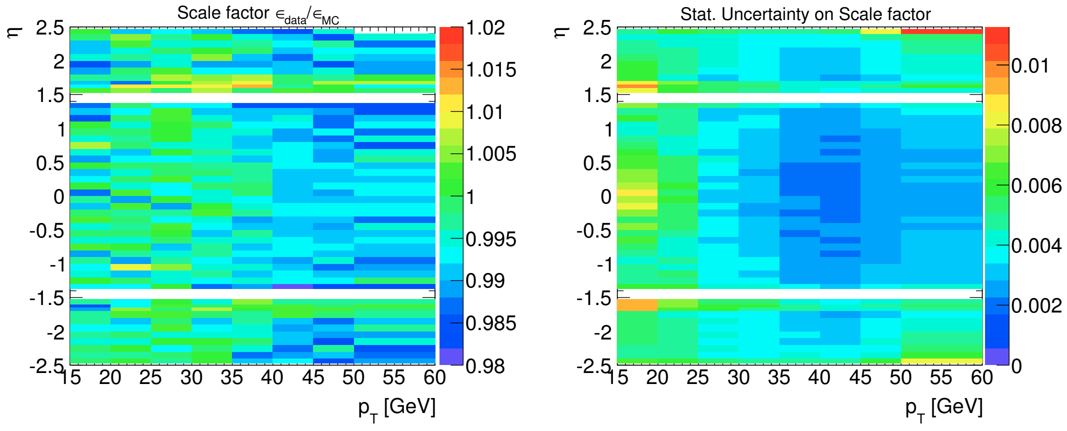

(a) Isolation scale factors

(b) Statistical uncertainties

Figure 12.6: Scale factors for the isolation efficiencies for the 2011 data together with statistical uncertainties in 2D binning by p_{T} and η. The plots were made using the $Z \rightarrow ee$ MC samples with standard CC analysis cuts with the additional requirements on electron ID from the CF analysis.

CHAPTER 13

Background estimation

As was described in Section 10, the selection phase is designed to suppress the background events (i.e. not $Z \to ee$ events) while keeping the signal events. But even with all the cuts applied, some of the background events still pass all of them. In order to get the correct results, we need to estimate the number of the background events in our selection.

The background events can be distinguished into two types: the electroweak (EW) background and the QCD background. The difference from the analysis point of view is that we can directly predict the amount of the EW background based on the MC simulation (except for two components which will be discussed later), while the QCD background we have to estimate, using so-called fits based on the indirect data. Both of these methods will be described here.

13.1 Electroweak background

The sources of the electroweak background are the events that came from various electroweak decays but were misinterpreted as $Z \to ee$. The list of the processes that contribute to the EW background was given in Tab. 6.3. There are eight of them, including three single-boson decays, three di-boson decays, $t\bar{t}$, and photon induced background. All the processes except the last one have a cross-section comparable with $Z \to ee$ which can be reliably predicted by the theory, and also use the same efficiency coefficients as signal, and therefore can be simulated using MC. For the photon-induced background the situation is more complicated. We can't reliably evaluate the amount of this background, and the relative uncertainty for it is usually 30-50%. This background is added after the unfolding.

The electroweak background is largely dominated by the $W \to e\nu$ events, where the electron goes to the central part of the calorimeter, and the fake forward electron is produced by the W+jet activity. Since the jet behavior in the forward region is modeled poorly, this background is normalized to data, instead of theoretical-driven luminocity normalization used for other backgrounds.

For the $W \to e\nu$ evaluation three selections were used, all of them in two mass windows around mass peak: $66 < m_{ee} < 80$ GeV and $100 < m_{ee} < 150$ GeV, but two of them also have an additional cuts:

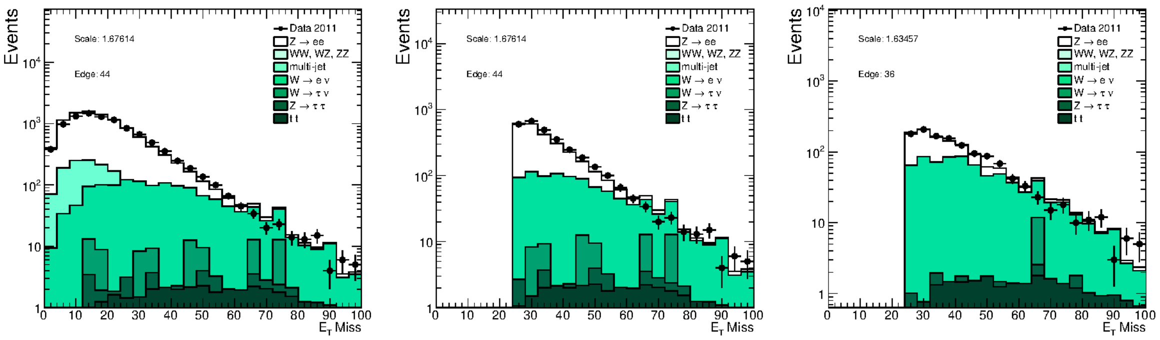

(a) Mass window

(b) Mass window, E_{T}^{miss}

(c) Mass window, E_{T}^{miss}, E_{T}

Figure 13.1: The data-fitting of the $W \to e\nu$ background with various selections. (a) Mass window selection, (b) Mass window and $E_{\mathrm{T}}^{miss} > 25$ GeV, (c) Mass window, $E_{\mathrm{T}}^{miss} > 25$ GeV and $E_{\mathrm{T}} > 50$ GeV.

y_Z bin	$t\bar{t}$	$W \to e\nu$	$W \to \tau\nu$	WW	WZ	ZZ	$Z \to \tau\tau$	$\gamma\gamma \to ee$
1.2 - 1.4	0.18	1.90	0.00	0.04	0.08	0.04	0.01	0.10
1.4 - 1.6	0.11	1.61	0.38	0.03	0.07	0.03	0.06	0.09
1.6 - 1.8	0.08	1.10	0.10	0.03	0.05	0.03	0.09	0.08
1.8 - 2.0	0.06	1.03	0.00	0.02	0.04	0.02	0.06	0.07
2.0 - 2.2	0.04	0.87	0.03	0.02	0.04	0.02	0.08	0.05
2.2 - 2.4	0.03	0.75	0.10	0.02	0.04	0.02	0.10	0.05
2.4 - 2.8	0.01	0.65	0.13	0.02	0.04	0.02	0.11	0.05
2.8 - 3.2	0.00	0.35	0.08	0.01	0.02	0.01	0.08	0.04
3.2 - 3.6	0.00	0.05	0.00	0.00	0.01	0.01	0.01	0.03

Table 13.1: Components of the electroweak background in % of selected data for $66 < m_{ee} < 116$ GeV.

- $E_{\mathrm{T}}^{miss} > 25$ GeV;
- $E_{\mathrm{T}}^{miss} > 25$ GeV, $E_{\mathrm{T}} > 50$ GeV.

These three selections were used to normalize the $W \to e\nu$ background in high bins of $E_{\mathrm{T}}^{miss} > 70$ GeV. Since both this and QCD backgrounds use the same method of fitting to data, they interfere with each-other. But since the fitting is done in different parts of the phase space, they correlate very little with each-other, and so only one additional iteration is required to obtain valid results. The fitted background can be seen in Figure 13.1.

All other electroweak backgrounds are simply scaled to the theoretically predicted luminocity-derived values. The resulting values for the electroweak background can be seen in Tab. 13.1 for the peak mass, and in Tab. 13.2 for the high mass.

y_Z bin	$t\bar{t}$	$W \to e\nu$	$W \to \tau\nu$	WW	WZ	ZZ	$Z \to \tau\tau$	$\gamma\gamma \to ee$
1.2 - 1.6	2.17	22.40	0.00	0.64	0.30	0.04	0.61	0.98
1.6 - 2.0	1.22	17.06	1.70	0.64	0.22	0.04	0.52	0.98
2.0 - 2.4	0.62	9.98	1.30	0.39	0.15	0.03	0.19	0.67
2.4 - 2.8	0.21	8.12	0.00	0.24	0.10	0.03	0.25	0.52
2.8 - 3.2	0.07	3.14	0.00	0.14	0.07	0.01	0.00	0.53
3.2 - 3.6	0.00	0.00	0.00	0.00	0.03	0.00	0.00	0.29

Table 13.2: Components of the electroweak background in % of selected data for $116 < m_{ee} < 150$ GeV.

13.2 QCD background

The QCD background is the name for the multi-jet hadronic background. Since it is nearly impossible to simulate all the multitude of the hadronic processes with even remote accuracy, the MC simulation as was used for the EW background is not an option. The shape and the amount of the QCD background should be estimated through other means. There are two methods to evaluate the shape of the multi-jet background. The first one is by using the theoretical functions. Usually the convolution of the Crystal Ball and the Breit-Wigner functions is used with the use of the RooFit framework [107]. The second method is more precise and is usually used when the data samples are large enough to provide the adequate statistical error, and consist of constructing the background template (i.e. the form) from the data itself, by using the cut inversion: several cuts in the selection chain (usually the most basic ones) are inverted to provide the sample of the background events with the most "signal-like" signature. The amount of such events is usually very limited, but the total amount of the 2011 data allows us to use this method, which is otherwise better than the theoretical predictions of the RooFit method.

In both cases, after the template (shape) is constructed, it is normalized to the data, which is basically the estimation of the background amount. This is done by using the discriminatory variable. This variable shows how much background there is in any particular bin, to distinguish background-dominated bins from the signal-dominated bins. For the $Z \to ee$ CF analysis the discriminatory variable was the isolation of the central electron cluster $E_{\mathrm{T}}^{\mathrm{cone30}}$. This variable showed the best results among the other tested, but since it is used in the default analysis selection, it can't be used directly, and the background was normalized to the selection without the isolation cuts, and then scaled accordingly.

The background template is constructed based on the three selections: the one with the default cuts, with the default cuts and relaxed track and cluster isolation, and with the default cuts and relaxed cluster isolation only. For all selection the cut inversion included some of the electron tight ID criteria. See Tab. 13.3. To calculate the systematic uncertainties for the background additional selections must be constructed. These selections must take into

	Cut inversion	Base selection	expected bkg
default	FwdTight, Tight++	Default	isolated
S_1	FwdTight, Tight++	Default w/o calo and track iso	all
S_2	FwdTight, Tight++	Default w/o calo iso	$p_{\mathrm{T}}^{\mathrm{cone}}$ isolated

Table 13.3: Event selections for QCD background estimation.

	Cut inversion	Base selection	expected bkg
default_1	Tight++	Default w/o FwdTight	isolated
S_2_1	Tight++	S_1 w/o FwdTight	all
default_2	FwdMedium++	Default w/o Tight++	isolated
S_2_2	FwdMedium++	S_1 w/o Tight++	all

Table 13.4: Event selections for QCD background systematic uncertainties calculation.

account the way the background is scaled: it is matched to the data in high-$E_{\mathrm{T}}^{\mathrm{cone30}}$ bin, and the isolation cuts are not applied. See Tab. 13.4 for the list.

The normalization procedure was made in several iterations, during which the background template and the signal MCs were scaled together to fit the data best, until the MC signal scalefactor is stabilized. Step by step explanation of the procedure is this:

- template is scaled to data based on the isolation tail bins: $s_{\mathrm{temp}} = \frac{N_{\mathrm{data}}^{\mathrm{tail}} - (s_{\mathrm{sig}} \cdot N_{\mathrm{sig.MC}}^{\mathrm{tail}} + N_{\mathrm{EWbkg}}^{\mathrm{tail}})}{N_{\mathrm{temp}}^{\mathrm{tail}}}$, where
  - s_{temp} is the scalefactor for the QCD template;
  - s_{sig} is the scalefactor for the signal MC, which is 1.0 at the first step;
  - $N_{\mathrm{data}}^{\mathrm{tail}}$ is the data events integrated over the isolation tail bins;
  - $N_{\mathrm{sig.MC}}^{\mathrm{tail}}$ is the signal MC events integrated over the isolation tail bins;
  - $N_{\mathrm{EWbkg}}^{\mathrm{tail}}$ is the electroweak background MC events integrated over the isolation tail bins;
  - $N_{\mathrm{temp}}^{\mathrm{tail}}$ is the template events integrated over the isolation tail bins;
- the scaled template (i.e. the QCD background) is subtracted from the data together with the electroweak background, and the remaining events are compared to signal MC to determine the new scalefactor for the MC: $s_{\mathrm{sig}} = \frac{N_{\mathrm{data}} - (s_{\mathrm{temp}} \cdot N_{\mathrm{temp}} + N_{\mathrm{EWbkg}})}{N_{\mathrm{sig.MC}}}$, where all the variables are the same, only integrated over all bins, not only the tail bins;
- if the new MC scalefactor differs from the previous by less then 0.1%, the template scalefactor is considered to be final, otherwise, the new iteration is made.

For the central values, the template S_1 with $E_{\mathrm{T}}^{\mathrm{cone30}}$ was chosen, as the one with the clearer separation of the background-dominated bins, and the most stable fit. On Figure 13.2 the

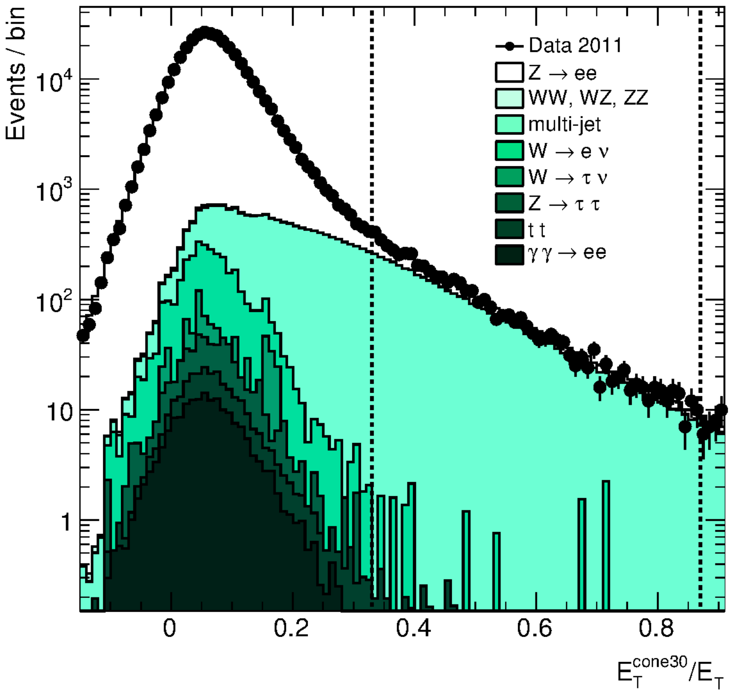

Figure 13.2: The control plot for the QCD background estimation. Dotted lines show the boundaries of the tail region for the $E_{\mathrm{T}}^{\mathrm{cone30}}/E_{\mathrm{T}}$ discriminatory variable.

distribution of the background estimation over the discriminatory variable can be seen together with the boundaries of the tail region that was used for scaling.

For the systematic uncertainties, several values were used as the threshold of the tail region. The results for peak region can be seen on Figure 13.3, where it can be seen that the estimations are consistent for a wide range of thresholds. The thresholds drawn in red were excluded from the uncertainties estimation because the χ^2/N_{DoF} for them outlaid for more than one standard deviation from the mean (as can be seen in Figure 13.4). The Figures 13.5 and 13.6 show the similar results for high-mass region.

The resulting QCD background estimations can be seen in Figure 13.7 and in Tabs. 13.5 and 13.6.

The correctness of the background estimation can be seen by the means of the control plots, in which we can compare the amount of the data events that pass all the selection cuts with the luminosity-weighted amount of signal MC together with all sources of the background combined. In Figures 13.8 and 13.9 are the control plots for electron p_{T} distributions for central and forward electrons respectively. In Figure 13.10 the control plots for electron cluster η can be seen (unlike the track η, which is available only in the central region where the tracker is present, that cluster η is available for both central and forward regions). In Figures 13.11 and 13.12 the Z boson distributions for boson rapidity and p_{T} can be seen. All the plots are provided for peak mass and high mass regions separately. And finally in Figure 13.13 the control plot for $Z \to ee$ mass-distribution can be seen. Both mass regions are presented there.

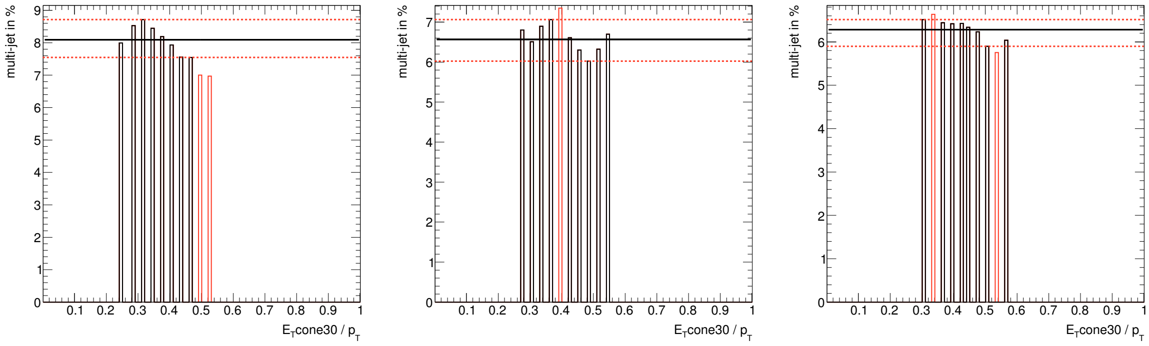

(a) $1.2 < |y_Z| < 1.4$ (b) $1.4 < |y_Z| < 1.6$ (c) $1.6 < |y_Z| < 1.8$

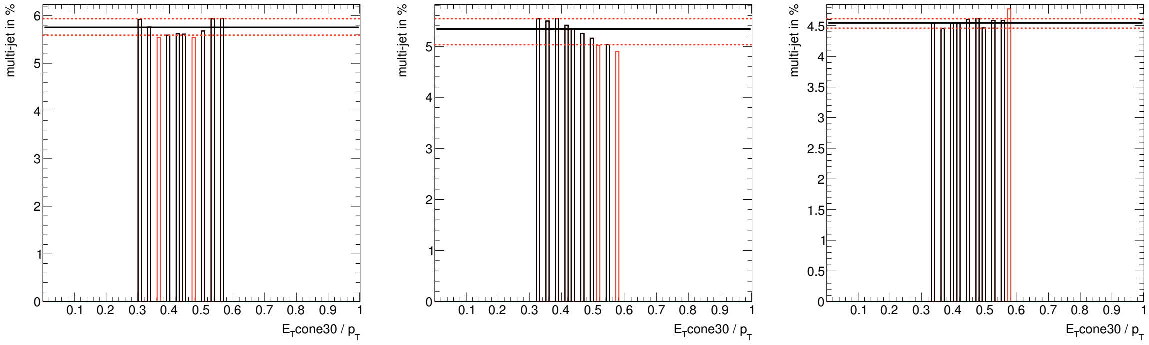

(d) $1.8 < |y_Z| < 2.0$ (e) $2.0 < |y_Z| < 2.2$ (f) $2.2 < |y_Z| < 2.4$

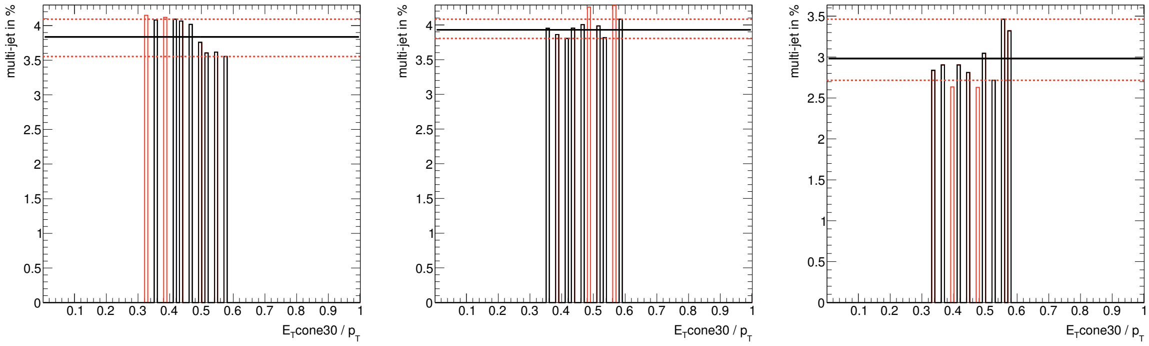

(g) $2.4 < |y_Z| < 2.8$ (h) $2.8 < |y_Z| < 3.2$ (i) $3.2 < |y_Z| < 3.6$

Figure 13.3: Comparison of the estimated amount of the QCD background in peak region for various threshold values. The estimated uncertainty is shown in red dots.

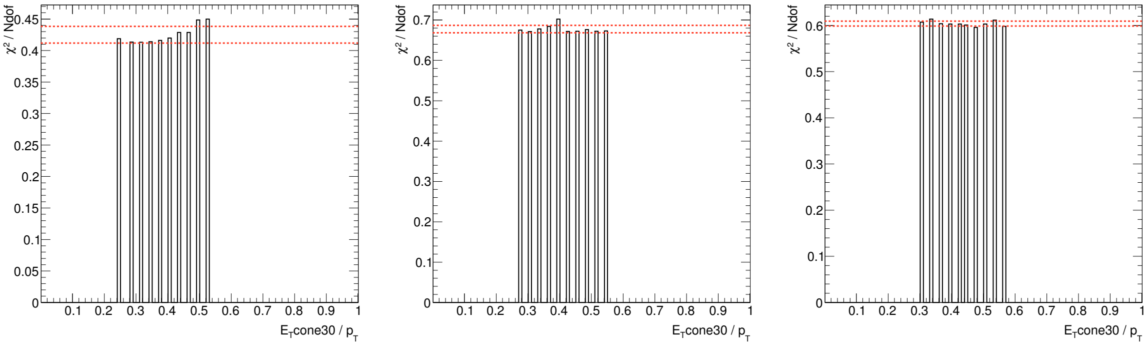

(a) $1.2 < |y_Z| < 1.4$ (b) $1.4 < |y_Z| < 1.6$ (c) $1.6 < |y_Z| < 1.8$

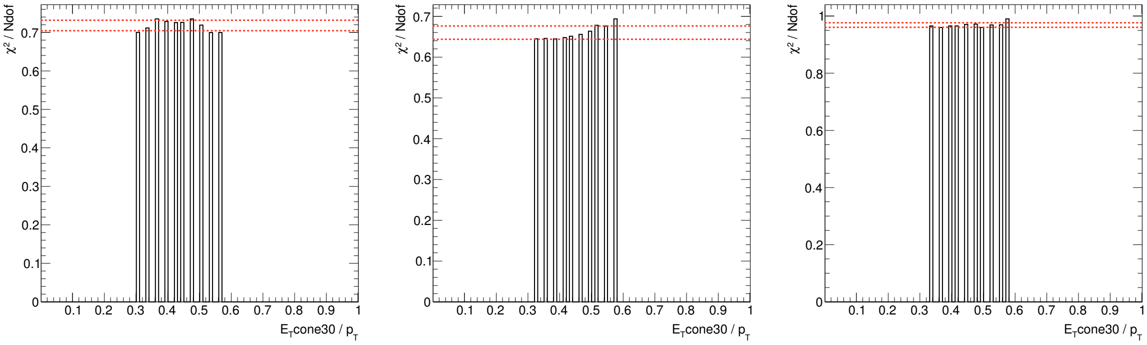

(d) $1.8 < |y_Z| < 2.0$ (e) $2.0 < |y_Z| < 2.2$ (f) $2.2 < |y_Z| < 2.4$

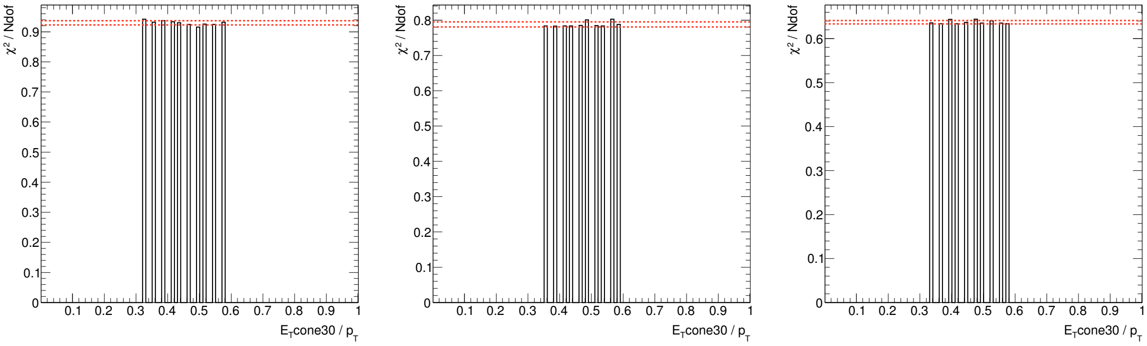

(g) $2.4 < |y_Z| < 2.8$ (h) $2.8 < |y_Z| < 3.2$ (i) $3.2 < |y_Z| < 3.6$

Figure 13.4: The χ^2/N_{DoF} values for QCD background estimates in peak region with various threshold values. The red dots show one standard deviation.

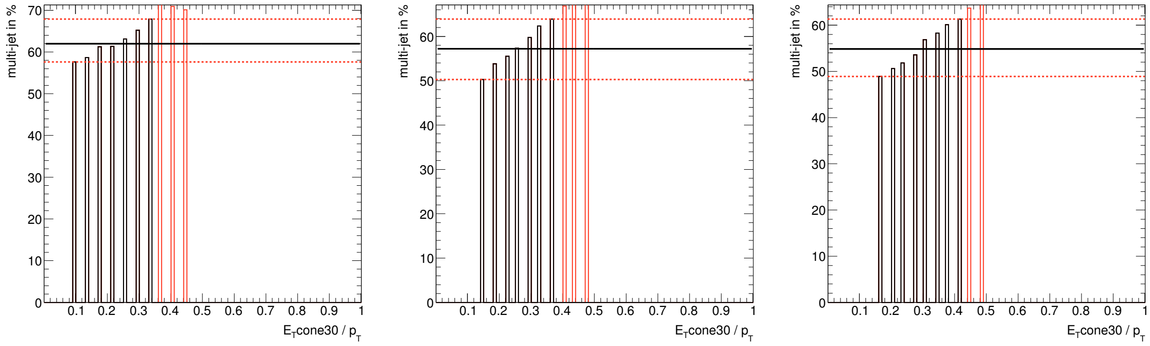

(a) $1.2 < |y_Z| < 1.6$ (b) $1.6 < |y_Z| < 2.0$ (c) $2.0 < |y_Z| < 2.4$

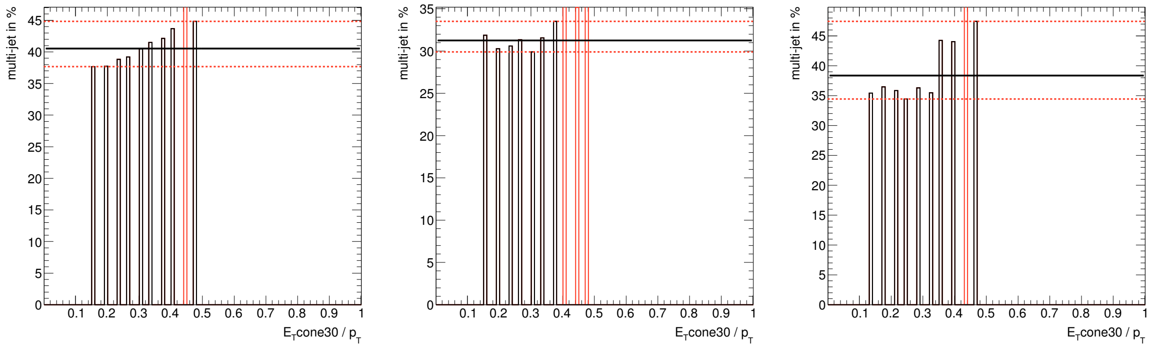

(d) $2.4 < |y_Z| < 2.8$ (e) $2.8 < |y_Z| < 3.2$ (f) $3.2 < |y_Z| < 3.6$

Figure 13.5: Comparison of the estimated amount of the QCD background in high-mass region for various threshold values. The estimated uncertainty is shown in red dots.

y_Z bin	QCD bkg	Stat	Syst
1.2 - 1.4	2.46	0.23	0.21
1.4 - 1.6	1.97	0.10	0.16
1.6 - 1.8	1.93	0.09	0.16
1.8 - 2.0	1.81	0.07	0.22
2.0 - 2.2	1.87	0.10	0.19
2.2 - 2.4	1.86	0.08	0.07
2.4 - 2.8	1.69	0.06	0.17
2.8 - 3.2	1.88	0.19	0.08
3.2 - 3.6	1.43	0.26	0.25

Table 13.5: The bin-by-bin QCD background estimation for the $Z \rightarrow ee$ CF $66 < m_{ee} < 116$ GeV analysis in percents.

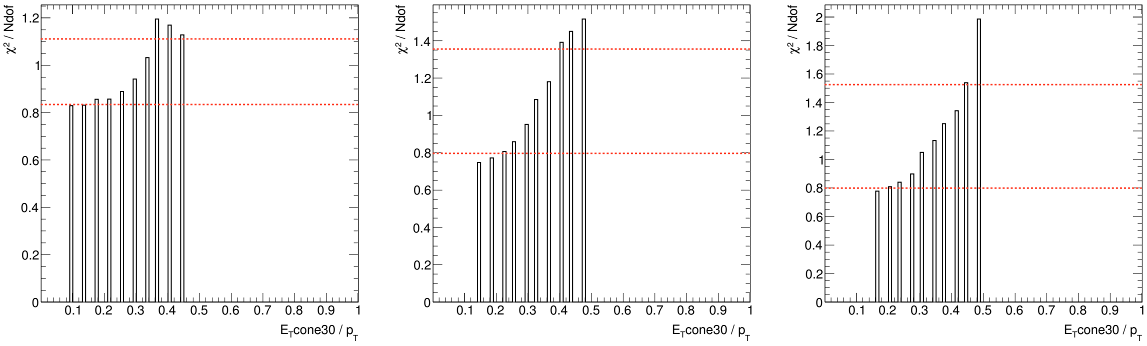

(a) $1.2 < |y_Z| < 1.6$ (b) $1.6 < |y_Z| < 2.0$ (c) $2.0 < |y_Z| < 2.4$

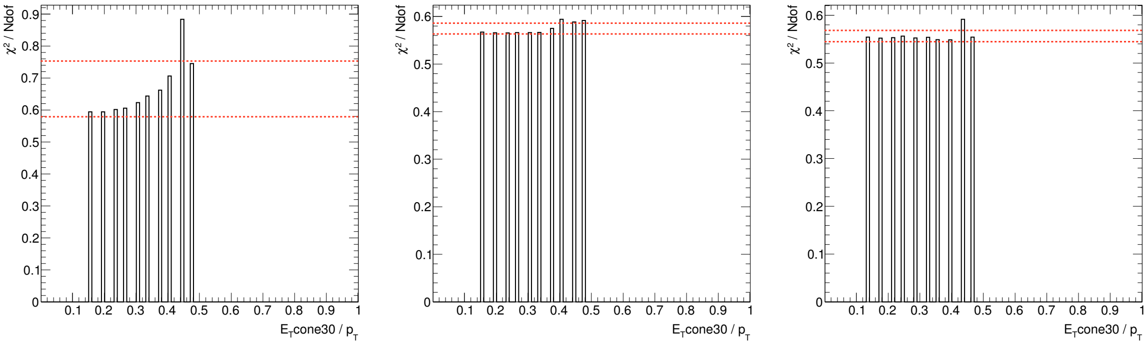

(d) $2.4 < |y_Z| < 2.8$ (e) $2.8 < |y_Z| < 3.2$ (f) $3.2 < |y_Z| < 3.6$

Figure 13.6: The χ^2/N_{DoF} values for QCD background estimates in high-mass region with various threshold values. The red dots show one standard deviation.

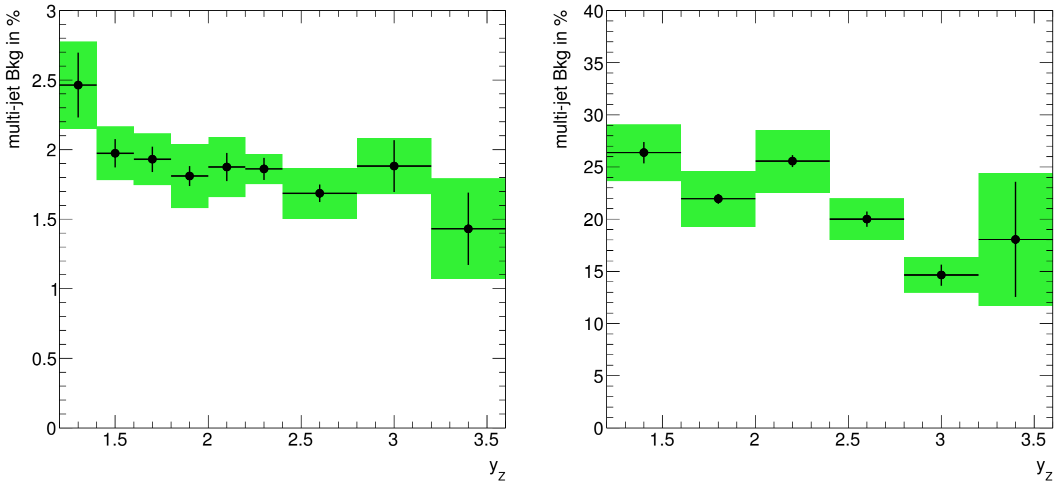

(a) $66 < m_{ee} < 116$ GeV (b) $116 < m_{ee} < 150$ GeV

Figure 13.7: The QCD background estimation for the $Z \to ee$ central-forward analysis, (a) for peak mass and (b) for high mass.

y_Z bin	QCD bkg	Stat	Syst
1.2 - 1.6	26.37	1.04	2.50
1.6 - 2.0	21.96	0.47	2.63
2.0 - 2.4	25.57	0.57	2.95
2.4 - 2.8	20.00	0.72	1.84
2.8 - 3.2	14.64	1.01	1.36
3.2 - 3.6	18.07	5.53	3.17

Table 13.6: The bin-by-bin QCD background estimation for the $Z \to ee$ CF $116 < m_{ee} < 150$ GeV analysis in percents.

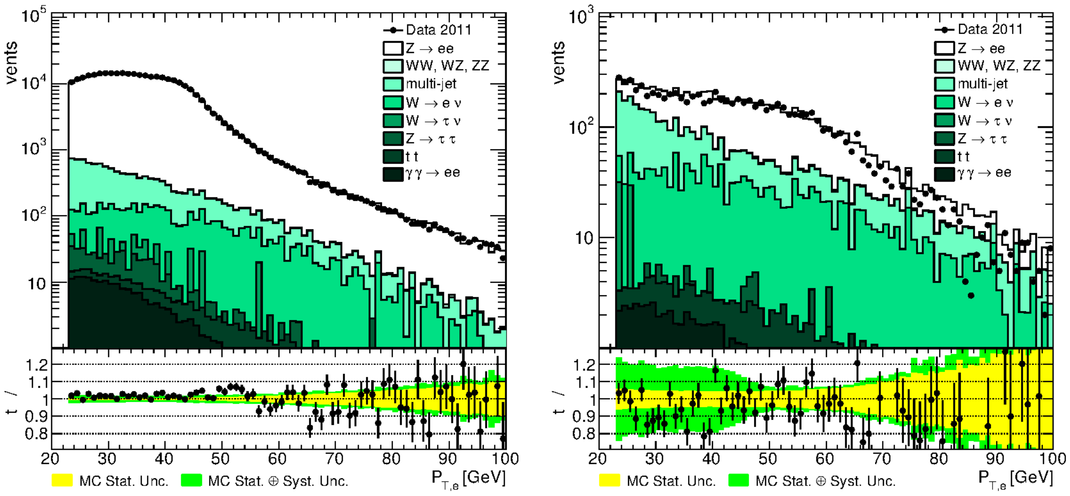

(a) Peak mass

(b) High mass

Figure 13.8: The comparison between data and MC for central electron p_{T} distribution for peak mass and high mass regions.

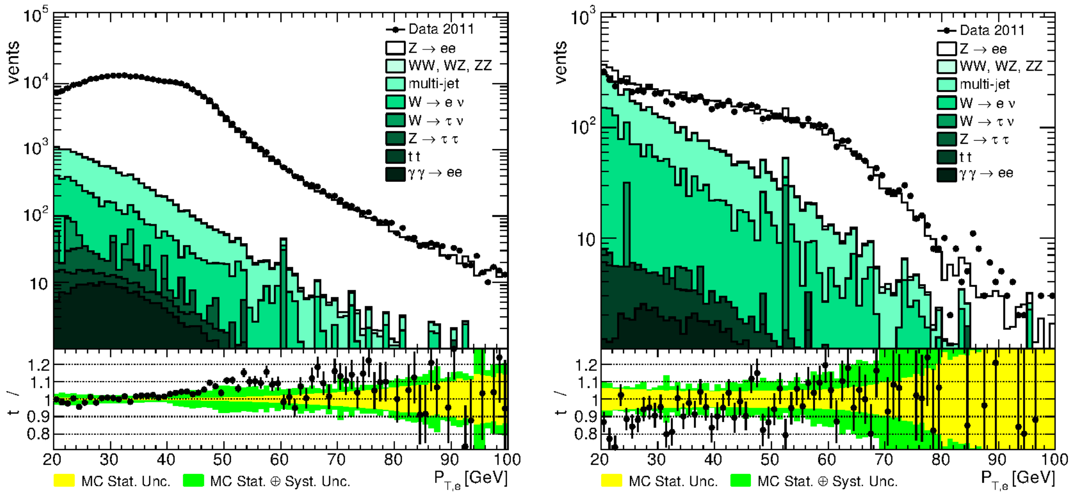

(a) Peak mass

(b) High mass

Figure 13.9: The comparison between data and MC for forward electron p_{T} distribution for peak mass and high mass regions.

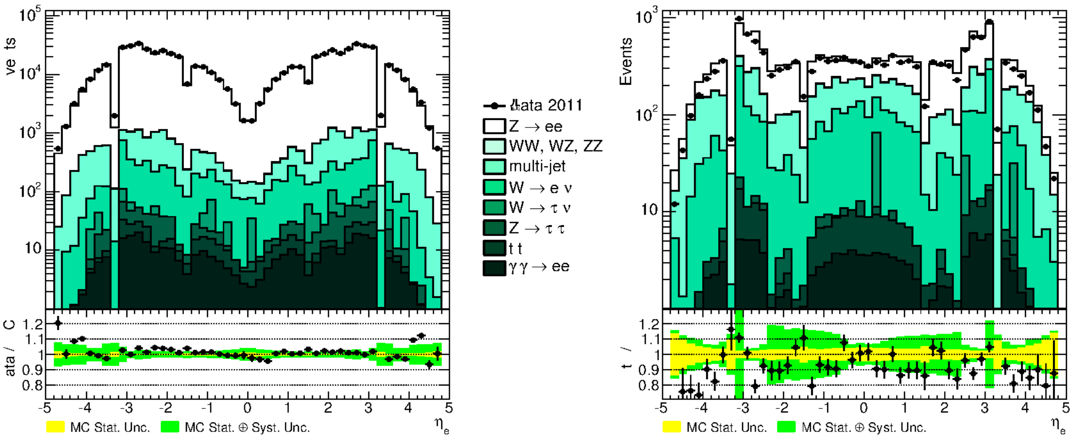

(a) Peak mass

(b) High mass

Figure 13.10: The comparison between data and MC for electron cluster η for peak mass and high mass regions.

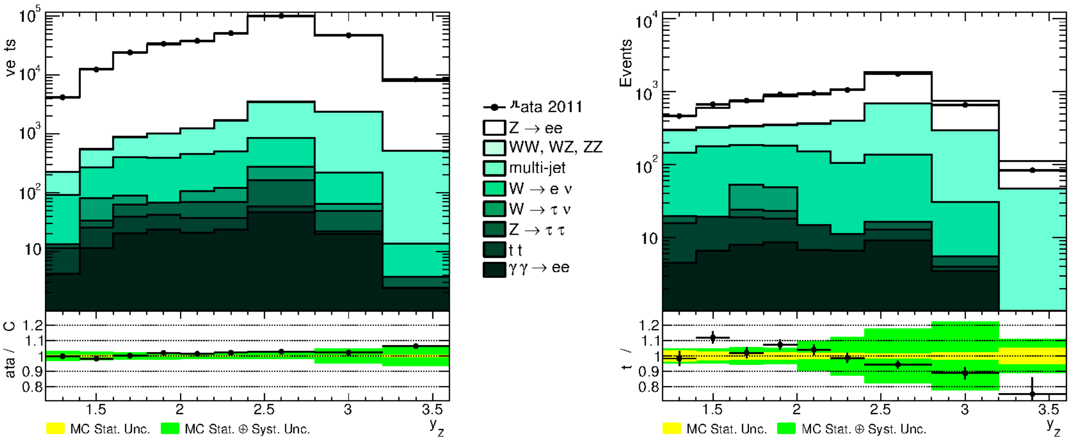

(a) Peak mass (b) High mass

Figure 13.11: The comparison between data and MC for Z boson rapidity distribution for peak mass and high mass regions.

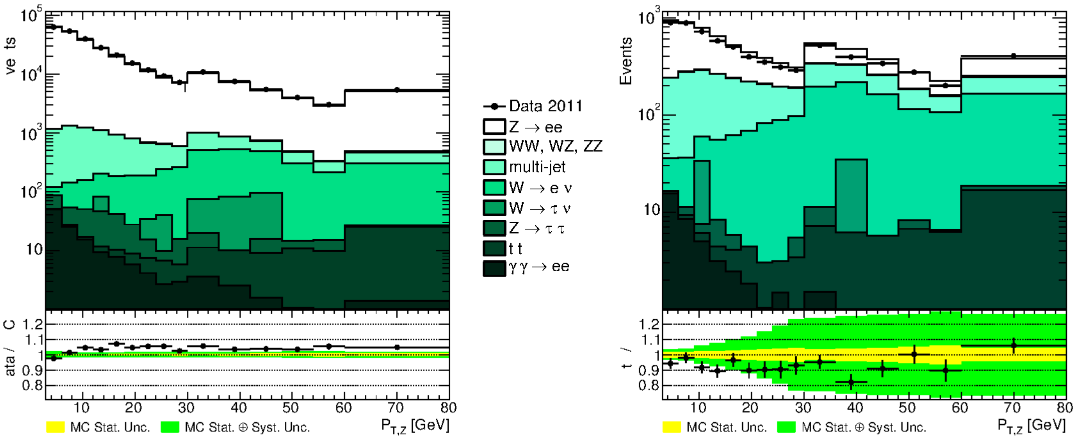

(a) Peak mass (b) High mass

Figure 13.12: The comparison between data and MC for Z boson p_{T} distribution for peak mass and high mass regions.

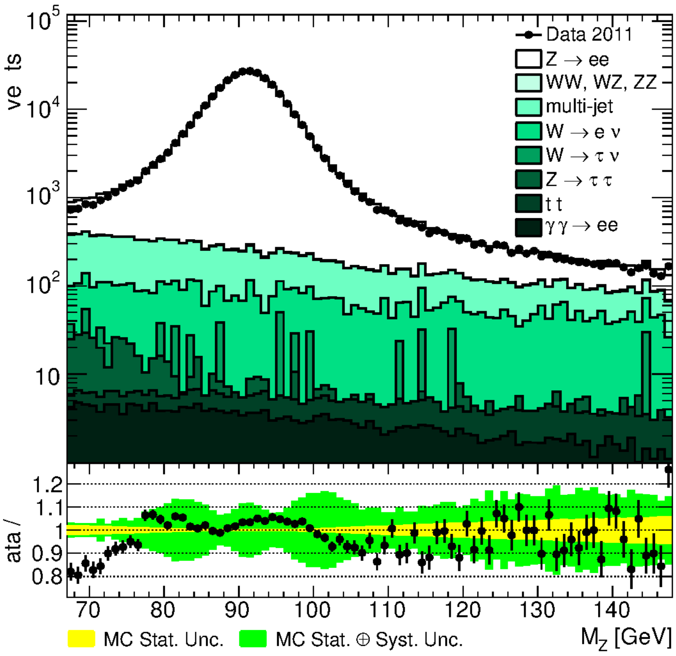

Figure 13.13: The comparison between data and MC for $Z \to ee$ mass-distribution for both peak mass and high mass regions.

CHAPTER 14

Results

In this section the results of the cross-section calculations are presented. The results of the integral and differential cross-sections (as defined in Section 11) are shown together with uncertainties and theoretical predictions. There are two main types of the uncertainties: statistical and systematical, and whereas the statistical uncertainties are trivial to calculate, and depend only on the amount of the data in any given bin, the sources for the systematical uncertainties are much more numerous. The sources for the different systematical uncertainties are listed in Tab. 14.1 for peak mass region and in Tab. 14.2 for high mass region. The efficiency uncertainties were described in the Section 12, the resolution and scale were described in Section 8, the background was described in Section 13, and the rest are the theory uncertainties. The systematic uncertainties are also shown at Figure 14.1. Note, that on the image the different uncertainties are just stacked one on top of another, so the total amount of uncertainty shown on the plot in every given bin won't be the same as the resulting uncertainty for that bin, which would require the quadratic sum. From the plots it can be easily seen, that for the peak mass region the uncertainties are largely dominated by the identification efficiency for the forward electron, while in the high mass region the main contributors is the forward electron resolution.

As the work that was done as part of this thesis contributed to the W,Z inclusive paper [1] the combined $Z \to ee$ and $Z \to \ell\ell$ results were taken from there. The theory comparison that was done for the combined $Z \to \ell\ell$ results was outside of the scope of this thesis.

The double-differential analyses were done in the rapidity and mass binning with three mass windows. The $Z \to ee$ central-forward analysis contributed only to two of them: the peak mass ($66 < M_{ee} < 116$ GeV) and the high mass ($116 < M_{ee} < 150$ GeV) windows. Unlike the central-central analysis, the peak mass windows was not divided into additional bins. The analyses results were first calculated in the true experimental fiducial volume, which equals to the experimental phase space and is described in Tab. 14.3. Figure 14.2 shows the double-differential cross-section with statistical and systematical uncertainties, and Figure 14.3 shows the comparison with the different MC simulations. The POWHEGPYTHIA6 MC simulation was the one used as signal MC, while the others were used as sources for systematical uncertainties.

The same results in tabular form can be seen in Tabs. 14.4 and 14.5, where N is the number of events in the bin, B is the estimated number of the background events included in N, and

$\lvert\eta\rvert$ bin boundary	low	1.20	1.40	1.60	1.80	2.00	2.20	2.40	2.80	3.20
	high	1.40	1.60	1.80	2.00	2.20	2.40	2.80	3.20	3.60
Trigger efficiency		0.159	0.072	0.067	0.064	0.070	0.068	0.089	0.115	0.220
Recon. efficiency		0.499	0.370	0.340	0.251	0.180	0.122	0.093	0.149	0.307
Id. efficiency		0.258	0.223	0.210	0.166	0.157	0.133	0.164	0.216	0.436
Id.Fwd efficiency		3.215	2.898	2.641	2.450	2.070	1.840	1.634	5.443	6.991
Iso. efficiency		0.090	0.082	0.078	0.091	0.064	0.077	0.067	0.067	0.179
Electron resolution		0.073	0.029	0.046	0.008	0.051	0.072	0.023	0.010	0.117
Fwd Electron resolution		0.984	0.696	0.513	1.727	2.632	1.883	3.002	0.451	0.353
Electron scale		0.438	0.277	0.186	0.212	0.255	0.154	0.114	0.097	0.247
Fwd Electron scale		0.410	0.243	0.124	0.042	0.161	0.096	0.156	0.432	2.114
Matrix element		0.138	0.138	0.138	0.138	0.138	0.138	0.138	0.138	0.138
PS and hadronization		0.522	0.522	0.522	0.522	0.522	0.521	0.521	0.521	0.521
PDF		0.124	0.057	0.031	0.015	0.015	0.010	0.007	0.021	0.057
EW Bkg		0.386	0.325	0.197	0.163	0.156	0.132	0.120	0.064	0.029
QCD Bkg		0.228	0.174	0.177	0.248	0.220	0.083	0.187	0.093	0.289
Tot. Syst. Uncertainty		3.540	3.107	2.797	3.084	3.426	2.707	3.480	5.515	7.368
Stat. Uncertainty (MC)		0.635	0.353	0.207	0.206	0.186	0.175	0.126	0.199	0.453
Stat. Uncertainty		1.763	1.019	0.730	0.595	0.580	0.499	0.339	0.494	1.227

Table 14.1: The list of the uncertainties in percent for peak mass region.

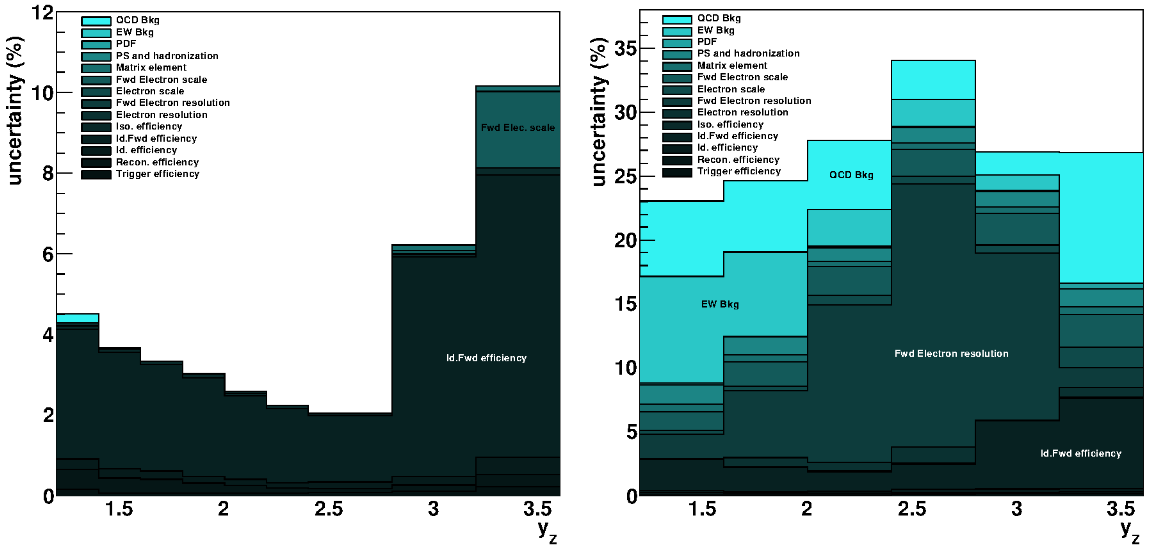

Figure 14.1: The list of the systematic uncertainties for the $Z \to ee$ CF analysis for peak mass (left) and high mass (right) regions. The largest sources are explicitly labeled. Each following uncertainty is placed on top of the previous.

$\lvert\eta\rvert$ bin boundary	low high	1.20 1.60	1.60 2.00	2.00 2.40	2.40 2.80	2.80 3.20	3.20 3.60
Trigger efficiency		0.067	0.037	0.058	0.109	0.139	0.191
Recon. efficiency		0.195	0.158	0.147	0.142	0.137	0.135
Id. efficiency		0.132	0.113	0.170	0.246	0.256	0.243
Id.Fwd efficiency		2.463	1.919	1.517	1.955	5.330	7.069
Iso. efficiency		0.046	0.053	0.080	0.096	0.078	0.079
Electron resolution		0.459	0.714	0.672	1.254	1.102	0.753
Fwd Electron resolution		2.357	5.231	12.303	20.601	14.154	1.554
Electron scale		0.302	0.354	0.717	0.592	0.609	1.607
Fwd Electron scale		1.470	1.884	2.252	2.086	2.497	2.566
Matrix element		0.606	0.568	0.429	0.494	0.488	0.565
PS and hadronization		1.480	1.385	1.048	1.208	1.195	1.397
PDF		0.162	0.081	0.110	0.074	0.099	0.471
EW Bkg		8.332	6.544	2.880	2.144	1.184	0.000
QCD Bkg		5.904	5.575	5.417	3.043	1.828	10.225
Tot. Syst. Uncertainty		11.044	10.576	14.109	21.221	15.594	13.012
Stat. Uncertainty (MC)		1.619	1.156	0.981	0.930	1.716	3.892
Stat. Uncertainty		6.845	5.213	4.023	3.886	5.291	14.533

Table 14.2: The list of the uncertainties in percent for high mass region.

Central electron	$p_{\mathrm{T}} > 23$ GeV, $\lvert\eta\rvert < 2.47$ **excluding** $1.37 < \lvert\eta\rvert < 1.52$ & $1.6 < \lvert\eta\rvert < 1.7$
Forward electron	$p_{\mathrm{T}} > 20$ GeV, $2.5 < \lvert\eta\rvert < 4.9$ **excluding** $3.16 < \lvert\eta\rvert < 3.35$
Mass windows	$66 < m_{ee} < 116$ & $116 < m_{ee} < 150$

Table 14.3: The conditions of the experimental phase space.

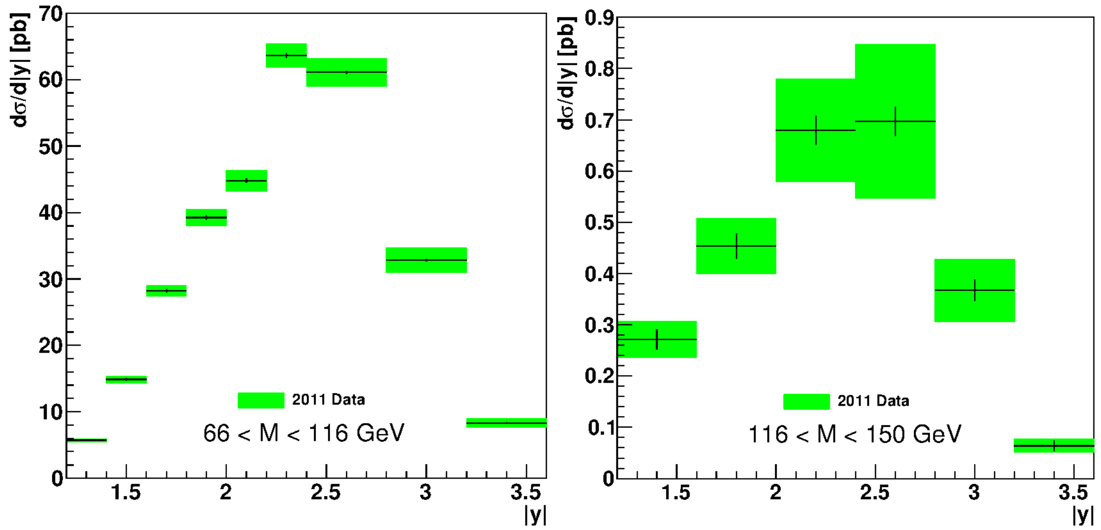

Figure 14.2: Differential $Z \to ee$ CF cross-section, measured in the true experimental fiducial volume, as a function of absolute boson rapidity for peak mass (left) and high mass (right) regions together with statistical and systematic uncertainties.

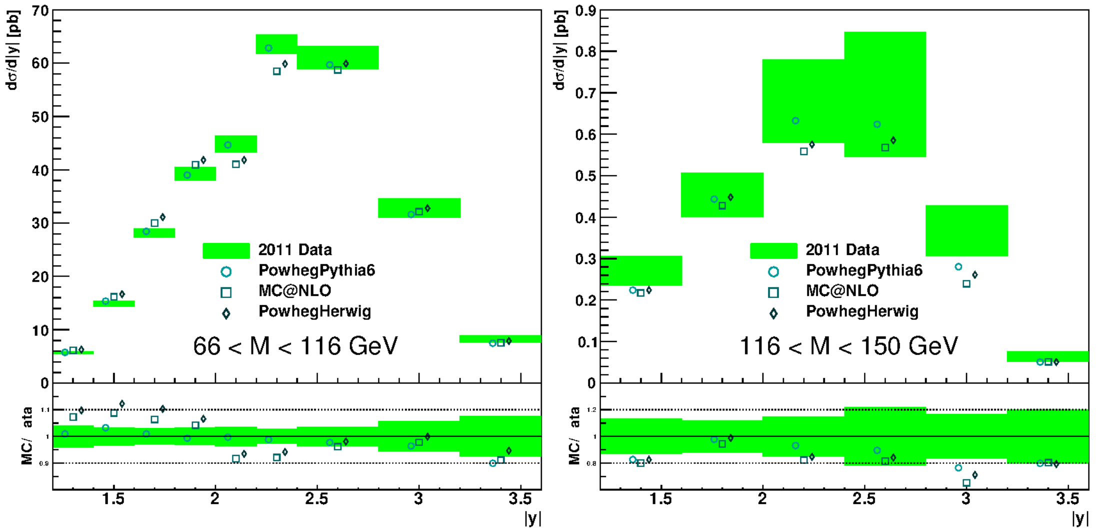

Figure 14.3: Differential $Z \to ee$ CF cross-section, measured in the true experimental fiducial volume, as a function of absolute boson rapidity for peak mass (left) and high mass (right) regions compared to various MC simulations.

	N	$B \pm \delta B$	$C \pm \delta C$
$1.20 < \|y\| < 1.40$	4178	193.7 ± 19.7	0.381 ± 0.014
$1.40 < \|y\| < 1.60$	12404	517.7 ± 47.4	0.436 ± 0.013
$1.60 < \|y\| < 1.80$	24210	812.1 ± 72.7	0.453 ± 0.012
$1.80 < \|y\| < 2.00$	33978	1021.2 ± 110.9	0.459 ± 0.014
$2.00 < \|y\| < 2.20$	38023	1141.2 ± 123.9	0.449 ± 0.015
$2.20 < \|y\| < 2.40$	51372	1454.4 ± 77.6	0.429 ± 0.011
$2.40 < \|y\| < 2.80$	101004	2613.2 ± 267.5	0.440 ± 0.015
$2.80 < \|y\| < 3.20$	47304	1104.4 ± 52.3	0.384 ± 0.021
$3.20 < \|y\| < 3.60$	8453	126.6 ± 29.5	0.276 ± 0.020

Table 14.4: Main components of the differential $Z \to ee$ CF cross-section for peak mass region.

	N	$B \pm \delta B$	$C \pm \delta C$
$1.20 < \|y\| < 1.60$	1136	592.4 ± 54.8	0.552 ± 0.024
$1.60 < \|y\| < 2.00$	1676	754.6 ± 79.2	0.565 ± 0.035
$2.00 < \|y\| < 2.40$	2006	737.4 ± 80.2	0.531 ± 0.067
$2.40 < \|y\| < 2.80$	1754	506.2 ± 48.6	0.515 ± 0.107
$2.80 < \|y\| < 3.20$	659	120.7 ± 12.8	0.439 ± 0.068
$3.20 < \|y\| < 3.60$	84	15.2 ± 8.3	0.348 ± 0.031

Table 14.5: Main components of the differential $Z \to ee$ CF cross-section for high mass region.

C is the true experimental fiducial extrapolation factor, which represents the fraction of all the Z boson that N amounts to.

In Tabs. 14.6 and 14.7 the results of the cross-section as measured in the true experimental fiducial volume can be found along with statistical, systematical and luminosity uncertainties.

For the comparison with the theoretical predictions, the results were extrapolated to the fiducial volume, which differs from the true experimental fiducial volume in inclusion of the crack regions. As a result, the values are about ~20% higher as in the true experimental one. The theoretical predictions were calculated at NLO using the MCFM software [108] and then corrected to NNLO using the k-factor produces by FEWZ software [109, 110]. Figure 14.4 shows the comparison to the theoretical predictions done with various PDF sets.

The following results for the $Z \to \ell\ell$ combined cross sections were taken from the W,Z inclusive paper [1], as the combination of the results was outside of the scope of this thesis. The combination technique was described in Section 11.3. It is important to note, that $Z \to ee$ central-forward data contributed only to the $|y| > 1.2$ part of the combined cross-section, and the last three bins $|y| > 2.4$ of it can be seen as purely $Z \to ee$ central-forward. The combined cross-section itself can be seen in Figure 14.5, while the comparison with the different theoretical predictions can be seen in Figure 14.6.

$1.20 < \lvert y\rvert < 1.40$	5.715 ± 0.101 (stat) $\pm$ 0.207 (syst) $\pm$ 0.103 (lum) [pb]
$1.40 < \lvert y\rvert < 1.60$	14.864 ± 0.151 (stat) $\pm$ 0.465 (syst) $\pm$ 0.268 (lum) [pb]
$1.60 < \lvert y\rvert < 1.80$	28.200 ± 0.206 (stat) $\pm$ 0.792 (syst) $\pm$ 0.508 (lum) [pb]
$1.80 < \lvert y\rvert < 2.00$	39.245 ± 0.233 (stat) $\pm$ 1.214 (syst) $\pm$ 0.706 (lum) [pb]
$2.00 < \lvert y\rvert < 2.20$	44.786 ± 0.260 (stat) $\pm$ 1.534 (syst) $\pm$ 0.806 (lum) [pb]
$2.20 < \lvert y\rvert < 2.40$	63.598 ± 0.317 (stat) $\pm$ 1.717 (syst) $\pm$ 1.145 (lum) [pb]
$2.40 < \lvert y\rvert < 2.80$	61.087 ± 0.207 (stat) $\pm$ 2.126 (syst) $\pm$ 1.100 (lum) [pb]
$2.80 < \lvert y\rvert < 3.20$	32.826 ± 0.162 (stat) $\pm$ 1.811 (syst) $\pm$ 0.591 (lum) [pb]
$3.20 < \lvert y\rvert < 3.60$	8.313 ± 0.102 (stat) $\pm$ 0.614 (syst) $\pm$ 0.150 (lum) [pb]

Table 14.6: Differential $Z \to ee$ CF cross-section for the peak mass region, measured in the true experimental fiducial volume together with uncertainties.

$1.20 < \lvert y\rvert < 1.60$	0.271 ± 0.018 (stat) $\pm$ 0.030 (syst) $\pm$ 0.005 (lum) [pb]
$1.60 < \lvert y\rvert < 2.00$	0.454 ± 0.023 (stat) $\pm$ 0.047 (syst) $\pm$ 0.008 (lum) [pb]
$2.00 < \lvert y\rvert < 2.40$	0.680 ± 0.027 (stat) $\pm$ 0.095 (syst) $\pm$ 0.012 (lum) [pb]
$2.40 < \lvert y\rvert < 2.80$	0.697 ± 0.027 (stat) $\pm$ 0.147 (syst) $\pm$ 0.013 (lum) [pb]
$2.80 < \lvert y\rvert < 3.20$	0.367 ± 0.019 (stat) $\pm$ 0.057 (syst) $\pm$ 0.007 (lum) [pb]
$3.20 < \lvert y\rvert < 3.60$	0.064 ± 0.009 (stat) $\pm$ 0.009 (syst) $\pm$ 0.001 (lum) [pb]

Table 14.7: Differential $Z \to ee$ CF cross-section for the high mass region, measured in the true experimental fiducial volume together with uncertainties.

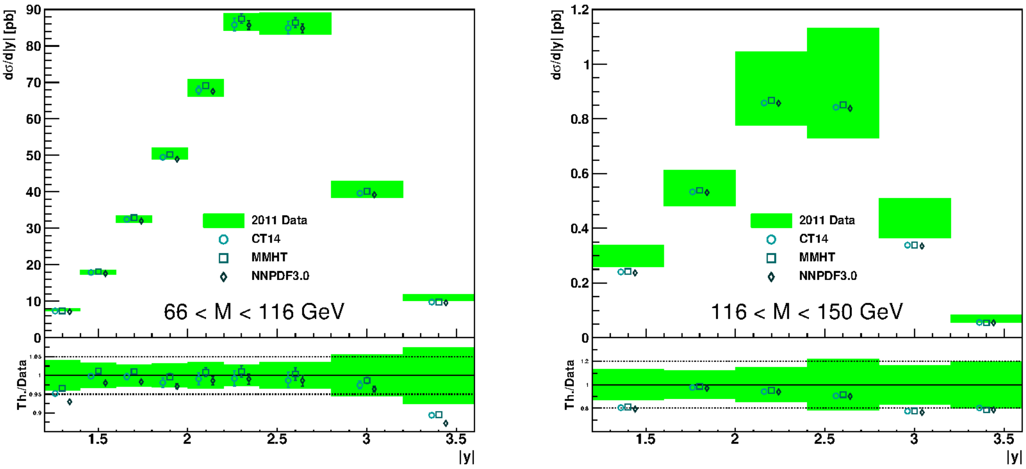

Figure 14.4: Differential $Z \to ee$ CF cross-section, measured in the extrapolated fiducial volume, as a function of absolute boson rapidity for peak mass (left) and high mass (right) regions compared to various theoretical predictions.

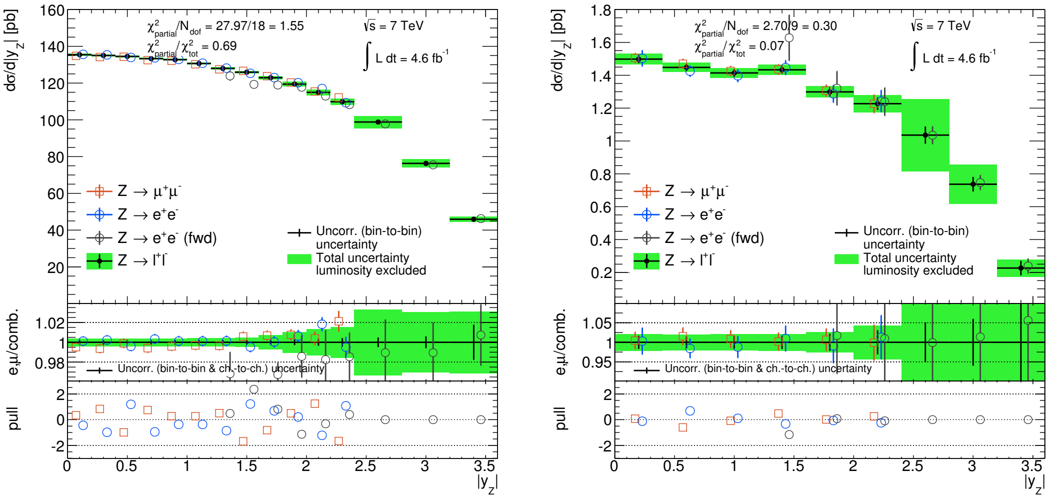

Figure 14.5: Combined $Z \to \ell\ell$ cross-section for peak mass (left) and high mass (right) regions together with uncertainties. The ratio and the pull values are also shown for each source. [1]

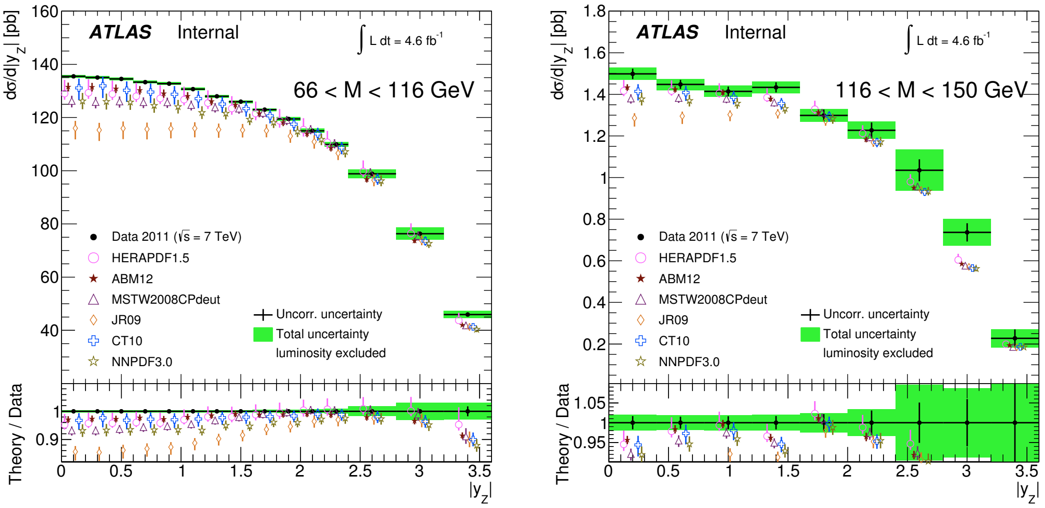

Figure 14.6: Comparison of the combined $Z \to \ell\ell$ cross-section with NNLO predictions using various PDF sets for peak mass (left) and high mass (right) regions together with uncertainties. The ratios are also shown. [1]

CHAPTER 15

Summary

This thesis represented the results of the $Z \to ee$ central-forward cross-section measurement based on the 4.6fb^{-1} of the data collected on the ATLAS detector of the LHC during the 2011 year.

In order to get these results some technical solutions were developed for both ATLAS software infrastructure and the analysis software itself. For the ATLAS software the Frozen Showers system was developed. This system reduced the amount of time needed for the Monte Carlo simulation by about 25% while introducing a small error that was well within the uncertainties introduced by the technical limitations of the detector. The Frozen Shower system was enabled by default in all the Monte Carlo samples starting with the 2011 for all the analyses. The MC samples used in this analysis were also produced with Frozen Showers enabled.

For the analysis software the new TTree system was developed that was used for data storage. This system reduced the amount of space needed for data samples from terabytes to gigabytes and subsequently allowed to launch the analysis software on local machines and reduced the time needed for the analysis. With the TTree input the ZeeD software was able to process 1000 events per second which makes a couple of hours for the whole dataset, instead of several days that the same task would take while on the GRID reading from the raw AODs. The analysis presented in this thesis was done using the TTree system.

The different stages of the analysis included the identification of the electrons, finding of the boson candidates, filtering of the $Z \to ee$ events based on several criteria (cuts), estimating of the background and the unfolding. Each stage was described in a separate chapter, presenting its impact on the result and the possible sources of the uncertainties it adds. The resulting double-differential $Z \to ee$ central-forward cross-section together with all sources of uncertainties was presented. This cross-section agrees well with the results of $Z \to ee$ central-central and $Z \to \mu\mu$ analyses, and in combination with them can be used for a future improvement of PDF sets.

List of Figures

Bibliography

[1] K. Bachas et al., *Measurement and QCD analysis of differential inclusive* $W^{\pm} \to \ell\nu$ *and* $Z \to \ell\ell$ *production and leptonic decay cross sections with ATLAS*, ATL-COM-PHYS-2013-217. 1, 105, 109, 111

[2] G. Arnison et al., *Experimental Observation of Isolated Large Transverse Energy Electrons with Associated Missing Energy at* $\sqrt{s} = 540\ GeV$, Phys. Lett. **122B** (1983) 103. 3, 8

[3] F. Abe et al., *Observation of Top Quark Production in* $\bar{p}p$ *Collisions with the Collider Detector at Fermilab*, Phys. Rev. Lett. **74** (1995) 2626–2631. 3, 10

[4] DONUT Collaboration, K. Kodama et al., *Observation of tau neutrino interactions*, Phys. Lett. B **504** (2001) 218–224, `arXiv:hep-ex/0012035 [hep-ex]`. 3

[5] M. C. Gonzalez-Garcia and Y. Nir, *Neutrino masses and mixing: evidence and implications*, Rev. Mod. Phys. **75** (2003) 345–402, `arXiv:hep-ph/0202058 [hep-ph]`. 3

[6] T2K Collaboration, K. Abe et al., *Evidence of electron neutrino appearance in a muon neutrino beam*, Phys. Rev. D. **88** (2013). 3

[7] “CERN Summer Student Webfest.” `https://webfest.web.cern.ch/`. 4

[8] Particle Data Group Collaboration, J. Beringer et al., *Review of Particle Physics*, Phys.Rev.D **86** (2012) 010001. 5

[9] R. McCormmach, *H. A. Lorentz and the electromagnetic view of nature*, Isis **61** (1970) 459–497. 5

[10] B. G. Doran, *Origins and consolidation of field theory in 19th century Britain: From the mechanical to the electromagnetic view of nature*, Hist. Stud. Phys. Sci. **6** (1975) 133–260. 5

[11] Đ. Hirosige, *Electrodynamics before the theory of relativity*, Jap. Stud. Hist. Sci. **5** (1966) 1–49. 5

[12] J. Thomson, *Cathode Rays*, Philosophical Magazine **44** (1897) 293–316. 5

[13] W. Kaufmann, *Die elektromagnetische Masse des Elektrons*, Phys. Zeitschr. **4** (1902) 54–57. 5

[14] W. Kaufmann, *Über die Konstitution des Elektrons*, Sitzungsberichte der Königlich Preussischen Akademie der Wissenschaften **45** (1905) 949–956. 5

[15] A. Einstein, *Zur Elektrodynamik bewegter Körper*, Annalen der Physik **17** (1905) 891–921. 5

[16] H. Minkowski, *Die Grundgleichungen für die elektromagnetischen Vorgänge in bewegten Körpern*, Göttinger Nachr. (1908) 53. 5

[17] H. Minkowski, *Raum und Zeit*, Jahresberichte der Deutschen Mathematiker-Vereinigung (1909). 5

[18] G. Mie, *Grundlagen einer Theorie der Materie*, Annalen der Physik **342** (1912) 511–534. 6

[19] G. Mie, *Grundlagen einer Theorie der Materie (Zweite Mitteilung)*, Annalen der Physik **345** (1913) 1–66. 6

[20] G. Mie, *Grundlagen einer Theorie der Materie (Dritte Mitteilung, Schluß)*, Annalen der Physik **344** (1912) 1–40. 6

[21] A. Einstein, *Zum gegenwärtigen Stand des Strahlungsproblems*, Phys. Zeitschr. **10** (1909) 185–193. 6

[22] M. Born and L. Infeld, *Foundations of the New Field Theory.* The Royal Society, 1934. 6

[23] J. Ishiwara, *Grundlagen einer relativistischen elektromagnetischen Gravitationstheorie*, Phys. Zeitschr. **15** (1914) 294–298. 6

[24] G. Nordström, *Über die Möglichkeit, das Elektromagnetische Feld und das Gravitationsfeld zu vereiningen*, Phys. Zeitschr. **15** (1914) 504–506. 6

[25] D. Hilbert, *Die Grundlagen der Physik (Erste Mitteilung)*, Nachrichten Gesellschaft der Wissenschaften zu Göttingen (1915) 395–407. 6

[26] D. Hilbert, *Die Grundlagen der Physik (Zweite Mitteilung)*, Nachrichten Gesellschaft der Wissenschaften zu Göttingen (1915) 53–76. 6

[27] H. Weyl, *Raum. Zeit. Materie. Vorlesungen über allgemeine Relativitätstheorie, 5 Aufl.* J. Springer, 1921. 6

[28] T. Kaluza, *Zum Unitätsproblem der Physik*, Sitzungsber. Preuss. Ak. Wiss. (1921) 966–971. 6

[29] L. de Broglie, *Recherches sur la théorie des quanta*, Ann. de Physique **10** (1924). 6

[30] W. Heisenberg, *Über quantentheoretische Umdeutung kinematischer und mechanischer Beziehungen*, Zeitschrift für Physik **33** (1925) 879–893. 6

[31] M. Born and P. Jordan, *Zur Quantenmechanik*, Zeitschrift für Physik **34** (1925) 858–888. 6

[32] M. Born, W. Heisenberg, and P. Jordan, *Zur Quantenmechanik II*, Zeitschrift für Physik **35** (1925) 557–615. 6

[33] W. Heisenberg, *Über das Verhältnis der Heisenberg-Born-Jordanschen Quantenmechanik zu der meinem*, Annalen der Physik **384** (1926) 734–756. 6

[34] W. Heisenberg, *Über den anschaulichen Inhalt der quantentheoretischen Kinematik und Mechanik*, Zeitschrift für Physik **43** (1927) 172–198. 6

[35] P. A. M. Dirac, *The Quantum Theory of the Electron*, Proceedings of the Royal Society of London. **117** (1928) 610–624. 6

[36] C. D. Anderson, *The Positive Electron*, Phys. Rev. **43** (1933) 491. 6

[37] V. Fock, *Über die invariante Form der Wellen- und der Bewegungsgleichungen für einen geladenen Massenpunkt*, Zeitschrift für Physik **38** (1926) 226–232. 7

[38] F. London, *Quantenmechanische Deutung der Theorie von Weyl*, Zeitschrift für Physik **42** (1927) 375–389. 7

[39] H. Weyl, *Elektron und Gravitation*, Zeitschrift für Physik **56** (1929) 330–352. 7

[40] C. N. Yang and R. L. Mills, *Conservation of Isotopic Spin and Isotopic Gauge Invariance*, Phys. Rev. **96** (1954) 191–195. 7

[41] L. Faddeev and V. Popov, *Feynman diagrams for the Yang-Mills field*, Phys. Lett. **25** (1967) 29–30. 8

[42] E. Fermi, *Versuch einer Theorie der β-strahlung*, Zeitschrift für Physik **88** (1934) 161–177. 8

[43] C. S. Wu et al., *Experimental Test of Parity Conservation in Beta Decay*, Phys. Rev. **105** (1957) 1413–1415. 8

[44] R. Feynman and M. Gell-Mann, *Theory of the Fermi Interaction*, Phys. Rev. **109** (1958) 193. 8

[45] J. Christenson, J. Cronin, V. Fitch, and R. Turlay, *Evidence for the 2π Decay of the K_2^0 Meson*, Phys. Rev. Lett. **13** (1964) 138. 8

[46] S. Weinberg, *A Model of Leptons*, Phys. Rev. Lett. **19** (1967) 1264. 8

[47] G. 't Hooft and M. Veltman, *Regularization and Renormalization of Gauge Fields*, Nucl.Phys. **B44** (1972) 189–219. 8

[48] F. Hasert et al., *Observation of neutrino-like interactions without muon or electron in the Gargamelle neutrino experiment*, Phys. Lett. **46B** (1973) 138. 8

[49] G. D. Rochester and B. C. C., *Evidence for the existence of new unstable elementary particles*, Nature **160** (1947) 855–857. 9

[50] Y. H., *On the Interaction of Elementary Particles. I*, Proc. Phys.-Math. Soc. Japan **17** (1935) 48. 9

[51] C. M. G. Latters, M. H., O. G. P. S., and P. C. F., *Processes Involving Charged Mesons*, Nature **159** (1947) 694–697. 9

[52] Y. Ne'eman, *Derivation of Strong Interactions from a Gauge Invariance*, Nucl. Phys. **26** (1961) 222–229. 9

[53] M. Gell-Mann, *Symmetries of Baryons and Mesons*, Phys. Rev. **125** (1962) 1067. 9

[54] V. E. Barnes, *Observation of a Hyperon with Strangeness Minus Three*, Phys. Rev. Lett. **12** (1964) 204. 9

[55] M. Gell-Mann, *A Schematic Model of Baryons and Mesons*, Phys. Lett. **8** (1964) 214–215. 9

[56] G. Zweig, *An SU_3 model for strong interaction symmetry and its breaking*, CERN-TH-412. `https://cds.cern.ch/record/570209`. 9

[57] O. W. Greenberg, *Spin and Unitary Spin Independence in a Paraquark Model of Baryons and Mesons*, Phys. Rev. Lett. **13** (1964) 598–602. 9

[58] S. L. Glashow, J. Iliopoulos, and L. Maiani, *Weak Interactions with Lepton-Hadron Symmetry*, Phys. Rev. D **2** (1970) 1285–1292. 10

[59] M. Kobayashi and T. Maskawa, *CP-Violation in the Renormalizable Theory of Weak Interaction*, Prog. Theor. Phys. **49** (1973) 652–657. 10

[60] D. J. Gross and F. Wilczek, *Asymptotically Free Gauge Theories. I*, Phys. Rev. D **8** (1973) 3633. 10

[61] H. D. Politzer, *Reliable Perturbative Results for Strong Interactions?*, Phys. Rev. Lett. **30** (1973) 1346. 10

[62] J. E. Augustin et al., *Discovery of a Narrow Resonance in e^+e^- Annihilation*, Phys. Rev. Lett. **33** (1974) 1406–1408. 10

[63] J. J. Aubert et al., *Experimental Observation of a Heavy Particle J*, Phys. Rev. Lett. **33** (1974) 1404–1406. 10

[64] J. A. Appel et al., *Observation of a Dimuon Resonance at 9.5 GeV in 400-GeV Proton-Nucleus Collisions*, Phys. Rev. Lett. **39** (1977) 252–255. 10

[65] J. D. Bjorken and E. A. Paschos, *Inelastic Electron-Proton and γ-Proton Scattering and the Structure of the Nucleon*, Phys. Rev. **185** (1969) 1975. 10

[66] H.-L. Lai, M. Guzzi, J. Huston, Z. Li, P. M. Nadolsky, et al., *New parton distributions for collider physics*, Phys.Rev. **D82** (2010) 074024, `arXiv:1007.2241 [hep-ph]`. 12, 37

[67] A. Martin, W. Stirling, R. Thorne, and G. Watt, *Parton distributions for the LHC*, Eur.Phys.J. **C63** (2009) 189–285, `arXiv:0901.0002 [hep-ph]`. 12

[68] A. Martin, W. Stirling, R. Thorne, and G. Watt, *Uncertainties on α_S in global PDF analyses and implications for predicted hadronic cross sections*, Eur.Phys.J. **C64** (2009) 653–680, `arXiv:0905.3531 [hep-ph]`. 12

[69] L. A. Harland-Lang, A. D. Martin, P. Motylinski, and R. Thorne, *Parton distributions in the LHC era: MMHT 2014 PDFs*, Eur.Phys.J. **C75** (2015) 204, `arXiv:1412.3989 [hep-ph]`. 12

[70] S. Alekhin, J. Blumlein, and S. Moch, *Parton distribution functions and benchmark cross sections at NNLO*, Phys.Rev. **D86** (2012) 054009, `arXiv:1202.2281 [hep-ph]`. 12

[71] H1 and ZEUS Collaboration, F. Aaron et al., *Combined Measurement and QCD Analysis of the Inclusive ep Scattering Cross Sections at HERA*, JHEP **1001** (2010) 109, `arXiv:0911.0884 [hep-ex]`. 12

[72] R. D. Ball, L. Del Debbio, S. Forte, A. Guffanti, J. I. Latorre, J. Rojo, and M. Ubiali, *A first unbiased global NLO determination of parton distributions and their uncertainties*, Nucl.Phys. **B838** (2010) 136–206, `arXiv:1002.4407 [hep-ph]`. 12

[73] R. D. Ball, L. Del Debbio, S. Forte, A. Guffanti, J. I. Latorre, J. Rojo, and M. Ubiali, *Impact of Heavy Quark Masses on Parton Distributions and LHC Phenomenology*, Nucl.Phys. **B849** (2011) 296–363, `arXiv:1101.1300 [hep-ph]`. 12

[74] R. D. Ball, V. Bertone, S. Carrazza, C. S. Deans, L. Del Debbio, S. Forte, A. Guffanti, N. P. Hartland, J. I. Latorre, J. Rojo, and M. Ubiali, *Parton distributions with LHC data*, Nucl.Phys. **B867** (2013) 244–289, `arXiv:1207.1303 [hep-ph]`. 12

[75] D. Bourilkov, R. C. Group, and M. R. Whalley, *LHAPDF: PDF use from the Tevatron to the LHC*, `arXiv:hep-ph/0605240 [hep-ph]`. 12

[76] M. Aharrouche et al., *Double differential Z,W cross sections and their ratios in the electron channel*, Tech. Rep. ATL-COM-PHYS-2010-325, CERN, Geneva, Jun, 2010. 14

[77] "LHC Accelerators, CERN's 60th anniversary."
`http://cern60.web.cern.ch/en/exhibitions/lhc-accelerators`. 18

[78] ATLAS Collaboration, G. Aad et al., *The ATLAS Experiment at the CERN Large Hadron Collider*, JINST **3** (2008) S08003. 21, 22, 23, 24, 27, 28

[79] ATLAS Collaboration, *Performance of the ATLAS Electron and Photon Trigger in p-p Collisions at sqrts = 7 TeV in 2011*, Tech. Rep. ATLAS-CONF-2012-048, CERN, Geneva, May, 2012. 30

[80] ATLAS Collaboration, G. Aad et al., *Improved luminosity determination in pp collisions at $\sqrt{s} = 7$ TeV using the ATLAS detector at the LHC*, CERN-PH-EP-2013-026, `arXiv:1302.4393 [hep-ex]`. 31, 32

[81] "Atlas Public > Luminosity Public Results."
`https://twiki.cern.ch/twiki/bin/view/AtlasPublic/LuminosityPublicResults`. 33

[82] GEANT4 Collaboration, S. Agostinelli et al., *GEANT4: A simulation toolkit*, Nucl. Instrum. Meth. **A506** (2003) 250–303. 34

[83] P. Golonka and Z. Was, *PHOTOS Monte Carlo: A Precision tool for QED corrections in Z and W decays*, Eur. Phys. J. **C45** (2006) 97–107, `arXiv:hep-ph/0506026`. 35

[84] G. Corcella, I. Knowles, G. Marchesini, S. Moretti, K. Odagiri, P. Richardson, M. Seymour, and B. Webber, *HERWIG 6.5: an event generator for Hadron Emission Reactions With Interfering Gluons (including supersymmetric processes)*, JHEP **01** (2001) 010, `arXiv:hep-ph/0011363`. 36

[85] T. Sjostrand, S. Mrenna, and P. Skands, *PYTHIA 6.4 Physics and Manual*, JHEP **05** (2006) 026, `arXiv:hep-ph/0603175`. 36

[86] T. Sjostrand, S. Mrenna, and P. Skands, *Brief Introduction to PYTHIA 8.1*, Comput. Phys. Comm. **178** (2008) 85, `arXiv:0710.3820v1 [hep-ph]`. 36

[87] S. Frixione, P. Nason, and G. Ridolfi, *The POWHEG-hvq manual version 1.0*, `arXiv:0707.3081 [hep-ph]`. 36

[88] S. Frixione, F. Stoeckli, P. Torrielli, B. R. Webber, and C. D. White, *The MC@NLO 4.0 Event Generator*, `arXiv:1010.0819 [hep-ph]`. 36

[89] T. Gleisberg, S. Höche, P. Krauss, A. Schälicke, S. Schumann, and J. Winter, *SHERPA 1.α, a proof-of-concept version*, JHEP **02** (2004) 056, `arXiv:hep-ph/0311263 [hep-ph]`. 36

[90] T. Gleisberg, S. Höche, P. Krauss, M. Schönherr, S. Schumann, F. Siegert, and J. Winter, *Event generation with SHERPA 1.1*, JHEP **02** (2009) 007, `arXiv:0811.4622 [hep-ph]`. 36

[91] ATLAS Collaboration, G. Aad et al., *New ATLAS event generator tunes to 2010 data*, ATL-PHYS-PUB-2011-008. `http://cds.cern.ch/record/1345343`. 37

[92] ATLAS Collaboration, G. Aad et al., *ATLAS tunes of PYTHIA 6 and Pythia 8 for MC11*, ATL-PHYS-PUB-2011-009. `http://cds.cern.ch/record/1363300`. 37

[93] J. Pumplin, D. Stump, J. Huston, H. Lai, P. Nadolsky, and W. Tung, *New Generation of Parton Distributions with Uncertainties from Global QCD Analysis*, JHEP **0207** (2002) 012 MSU-HEP-011101, `arXiv:hep-ph/0201195 [hep-ph]`. 37

[94] ATLAS Collaboration, G. Aad et al., *Measurement of angular correlations in Drell-Yan lepton pairs to probe Z/gamma* boson transverse momentum at sqrt(s)=7 TeV with the ATLAS detector*, CERN-PH-EP-2012-325, `arXiv:1211.6899 [hep-ex]`. 50

[95] M. Boonekamp, A. Vicini, et al., *Improved LO electroweak approximations for Z and W Generators*, Tech. Rep. CERN, Geneva, Oct, 2012. `https://twiki.cern.ch/twiki/pub/AtlasProtected/WZElectroweakCommonTopics2011/IBA.pdf`. See also `https://indico.cern.ch/getFile.py/access?contribId=38&sessionId=2&resId=0&materialId=slides&confId=203748` and `https://indico.cern.ch/getFile.py/access?contribId=18&sessionId=2&resId=0&materialId=slides&confId=203748`. 50

[96] ATLAS Collaboration, G. Aad et al., *Expected Performance of the ATLAS Experiment - Detector, Trigger and Physics*, SLAC-R-980, CERN-OPEN-2008-020, `arXiv:0901.0512 [hep-ex]`. 54

[97] ATLAS Collaboration, G. Aad et al., *Electron and photon energy calibration with the ATLAS detector using LHC Run 1 data*, Eur.Phys.J. **C74** no. 10, (2014) 3071 CERN-PH-EP-2014-153, `arXiv:1407.5063 [hep-ex]`. 56

[98] J. P. Archambault et al., *Energy calibration of the ATLAS Liquid Argon Forward Calorimeter*, JINST **3** (2008) P02002. 56

[99] ATLAS Collaboration, M. Boonekamp, L. Carminati, et al., *Supporting note for the 2011 calibration analysis*, Tech. Rep. ATL-COM-PHYS-2012-1473, CERN, Geneva, Nov, 2012. 56

[100] ATLAS Collaboration, G. Aad et al., *Electron reconstruction and identification efficiency measurements with the ATLAS detector using the 2011 LHC proton-proton collision data*, CERN-PH-EP-2014-040, `arXiv:1404.2240`. 58, 85, 86, 88, 90

[101] ATLAS Collaboration, E. Stanecka, *The ATLAS Inner Detector operation, data quality and tracking performance*, `arXiv:1303.3630`. 58

[102] ATLAS Collaboration, W. Lampl et al., *Calorimeter Clustering Algorithms: Description and Performance*, ATL-LARG-PUB-2008-002. `http://cds.cern.ch/record/1099735`. 59

[103] M. Hance, D. Olivito, and H. Williams, *Performance Studies for e/gamma Calorimeter Isolation*, Tech. Rep. ATL-COM-PHYS-2011-1186, CERN, Geneva, Sep, 2011. 62

[104] ATLAS Collaboration, C. Anastopoulos et al., *Supporting document on electron performance measurements using the 2011 LHC proton-proton collision data*, ATL-COM-PHYS-2012-1023. `https://cdsweb.cern.ch/record/1461217`. 68

[105] ATLAS Collaboration, G. Choudalakis, *Unfolding in ATLAS*, `arXiv:1104.2962 [hep-ex]`. 74

[106] G. D'Agostini, *A multidimensional unfolding method based on Bayes' theorem*, Nucl. Instrum. Meth. **A362** (1995) 487. 79

[107] W. Verkerke and D. Kirkby, *The RooFit toolkit for data modelling*, `arXiv:physics/0306116 [physics]`. 94

[108] J. Campbell and R. Ellis, *MCFM for the Tevatron and the LHC*, Nucl.Phys.Proc.Suppl. **205-206** (2010) 10–15, `arXiv:1007.3492 [hep-ph]`. 109

[109] R. Gavin, Y. Li, F. Petriello, and S. Quackenbush, *FEWZ 2.0: A code for hadronic Z production at next-to-next-to-leading order*, Comput.Phys.Commun. **182** (2011) 2388–2403, `arXiv:1011.3540 [hep-ph]`. 109

[110] Y. Li and F. Petriello, *Combining QCD and electroweak corrections to dilepton production in FEWZ*, `arXiv:1208.5967 [hep-ph]`. 109

Acknowledgments

I would like to thank my friends and colleagues without whom this work would've never been finished. First of all, my supervisor Sasha Glazov, without whom this work wouldn't have been even started. Mikhail Karnevskiy and Daniel Britzger both helped me greatly throughout the whole time of my working on this thesis, on both scientific and personal issues, thank you guys! Stanislav Shushkevich and Pavel Starovoitov left before my moment of triumph, unfortunately, but I still remember you, thank you, hope to see you sometime in the future. And Nastya and Julia Grebenyuk, who also didn't wait long enough to see it, but were still believing in me, and helping me to finally make it, thank you too!

And everybody else who helped me with my work, the members of the DESY ATLAS group, and my friends from Hamburg, thank you all for your help.

And finally, a special mention for my family, my mother and grandmother, who waited patiently for my work to finish. See? I kept my word! If only a couple of years later.

Thank you all!

👍 Like Like if you opened the thesis only to read this page.